

学位申請論文

Study on universality of laminar-turbulent patterning to annular geometry of Poiseuille flows and on robustness of the patterning to roughness and rotation in plane channel flows

(環形状に対するポアズイユ流の層流乱流パターン形成普遍性と粗さ及び回転に対する平行平板間流でのパターン形成ロバスト性に関する研究)

Mar 2017
(平成29年3月)

Takahiro Ishida
(石田 貴大)

Contents

Nomenclatures	iii
1 Introduction and objective	1
1.1 Transition scenario in wall-bounded shear flows	1
1.2 Annular Poiseuille flow	2
1.3 Plane Couette flow with roughness	4
1.4 Rotating plane Poiseuille flow	5
1.5 Objective	7
2 Numerical procedures	10
2.1 Annular Poiseuille flow	10
2.2 Plane Couette flow with roughness	11
2.3 Rotating plane Poiseuille flow	17
3 Investigations of laminar-turbulent pattern in annular geometry	20
3.1 Transitional structures depending on radius ratio	20
3.1.1 Helical turbulence for $\eta = 0.8$ and $\eta = 0.5$	21
3.1.2 Helical puff for $\eta = 0.3$	23
3.1.3 Turbulent puff for $\eta = 0.1$	24
3.2 Friction factor and flow statistics influenced by the patterns	26
3.2.1 Flow regime	26
3.2.2 Friction factor	28
3.2.3 Mean flow statistics	31
3.3 Transition between straight and helical puff	34
3.3.1 Temporal dynamics of localised turbulent structures	34
3.3.2 Azimuthal length depending on radius ratio	36
3.3.3 Probability density function of azimuthal velocity	41
3.4 Modal analysis for laminar-turbulent patterning	44
3.4.1 Methods (e.g. $\eta = 0.5$)	44
3.4.2 Dominant modes for $\eta = 0.1$	48
3.4.3 Dominant modes for $\eta = 0.2$ and 0.3	50
3.4.4 Possession of dominant modes	53
3.5 Summary	55

4	Investigations of roughness effect on laminar-turbulent pattern	59
4.1	Quasi-linear stability analysis	59
4.2	Plane Couette flow with two smooth walls	61
4.3	Plane Couette flow with two rough walls	62
4.3.1	Rectangular-shaped roughness elements	62
4.3.2	Gaussian-shaped roughness elements	65
4.4	Plane Couette flow with one rough wall	66
4.4.1	Rectangular-shaped roughness elements	67
4.4.2	Gaussian-shaped roughness elements	72
4.5	Summary	72
5	Investigations of rotation effect on laminar-turbulent pattern	76
5.1	Large-scale structure alternation	76
5.1.1	Coriolis effects on the transitional regime	76
5.1.2	Friction factor	80
5.2	Augmentation of spanwise secondary flow of the pattern	83
5.2.1	Stripe pattern in weak rotation	83
5.2.2	Spanwise secondary flow	88
5.3	Summary	91
6	Discussion	93
7	Conclusion	103
	Appendix A	106
	Acknowledgements	107
	Bibliography	108

Nomenclatures

Br	Bradshaw number, $S/(S + 1)$
C_f	skin friction coefficient
C_η	laminar solution of skin friction coefficient for aPf
d	gap between inner and outer radius for aPf, $r_o - r_i$ [m]
d	gap between two parallel plates for pPf and pCf [m]
D	pipe diameter [m]
E_{ii}	one-dimensional energy spectra [m ² /s ²]
F_i	roughness shape function
F_t	turbulent fraction
h	roughness height [m]
\mathcal{H}	high-pass filter
II'	second invariant of the deformation tensor
k	turbulent kinetic energy [m ² /s ²]
k_i	wave-number in i -direction [1/m]
\mathcal{L}	low-pass filter
L_i	calculation domain size in the i -direction [m]
m_i	spectrum mode in i -direction [1/m]
N_i	number of grid points in the i -direction
P	pressure [Pa]
r_i	inner radius [m]
r_o	outer radius [m]
Re	Reynolds number
Re_g	critical Reynolds number for global instability
Re_l	critical Reynolds number for linear instability
Re_m	bulk Reynolds number, $u_m D/\nu$ for cPf
Re_m	bulk Reynolds number, $u_m d/\nu$ for aPf, pPf, and pCf
Re_t	critical Reynolds number for featureless turbulence
Re_w	wall Reynolds number, $u_w d/\nu$
Re_τ	friction Reynolds number, $u_\tau d/2\nu$ for aPf and $u_\tau \delta/\nu$ for pPf and pCf
$Re_{\tau i}$	friction Reynolds number on the inner cylinder, $u_{\tau i} d/2\nu$ for aPf
$Re_{\tau o}$	friction Reynolds number on the outer cylinder, $u_{\tau o} d/2\nu$ for aPf
Ro_m	bulk Rotation number, $2\Omega h/u_m$
Ro_τ	friction Rotation number, $2\Omega \delta/u_\tau$

S	ratio of rotation- and shear flow-induced vorticity, $-2\Omega/(d\bar{u}/dy)$
t	time [s]
u_i	velocity component, $u_x(u), u_y(v), u_z(w)$ in Cartesian coordinate [m/s]
u_i	velocity component, u_x, u_r, u_θ in cylindrical coordinate [m/s]
\tilde{u}_i	velocity component of small-scale-flow, $\tilde{u}_i = \mathcal{H}u'_i$ [m/s]
U_i	velocity component of large-scale-flow, $U_i = \mathcal{L}u'_i$ [m/s]
U_T	mean streamwise turbulent intensity of each azimuthal mode
W_T	mean azimuthal turbulent intensity of each azimuthal mode
u_m	bulk mean velocity [m/s]
u_w	velocity difference between the wall [m/s]
u_τ	friction velocity, $\sqrt{\tau_w/\rho}$ [m/s]
$u_{\tau i}$	friction velocity on the inner cylinder, $\sqrt{\tau_i/\rho}$ [m/s]
$u_{\tau o}$	friction velocity on the outer cylinder, $\sqrt{\tau_o/\rho}$ [m/s]
$u_{\tau s}$	friction velocity at stable side, $\sqrt{\tau_s/\rho}$ [m/s]
$u_{\tau p}$	friction velocity at unstable side, $\sqrt{\tau_p/\rho}$ [m/s]
\hat{u}_i	velocity component of each mode [m/s]
\acute{u}_i	non-dimensional turbulent intensity of each mode
x_1, x	streamwise direction [m]
x_2, y or r	wall-normal or radial direction, $y = r - r_i$ for aPf [m]
x_3, z or θ	spanwise or azimuthal direction, $z = r\theta$ for aPf [m]
Δx_i	mesh size [m]

Greek

α_i	roughness factor, density of roughness elements [1/m]
δ	channel half width [m]
ε	Levi-Civita symbol
η	radius ratio, r_i/r_o
$\eta(h)$	roughness height as the mean height of the profile [m]
λ_i	wave-length in i -direction [m]
ν	kinematic viscosity [m ² /s]
ρ	density [kg/m ³]
τ_w	statistically averaged wall shear stress [Pa]
Ω	angular velocity [rad/s]
τ_i	statistically averaged wall shear stress on the inner cylinder [Pa]
τ_o	statistically averaged wall shear stress on the outer cylinder [Pa]
τ_s	statistically averaged wall shear stress at stable side [Pa]
τ_u	statistically averaged wall shear stress at unstable side [Pa]
τ_t	statistically averaged total shear stress [Pa]

Superscripts

$()^*$	normalized by inner variables, e.g. u_w, d
$()^+$	normalized by outer variables, e.g. u_τ, ν
$()'$	fluctuation component
$\overline{()}$	statistically averaged

Subscripts

$() _{\max}$	maximum value
$() _{\min}$	minimum value
$()_{\text{rms}}$	root mean square

Abbreviation

aPf	annular Poiseuille flow
cPf	cylindrical Poiseuille flow
DNS	direct numerical simulation
pCf	plane Couette flow
PDF	probability density function
pPf	plane Poiseuille flow
SSP	self sustaining process

1

Introduction and objective

1.1 Transition scenario in wall-bounded shear flows

The flow property in nature and engineering applications is mostly classified into two different types of regime depending on Reynolds number (Re) defined by the rate of inertial and viscous forces. One is the laminar flow where Re is low and viscous forces are dominant. The other is turbulent flow where Re is relatively high and the flow is dominated by inertial forces. The laminar flow travels smoothly or in regular paths and the transfer of fluids is energetically efficient because the friction losses are lower. The turbulent fluid motion is an irregular condition of flow in which the various quantities show a random variation with time and space, and enhances the energy, momentum, and heat transfers. These two different flow regimes that are turbulent and laminar flows cannot be classified by the determined critical point as critical Re in most situations and there is overlapping region as transition regime that smoothly or discretely connects laminar and turbulent regimes. Prediction and control of turbulent transition phenomena are one of the most important issues in the thermofluid dynamics because the flow characteristics significantly change through the transition. Moreover, investigating and understanding the transitional flow regime depending on Re , flow geometry, and external forces, would be the guideline of designing the applications for different purposes in accordance to the use.

Transition to turbulence in most wall-bounded shear flows is subcritical as it features a competition between a linearly stable laminar regime and the turbulent regime (Kerswell, 2011; Manneville, 2015). The cylindrical Poiseuille flow (cPf), plane Couette flow (pCf) and plane Poiseuille flow (pPf) fall into this category and have puzzled researchers and engineers for a long time. This is also the case with the counter-rotating Taylor-Couette flow with large radius ratio, and with zero-pressure gradient flat plate boundary-layer flows with or without wall suction. The laminar-turbulent transition state has been studied by a number of researchers since the first pioneering experiment on the cPf was carried out by Reynolds (1883). Both the cPf and the pCf are considered linearly stable for any Re . However, experimental studies have demonstrated that both the cPf and the pCf cannot

maintain these laminar states at high Reynolds numbers, no matter how well the experiment is conducted (Pfenniger, 1961), because unpreventable finite-amplitude disturbances trigger a subcritical bypass transition. As for the pPf, the base flow is linearly unstable only for values of Re far above the first values where turbulence can be sustained in experiments (Schmid and Henningson, 2001). Transition in these flows is hence characterized by sensitivity to finite-amplitude perturbations only, and thus by hysteresis between the critical Reynolds number for global (Re_g) and linear instability (Re_l). The lowest end of the transitional range features intermittent coherent structures referred to as ‘puffs’ in the cPf (Wynanski and Champagnem, 1973; Wynanski et al., 1975) and ‘oblique stripe patterns’ in the pPf (Tsukahara et al., 2005) and the pCf (Prigent and Dauchot, 2002; Duguet et al., 2010). A typical property of such an intermittent structure observed in a transitional flow is the spatial coexistence of two stable states of laminar and turbulence in a flow, giving rise to alternation of the localized turbulence and the background laminar flow with respect to a homogeneous direction. In the case of the cPf, the geometry makes this alternation essentially one-dimensional, and a critical Reynolds number has been predicted (Avila et al., 2011) in the thermodynamic limit of infinitely long domain and observation times. This special point statistically delimitates the regime of transient localized turbulence from that of spatial turbulence proliferation. This suggests that the dynamics of isolated turbulent structures represent the key to the statistical characterization of the laminar-turbulent transition. Compared to the cPf, planar shear flows such as the pCf and the pPf show spatial extension in one additional (spanwise) direction. This gives rise to complex large-scale flows involved in the formation of the oblique stripe patterns (Duguet and Schlatter, 2013) around Re_g . The stripe pattern is inclined with respect to the streamwise direction. Many questions remain open regarding their growth mechanisms, robustness and lifetime (Manneville, 2015). There has been no direct determination of the global Reynolds number threshold for transition to sustained turbulence using the method proposed for the cPf (Avila et al., 2011), despite recent success in adapting this approach to one-dimensional periodic representations of Couette flows (Shi et al., 2013). In addition, the determination of Re_g value generally demands a massive flow channel (in experiments) or computational resources (in simulations), because of the presence and large-scale patterning of localized turbulence.

1.2 Annular Poiseuille flow

The pressure driven flow between two concentric cylinders (annular Poiseuille flow; aPf) is also in the subcritical scenario. This set-up is used in many industrial situations, such as heat exchangers, and cooling of nuclear plants. The aPf is one of the simplest incompressible flow systems featuring a skewed velocity profiles. In addition to its merit of being a closed system in the spanwise (azimuthal) direction, the aPf may be an ideal flow system

to understand canonical wall-bounded shear flows in a comprehensive manner based on the radius ratio, denoted by $\eta = r_i/r_o$ (where r_i and r_o are the inner and outer radii, respectively). The limit $\eta \rightarrow 1$ corresponds to the pPf. The limit $\eta \approx 0$ has sometimes been regarded in the literature as a modified cPf (Mott and Joseph, 1968). Both geometries differ strongly, even in the limit $\eta \rightarrow 0$, because of the presence of the inner rod in the aPf. Laminar profiles in the aPf are known to be linearly unstable for all η ($0 < \eta \leq 1$) above a critical Reynolds number $Re_l(\eta)$ (Cotrell and Pearlstein, 2006; Heaton, 2008). Despite the relatively high values for the linear instability thresholds, there is experimental evidence that an actual transition to turbulence can occur for $Re \ll Re_l$ (Walker et al., 1957), i.e. the transition is of a subcritical type. Together with the common one-dimensional extension and symmetries, this justifies why the cPf can be expected to display the same transition phenomenology as the aPf in the limit $\eta \rightarrow 0$. For $\eta = 1$, the critical Reynolds number coincides exactly with that for the pPf, whereas for $\eta \rightarrow 0$, Re_l diverges as $\eta^{-1} \log \eta$, inducing linear stability as in the cPf (Heaton, 2008).

High- Re turbulent statistics have previously been reported in simulations and experiments for different radius ratios (see e.g. Chung et al., 2002; Chung et al. and Sung, 2003; Rodriguez et al., 2014). Surprisingly little is known yet about the transitional regime. Patel & Head (1969) measured the skin friction coefficient to examine the transition regime and how turbulence can be sustained in the cPf and the pPf, both of which are the limiting cases of the aPf. They found that Re_g occurred at $Re_m|_{cPf} = u_m D/\nu \approx 2000$ for the cPf and at $Re_m|_{pPf} = 2u_m \delta/\nu \approx 1350$ for the pPf (where u_m denotes the bulk mean velocity; D the pipe diameter). Recently, Samanta et al. (2011) considered the dependence of the friction factor on initial conditions in the cPf focusing on localized structures of puff and spot. Their data provided a well-defined connection between the laminar and turbulence laws and predicted well the upper limits of the transitional regime. Since the aPf is widely used in engineering applications, several previous studies examined the friction factor as typified by Rothfus's group (Rothfus et al., 1950; Walker et al., 1957; Croop and Rothfus, 1962). Those studies suggested the critical Reynolds numbers of the onset and end of the transitional regime (Walker et al., 1957), which were defined by a slight progressive departure from the theoretical analysis and the empirical equation of the cPf (applied for aPf using the hydraulic diameter), respectively. The obtained onset Reynolds numbers of transition for $\eta = 0$ and 1 almost agree with those obtained by the recent studies for the global instability of the cPf (Avila et al., 2011) and the pPf (Patel and Head, 1969).

Hanks and Bonner (1971) employed a theoretical analysis to suggest that the first transition occurs near the inner cylinder and the second transition that occurs near the outer cylinder follows the first one. A smaller radius ratio η led to larger differences in the value of the critical Reynolds number between the first and second transitions. Moreover, due to the existence of singularity (inner cylinder), the first critical Reynolds number indicated that the flow was always unstable for any Reynolds number as η approached zero. In contrast, there was no difference between the first and second critical Reynolds numbers

at $\eta = 1$. Their result also suggested that the dual flow regime consisting of laminar and turbulent flows near the outer and inner cylinders, respectively, separated at the radial position of maximum velocity, and this typically occurred between the first and the second critical Reynolds numbers. The second critical Reynolds number (on the outer cylinder side) obtained by experiment (Walker et al., 1957) and theoretically (Hanks and Bonner, 1971) was similar to that in the pPf, although they did not exactly correspond. The second critical Reynolds number for the aPf was indicated to connect between the cPf and the pPf with the variance of η . Hanks and Peterson (1982) also performed an experimental study to verify the theoretical analysis, measured the flow rate using the oscilloscope traces at a low radius ratio ($\eta = 0.0416$), and observed the first and the second transitions. Despite the occurrence of the first transition, no oscillation was observed in the dual-flow regime where oscillations were expected to exist, while disturbed oscillations were detected for the second transition.

1.3 Plane Couette flow with roughness

Many incompressible shear flows can undergo transition to turbulence even in the absence of a linear instability of the laminar regime as discussed in the previous sections. This is also the case for the pCf, the flow between two parallel plates moving at different velocities, where the laminar base flow features homogeneous shear and a zero pressure gradient. A striking consequence of this competition between laminar and turbulent regimes is the possible spatial coexistence of a laminar flow with turbulent patches. Turbulent patches usually possess well-defined streamwise lengths (Manneville, 2016). For instance, most turbulent puffs in the cPf have a streamwise length of about 20 pipe diameters. Their equivalent in the pCf consists of turbulent band oblique to the mean flow, forming patterns whose streamwise wavelength is approximately 20 to 30 gap widths (Prigent, 2001; Duguet et al., 2010). Investigation of such regimes becomes demanding near the onset in Reynolds number Re_g where the fraction of turbulent flow becomes small (Avila et al., 2011; Lemoult et al., 2016; Sano and Tamai, 2016) and the flow shows strong intermittency both in space and time. For high enough Reynolds number turbulence in turn, turbulent motion fills all the space available. Between these two extremes, a relatively wide range of Reynolds number exists in which turbulence (once initiated) can only be found in the form of a regular alternation of laminar and turbulent zones (Moxey and Barkley, 2010). The Reynolds number in the pCf can be defined as $Re_w = u_w d / \nu$ where u_w is the velocity difference between the plates separated by a gap d . The onset in Re_w is known from experiments and large-scale simulations to be near $Re_g = 1300 \pm 20$, while laminar-turbulent patterns have been reported in the range 1320–1600, and featureless turbulence, is found only for $Re_w \geq Re_t = 1600$. The mean turbulent fraction increases monotonously from a finite value at Re_g (at least within a finite domain) to $\approx 100\%$. These approximate threshold values can be

dramatically augmented by the addition of a damping force. Laminar-turbulent patterns in the pCf have for instance been identified for values of Re as high as 8×10^4 (using the above definition) in the presence of cyclonic spanwise rotation or stable stratification (Brethouwer et al., 2012, Deusebio et al., 2014, 2015). Despite recent progress in interpretation (Barkley, 2011), the physical reasons for the laminar-turbulent coexistence, its self-organization and dynamics, remain to be better understood and quantified.

Most of these experimental shear flow studies were performed with carefully designed smooth walls. Moreover, numerical simulations have focused so far on perfectly smooth walls. However, most solid surfaces in nature and in technological applications show some degree of irregularity describable as roughness. Hence, it is natural to wonder how robust the laminar-turbulent coexistence is to the presence of wall roughness. A quantitative study is justified in many regards: from a fundamental point of view, it is desirable to assess whether the phenomenon of shear flow intermittency is only of academic interest. From an engineering perspective, the large energetic fluctuations associated with intermittency can be seen as a nuisance and hence need to be well characterized in order to be avoided. This task involves producing clear cartography of the region of existence of laminar-turbulent patterns in a suitably chosen parameter space including parametrization of the roughness. Moreover, many large-scale atmospheric or oceanic boundary layer flows can be described, as a first approximation, as shear flows over a rough background. Understanding whether the observations of high- Re in Brethouwer et al. (2012) and Deusebio et al (2014, 2015) can be used to understand the often intermittent nature of geophysical flows constitutes a major challenge.

Experimental studies addressing roughness date back to the seminal works of Nikuradze (1931) in the cPf. They measured statistical quantities such as the friction factor vs. Re in a pipe with sand covered walls. Their study indicates that the turbulent flow becomes independent of viscosity for sufficiently large roughness height. However, few pipe flow studies so far have reported on the influence of roughness on the localized turbulent structures occurring in the so-called transitional regime [$Re_g : Re_t$]. The case of planar shear flows, with their large-scale patterns delimited by oblique laminar-turbulent interfaces, remains even less explored to this date.

1.4 Rotating plane Poiseuille flow

The onset of a laminar-turbulent patterning that we called the ‘stripe pattern’ was first demonstrated by Tsukahara et al. (2005) in the pPf. The typical structure of stripe pattern, which is characterized by regular turbulent bands oblique to the streamwise direction, and by spanwise secondary flow, was described by direct numerical simulation (DNS) and experimental studies on the transitional pPf (Tsukahara et al., 2006; Hashimoto et al., 2009) and on the pCf (Prigent, 2001; Duguet et al., 2013) as also described in the previous

subsection. Tsukahara et al. (2010a) reported the streamwise- and spanwise-wavelengths of stripe pattern as $\lambda_x^+ = \lambda_x(u_\tau/\nu) \approx 5000$ and $\lambda_z^+ \approx 2000$, respectively, in the pPf at $\text{Re}_\tau = u_\tau\delta/\nu = 80$ (where u_τ , the friction velocity; and δ , half the channel width). When the Reynolds number decreases from a high Reynolds number to a value in the transitional regime, the appearance of the stripe pattern delays the reverse transition (from fully turbulence to a laminar), and the flow maintains momentum and scalar transfers as great as the corresponding turbulent flow (Tsukahara et al., 2006 and 2010a). Therefore, the onset of the stripe pattern is an important issue to consider in order to understand the fluid dynamics related to the subcritical transition.

Tsukahara et al. (2010b) and Brethouwer et al. (2012) demonstrated the onset of the stripe pattern in rotating plane Couette flows, an open channel flow, and a magnetohydrodynamic flow, all of which were subjected to external stabilizing forces of the Coriolis, buoyancy, or Lorentz forces. Their results imply that, under stable stratification due to an external force, the fully-developed wall turbulence at a high Reynolds number would provide a stripe pattern. However, until recently, there was no study reporting on the stripe pattern in the rotating plane Poiseuille flow subjected to spanwise system rotation. This may be because streamwise-oriented roll cells due to the Coriolis instability would dominate the flow in terms of turbulent structures. Actually, the turbulent pPf with spanwise system rotation involving roll cells has been investigated experimentally (Johnston et al., 1972; Tafti and Vanka, 1991; Matsson and Alfredsson, 1994; Lamballais et al., 1996) and numerically (Kristoffersen and Andersson, 1993; Iida et al., 2010), and no footprint of a stripe pattern could be found in the flow even at low Reynolds numbers.

The pPf with spanwise system rotation is known to consist of a pressure side and a suction side (Johnston et al., 1972; Kristoffersen et al., 1993; Matsson et al., 1994). On the suction side of the channel, where the system rotation has the same direction as the vorticity of the mean shear, the flow becomes stable, thereby promoting the tendency of flow separation from the wall surface. Even for fully-turbulent states, stable stratification would attenuate the turbulent motion in this region. On the pressure side, the flow becomes unstable, and longitudinal roll cells may occur at an initial stage of laminar-turbulent transition and survive even with a turbulent background at a high Reynolds number due to the Coriolis force instability. The structure of roll cells involves an array of large-scale longitudinal vortices aligning in the spanwise direction with regularity.

As discussed above, the pPf with spanwise system rotation is a complicated flow field consisting of a suction side and a pressure side. Bradshaw (1969) and Lezius and Johnston (1976) determined the stability by Bradshaw number (Br), or the Richardson number:

$$\text{Br} = S(S + 1), \quad (1.1)$$

where

$$S = -\frac{2\Omega}{d\bar{u}/dy}. \quad (1.2)$$

In the equation, Ω is denoted as the system rotation vector. The flow should be stabilized or destabilized depending on Br: the effect of rotation is destabilizing when $\text{Br} < 0$, while stabilization of the flow may be expected when $\text{Br} > 0$.

Moreover, the Coriolis force has two major effects: a linear effect and a scrambling effect (Cambon et al., 1997; Morinishi et al., 2001). The scrambling effect is due to the nonlinear interaction among the velocity components of the rotating turbulence. This nonlinear interaction inhibits the energy cascade and delays the decay of turbulence. As for the linear effect, if we consider the channel flow with a system rotation with respect to the spanwise axis, the Coriolis force would act as the energy exchange between $\overline{u'u'}$ and $\overline{v'v'}$ (here, u' , streamwise velocity fluctuation; v' , wall-normal velocity fluctuation) through the Reynolds shear stress ($-\overline{u'v'}$). Each transport equation of the Reynolds stresses has been described in the literature: for instance, see (Johnston et al., 1972). In the case that Ω and $d\bar{u}/dy$ have the same sign (as is the case for the pressure side), turbulent energy will be transferred from $\overline{u'u'}$ to $\overline{v'v'}$. On the other hand, the opposite rotation will give a reverse transfer to $\overline{u'u'}$ and a decrease in $\overline{v'v'}$. The wall-normal component $\overline{v'v'}$ is important for turbulence production since it directly influences $\overline{u'v'}$. Then, the suction side will lead to decreases in $\overline{u'v'}$ and also in the production of turbulent energy. In the pPf with spanwise system rotation, these energy redistributions through the Coriolis term would lead to an equalization and a differentiation of the two components ($\overline{u'u'}$ and $\overline{v'v'}$) on the pressure and suction sides, respectively. However, it is not obvious what the overall result would be on the turbulence or the intermittent structures in transitional flows. Moreover, it is interesting to discuss the effects of the Coriolis force on the spanwise velocity component, because the spanwise secondary flow must play an important role in the pattern (or the oblique band) formation in the static system.

1.5 Objective

The subcritical transition phenomena particularly including the cPf, have been explained through the greatly efforts of researchers in recent years. The formation of the laminar-turbulent pattern depends on the flow geometry and there are two types of the pattern. One is the streamwise localized structure that is turbulent puff observed in the cPf and the other is the stripe pattern that has the oblique laminar-turbulent interface observed in the pPf and pCf. The turbulent puff has temporal dynamics that are self-replication, merging, decaying events, whereas stripe pattern is steady or is not well understood the dynamics. These differences of the pattern may be characterized by spanwise confinement of the geometry. In addition, any pattern has not been organized in the suction boundary layer because of the wall-normal freedom of the flow (Khapko et al., 2016). These various types of flow systems, such as the cPf and the pPf, have been treated individually, and also the discussion of similarity and connection between flow systems has been extremely

limited. Several additional forces effect on the stripe pattern have been considered in recent years. However, most studies of external forces have evaluated the flow stabilization that attenuates turbulent motion. Although destabilizing effects on the stripe pattern has been studied, the effect always induces large-scale vortical motion that is roll cell and the influence on the coherent turbulent motion has not been discussed. To address the above points, we consider three different kinds of flow geometries, namely the aPf, the pCf with roughness, and the pPf with spanwise system rotation. The universality of laminar-turbulent patterning with respect to the flow system and the robustness of the patterning to external forces are discussed to elucidate the sustaining mechanism of the pattern by means of numerical experiment.

The main issue in this study is the universality of laminar-turbulent patterning. We consider the aPf to puzzle out this issue. This study is the first investigation to evaluate a possible connection between the different canonical geometries with/without spanwise confinement. As described in the previous subsection, the limiting system of the aPf could be treated as the cPf ($\eta \rightarrow 0$) and the pPf ($\eta \rightarrow 1$). The transitional regime of the aPf for varying η , which would bridge together the limiting cases of the cPf and the pPf is analyzed to evaluate a possible connection between the different canonical geometries. In the transitional regime, the puff in the cPf and the stripe pattern in the pPf are found and often reported in the literature. However, in the aPf, the occurrence of the coexistence has not been reported. Therefore, the first issue of the subcritical transition in the aPf is whether a transitional structure like a puff or the stripe pattern occurs in the limiting system of the aPf. The second issue is how to connect or change these structures depending on η . Comparing with the recent results about cPf, the study about the turbulent transition in pPf still has a lot of problems. Therefore, studying the subcritical transition regime of the aPf is expected to be useful for puzzling out that of the pPf by connecting with the transition regimes of the cPf. Moreover, how the transitional structure affects the friction factor and the low-dimensional statistical property are described.

The second main issue is the robustness of laminar-turbulent patterning. To address this issue, we analyze the characteristics of the flow between two parallel plates that manifest transitional states in terms of the Reynolds number, the roughness height, and the rotation number. We consider the rotating plane Poiseuille flow that consists of stabilized and destabilized sides in the wall-normal direction. In addition, pCf with roughness that has wall-normal freedom of the flow and induces instability without large-scale vortical motion is examined. The present thesis particularly discusses how the roughness and the rotation affects the laminar-turbulent patterning, in particular the stripe pattern observed in the transitional flow.

This thesis is organized as follows: Chapter 2 describes numerical methods and parameters for DNS of the aPf, the pCf with roughness, and the pPf with spanwise system rotation. Chapters 3 to 5 consist of investigations of each flow system. In Chapter 3, the universality of turbulent transition independent of flow systems is discussed by considering the aPf with a varying radius ratio. In Chapters 4 and 5, the influence of destabilized systems on laminar-turbulent patterning is discussed by scrutinizing the pCf with roughness and the pPf with spanwise system rotation. In Chapter 6, the robustness and universality of laminar-turbulent patterning in wall-bounded shear flows are thoroughly discussed by summarizing the investigations in Chapters 3 to 5. Finally, the study is concluded in Chapter 7.

2

Numerical procedures

2.1 Annular Poiseuille flow

We consider here the axial flow between two co-axial cylinders, driven by a constant and uniform pressure gradient $d\bar{p}/dx = -(2/d)(\tau_o + \eta\tau_i)/(1 + \eta)$ in the axial direction denoted by x . Here $d = r_o - r_i$ is the gap between the inner and outer cylinders, τ_i and τ_o are the mean wall shear rate at the outer and inner wall, respectively. We adopt the conventional cylindrical coordinate system (r, θ, x) and define $y = r - r_i$ as the wall-normal distance measured from the inner wall and $z = 2\pi r\theta$ as azimuthal length are additionally defined.

The periodic boundary condition is imposed in the x and θ directions. The non-slip condition is applied on the walls. The working fluid is incompressible Newtonian fluid. The friction velocities on the inner and outer cylinder are, respectively, defined as

$$u_{\tau_i} = \sqrt{\frac{\tau_i}{\rho}}, \quad \text{and} \quad u_{\tau_o} = \sqrt{\frac{\tau_o}{\rho}}. \quad (2.1)$$

The averaged friction velocity is defined by

$$u_\tau = \sqrt{\frac{\tau_o + \eta\tau_i}{\rho(1 + \eta)}}. \quad (2.2)$$

The fundamental equation for the velocity $\mathbf{u} = (u_x, u_r, u_\theta)$ and the pressure p are following: the equation of continuity

$$\nabla \cdot \mathbf{u}^+ = 0, \quad (2.3)$$

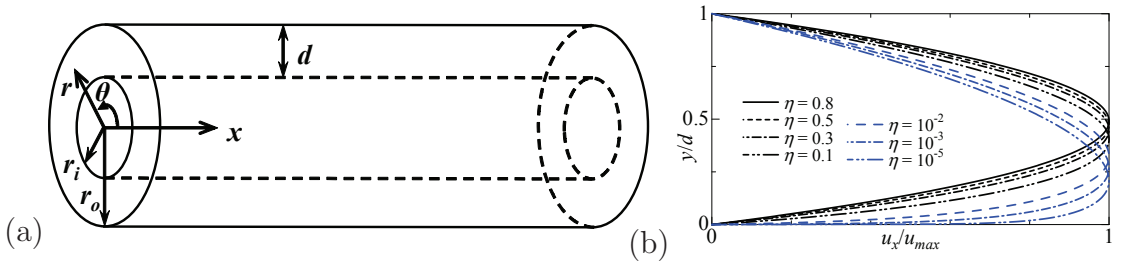


Fig. 2.1 Schematic diagram (a) and laminar velocity profiles (b) of annular Poiseuille flow.

and the Navier-Stokes equation

$$\partial_t \mathbf{u}^+ + (\mathbf{u}^+ \cdot \nabla) \mathbf{u}^+ = -\nabla p^+ + \frac{1}{\text{Re}_\tau} \nabla^2 \mathbf{u}^+. \quad (2.4)$$

Note that, the superscript of + indicates the quantities normalized by the wall unit (i.e., the friction velocity u_τ , and/or the kinematic viscosity ν).

A sketch of the geometry is shown in Fig. 2.1 (a). Velocity profiles of the laminar solutions are reported for values of η ranging from 1 to 10^{-5} in Fig. 2.1(b). The finite difference method was adopted for the spatial discretization. The fourth-order central scheme was employed in both x and θ with uniform grids, while the second-order one was in r with non-uniform grids. The non-uniform spacing in the wall-normal direction was given in a similar way to Moin and Kim (1982). Further information about the numerical method employed here can be found in Abe et al. (2001).

We analyzed several values of $\text{Re}_\tau = u_\tau d / \nu = 46\text{--}150$ and chose five different values of $\eta = 0.1, 0.2, 0.3, 0.4, 0.5$, and 0.8 . We begin by simulating fully turbulent flow at $\text{Re}_\tau = 150$ for each value of η . Re_τ is then decreased in small discrete steps down to the target value. Tables 2.1–2.5 summarize the simulation parameters. We set up long streamwise domains of $L_x = 51.2d\text{--}166.0d$ to capture the intermittent structures with long streamwise extents. The full azimuthal extent depends on η , e.g. $(L_{zi}, L_{zo}) = (2\pi r_i, 2\pi r_o) = (6.28d, 12.56d)$ at $\eta = 0.5$. Statistically steady states were achieved in all cases after transients shorter than our minimum observation time of $tu_\tau^2/\nu \approx 9000$ (approximately $900d/u_m$). Finally, the mean bulk Reynolds number $\text{Re}_m = u_m d / \nu$ and its instantaneous fluctuations are estimated only in the statistically steady regime, where u_m is the bulk velocity. To satisfy the energy conservation near the inner wall especially for low η ($= 0.1$), we make discrete time step smaller. Our DNS code has been validated comparing with the data by Chung et al. (2002) at high $\text{Re}_\tau = 150$ for $\eta = 0.1$ and 0.5 .

2.2 Plane Couette flow with roughness

Two generic approaches dominate numerical studies of rough turbulent flows: direct numerical simulation involving accurate description of specific roughness elements, or simulation of the flow including specific modelling of the expected influence of the roughness. Even in the second case, modelling can enter directly the governing equations or concern the boundary conditions only. The large wavelengths of the patterns imply the use of extended numerical domains, and make brute force simulation of several types of roughness distributions very costly. The modelling approach is still numerically demanding but is more tractable. Yet the difficulty is to select a well-sorted parametric model for the rough walls. The majority of roughness models are dedicated to higher-Re wall turbulence, where most efforts concern an accurate reproduction of the mean velocity statistics

Table 2.1 Numerical conditions for DNS of annular Poiseuille flow for $\eta = 0.8$ and 0.5 : $\text{Re}_\tau = (u_\tau d/2\nu)$ the friction Reynolds number; $\text{Re}_m = (u_m d/\nu)$ the bulk Reynolds number; L_x and L_z are the streamwise and azimuthal lengths ($L_{zi} = 2\pi r_i$ and $L_{zo} = 2\pi r_o$); N_x , N_y , and N_z the corresponding grid numbers ($y = r - r_i$, $z = r\theta$); Δx_i the resolutions.

η	0.8						0.5				
Re_τ	52	56	64	72	80	150	52	56	64	80	150
Re_m	1460	1590	1820	2060	2310	4630	1460	1530	1770	2300	4640
L_x/d	80.0	74.0	64.0	57.0	51.2	51.2	80.0	74.0	64.0	51.2	51.2
$L_{zi}(\eta)/d, L_{zo}(\eta)/d$	25.1, 31.4						6.28, 12.6				
N_x	2048										
N_y	128										
N_z	1024						512				
$\Delta x u_\tau/\nu$	4.0					7.5	4.0				7.5
$\Delta y_{\min} u_\tau/\nu$	0.13	0.14	0.16	0.18	0.20	0.38	0.13	0.14	0.16	0.20	0.38
$\Delta y_{\max} u_\tau/\nu$	1.65	1.77	2.02	2.28	2.53	4.75	1.64	1.77	2.02	2.53	4.75
$\Delta z_i u_\tau/\nu$	2.56	2.75	3.14	3.53	3.93	7.36	1.28	1.37	1.57	1.96	3.68
$\Delta z_o u_\tau/\nu$	3.19	3.44	3.93	4.42	4.91	9.20	2.55	2.75	3.14	3.93	7.36

as a function of the distance to the wall. In particular, a quantitatively correct estimation of the roughness function, i.e., the modification to the logarithmic law of the wall in the form of an additive offset, is the main requirement for a roughness model to perform well (Jimenez, 2004). However, the parameter regime concerned in this investigation does not require such a fine representation of the velocity profile, mainly since Re (and hence the friction Reynolds number Re_τ) is too low to justify the usual description in terms of viscous sublayer, buffer and outer layer, even in the so-called turbulent parts of the flow. The desired model should yet be able to capture phenomenologic expectations about the motion inside the laminar-turbulent interfaces, such as its dimensions, obliqueness, properties, etc ... as well as capture realistic energetic criteria such as the friction factor C_f . We opt here for the parametric roughness model suggested by Busse and Sandham (2012), in which an additive forcing term mimicking the additional pressure drag induced by the roughness elements is included in the Navier-Stokes equations. The Busse-Sandham model is easy to be implemented in a simulation code, and generate no additional computational cost compared to smooth case. They reproduced very well velocity statistics in the case of fully-developed channel flow turbulence with rough walls. This model contains two main parameters: the streamwise density of roughness elements and their statistical height, besides it contains a parametrization of the shape of the roughness elements encoded into a scalar function. Similar to additive forcing terms in the Navier-Stokes equations have been used, e.g., in large-eddy simulations in the context of atmospheric boundary layers, to model the influence of vegetation and forests (Su et al., 1998; Finnigan et al., 2009). This approach is therefore useful to investigate transition in other flows as well, for instance, atmospheric flows are known to become intermittent under the influence of a strong strat-

Table 2.2 Numerical conditions for DNS of annular Poiseuille flow for $\eta = 0.4$.

η	0.4			
Re_τ	52	56	64	80
Re_m	1520	1570	1780	2290
L_x/d	160.0	148.0	128.0	102.4
$L_{zi}(\eta)/d, L_{zo}(\eta)/d$	4.19, 10.5			
N_x	4096			
N_y	128			
N_z	512			
$\Delta x u_\tau/\nu$	4.0			
$\Delta y_{\min} u_\tau/\nu$	0.13	0.14	0.16	0.20
$\Delta y_{\max} u_\tau/\nu$	1.65	1.77	2.02	2.53
$\Delta z_i u_\tau/\nu$	0.85	0.91	1.05	1.31
$\Delta z_o u_\tau/\nu$	2.13	2.30	2.63	3.28

Table 2.3 Numerical conditions for DNS of annular Poiseuille flow for $\eta = 0.3$.

η	0.3							
Re_τ	50	52	54	56	60	64	80	150
Re_m	1700	1590	1590	1600	1670	1800	2280	4650
L_x/d	166.0	160.0	154.0	148.0	128.0	64.0	51.2	51.2
$L_{zi}(\eta)/d, L_{zo}(\eta)/d$	8.98, 2.69							
N_x	4096					2048		
N_y	128							
N_z	512							
$\Delta x u_\tau/\nu$	4.0							7.5
$\Delta y_{\min} u_\tau/\nu$	0.13	0.13	0.14	0.14	0.15	0.16	0.20	0.38
$\Delta y_{\max} u_\tau/\nu$	1.58	1.65	1.71	1.77	1.90	2.02	2.53	4.75
$\Delta z_i u_\tau/\nu$	0.53	0.55	0.57	0.59	0.63	0.67	0.84	1.58
$\Delta z_o u_\tau/\nu$	1.75	1.82	1.89	1.96	2.10	2.24	2.80	5.26

ification (Mahrt, 2014). In the present investigation, we make direct use of this model adapted to the case of pCf, by selecting two generic shapes of roughness elements and varying the other parameters, including the Reynolds number Re_w . For each case the parameter regions of sustenance of the laminar-turbulent patterns are determined numerically. The data obtained using this procedure eventually sheds light on the mechanisms allowing for turbulence localization.

Plane Couette flow (pCf) is the fluid flow sheared between two parallel plates of different velocities U_1 and $U_2 = U_1 + u_w$ in the streamwise direction x , separated by a gap d in the wall-normal direction y as shown in Fig. 2.2. The spanwise direction is denoted z . The three-dimensional flow is governed by the incompressible Navier–Stokes equations with no-slip boundary conditions at both walls. Velocities, space and time are non-dimensionalised by u_w , d and du_w , respectively. The governing equations are discretized using fourth-order finite differences in both the streamwise and spanwise directions with uniform grids

Table 2.4 Numerical conditions for DNS of annular Poiseuille flow for $\eta = 0.2$.

η	0.2					
Re_τ	50	52	56	64	80	150
Re_m	1730	1665	1660	1790	2273	4630
L_x/d	166.0	160.0	148.0	128.0	102.4	102.4
$L_{zi}(\eta)/d, L_{zo}(\eta)/d$	1.25, 0.25					
N_x	4096					
N_y	128					
N_z	256					
$\Delta x u_\tau/\nu$	4.0					7.5
$\Delta y_{\min} u_\tau/\nu$	0.13	0.13	0.14	0.16	0.20	0.38
$\Delta y_{\max} u_\tau/\nu$	1.58	1.64	1.772	2.02	2.53	4.75
$\Delta z_i u_\tau/\nu$	3.07	3.20	3.44	3.93	0.98	1.84
$\Delta z_o u_\tau/\nu$	0.62	0.64	0.69	0.79	4.90	9.20

Table 2.5 Numerical conditions for DNS of annular Poiseuille flow for $\eta = 0.1$.

η	0.1									
Re_τ	46	48	50	52	54	56	60	64	80	150
Re_m	1520	1540	1570	1600	1660	1650	1710	1790	2260	4635
L_x/d	180.0	173.0	166.0	160.0	154.0	148.0	138.0	64.0	51.2	51.2
$L_{zi}(\eta)/d, L_{zo}(\eta)/d$	6.98, 0.70									
N_x	4096							2048		
N_y	128									
N_z	256									
$\Delta x u_\tau/\nu$	4.0									7.5
$\Delta y_{\min} u_\tau/\nu$	0.12	0.12	0.13	0.13	0.14	0.14	0.15	0.16	0.20	0.38
$\Delta y_{\max} u_\tau/\nu$	1.46	1.52	1.58	1.65	1.71	1.77	1.90	2.03	2.53	4.75
$\Delta z_i u_\tau/\nu$	0.25	0.26	0.27	0.28	0.29	0.31	0.33	0.35	0.44	0.82
$\Delta z_o u_\tau/\nu$	2.51	2.62	2.73	2.84	2.95	3.05	3.33	3.49	4.36	8.18

$N_x \times N_z$, while the second-order one in wall-normal direction with non-uniform grids N_y . Time integration is carried out using a combination of second-order Crank-Nicolson and Adams-Bashforth schemes. Periodicity is enforced in both in-plane directions, with the associated wavelengths denoted L_x and L_z , respectively. The pCf is a convenient prototype for the study of subcritical transition since the associated base flow has a simple analytical expression $U_l(y) = U_1 + y\Delta u_w/d$ (with y the wall-normal coordinate ranging from 0 to d), and is furthermore linearly stable for all values of the Reynolds number (Romanov, 1973). Roughness effects are incorporated in the simulation code without any change in the boundary conditions but using additional force term in the incompressible Navier-Stokes equations. This term models the pressure drag induced by all roughness elements

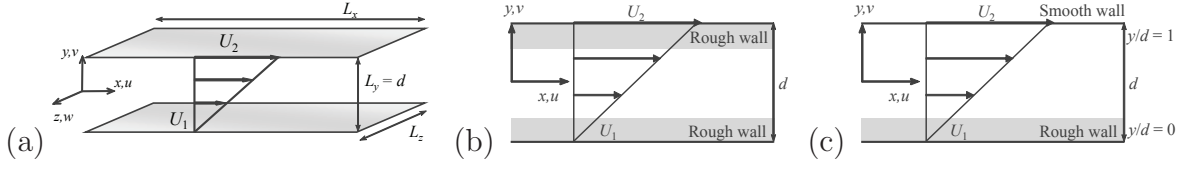


Fig. 2.2 Flow configuration of plane Couette flow with or without roughness.

together. The modified Navier-Stokes equations read

$$\begin{aligned} \frac{\partial u_i^*}{\partial t^*} + u_j^* \frac{\partial u_i^*}{\partial x_j^*} &= -\frac{\partial p^*}{\partial x_i^*} + \frac{1}{\text{Re}_w} \frac{\partial^2 u_i^*}{\partial x_j^* \partial x_j^*} - \alpha_i^* F_i(y) u_i^* |u_i^*|, \\ \frac{\partial u_i^*}{\partial x_i^*} &= 0. \end{aligned} \quad (2.5)$$

where, u_i are the full velocity components (including the base flow) and p the hydrodynamic pressure. Note that * indicates the quantity normalized by the outer scale unit (i.e., d and u_w).

In the drag term $-\alpha_i F_i(y, h_i) u_i |u_i|$, α_i is the roughness factor and F_i the roughness shape function, using the same terminology of Busse and Sandham (2012). An extra force term is added to the Navier-Stokes equations to account for the additional pressure drag induced by the roughness elements, without having to resolve the details of the surface. Because we focus on the pattern formation in the roughness free-area, the explicit roughness element has not been treated and study the effect on the roughness free-area induced by the all roughness elements together. The term was chosen quadratic in the respective velocity component in order to model form drag effects, because the flow is separating from the roughness elements and so the dominant drag is form drag which would scale with the dynamic pressure (i.e., quadratic in velocity). This model enables us to assume the roughness region as assemblage of infinitesimal roughness elements that has very small element size and interval compared to the viscous length. This model can correspond the explicit roughness elements by selecting the parameters (α, F, h) . Busse and Sandham (2012) adapt the best suited roughness parameter to compare the result with the study for transverse square roughness element in pPf by means of DNS (Ashrafian et al., 2004), and confirm that turbulent statistics are good agreement with the explicit study in the roughness free area. Therefore, this indicates that selecting the explicit roughness element is also possible based on the results obtained by roughness model. Note that several numerical investigations of atmospheric boundary layer flows over plant canopies and forests (Su et al., 1998; Finnigan et al., 2009) have included a drag term of the form $\propto -|u_i| u_i$. Busse and Sandham (2012) noted that roughness elements near a wall differ significantly from free-stream cases. To obtain a better outer layer similarity they suggested the drag term $\propto -|u_i| u_i$ used in the present study. This form also ensures that this term always has a damping effect on near-wall velocities. The roughness factor, α_i , is meant to account for the density of the roughness elements with higher values implying more densely spaced elements. We refer to

the original study of Busse and Sandham (2012) for an extensive discussion on the shape factor and study of its influence on the velocity statistics. In principle, both α_i and F_i can be direction-dependent, however, in this more generic study we restrict ourselves to cases whereby both are independent of the direction: that is, $\alpha_x = \alpha_y = \alpha_z = \alpha$. Furthermore, we take $\alpha_i = 1$ which corresponds to mildly dense roughness elements (Busse and Sandham, 2012). Finally, we will only consider two roughness shapes: (i) a rectangular profile

$$F(y) = \begin{cases} 1 & \text{if } y \leq \eta(h) \\ 0 & \text{if } y > \eta(h) \end{cases} \quad (2.6)$$

and (ii) a Gaussian profile

$$F(y) = \exp\left(-\frac{y^2}{\eta(h)^2}\right) \quad (2.7)$$

Besides that we consider varying roughness heights. The roughness height h can be defined in different ways, but here we use the suggestion by Busse and Sandham

$$h = \frac{\int_0^{d/2} F(y) y dz}{\int_0^{d/2} F(y) dz} \quad (2.8)$$

The quantity $\eta(h)$ is chosen as $\eta(h) = 2h$ for the rectangular profile i) and $\eta(h) = h\sqrt{\pi}$ for the Gaussian profile ii). The current model has been implemented in our DNS code, and validated successfully versus Busse & Sandham's data for the case of pressure-driven plane Poiseuille flow with $\text{Re}_\tau = 180$, for equivalent numerical resolution and domain size. Since the roughness model used does not account for e.g., turbulence produced by vortex shedding behind roughness elements, it cannot be expected to give a good representation of the small-scale turbulence inside the roughness sublayer (Busse & Sandham, 2012). However, if the roughness elements are sufficiently small we can expect that this vortex shedding effect is fairly limited and local and does not affect the turbulence outside the roughness sublayer in an important way. Other important effects of roughness, such as the slowing down of the mean flow and the damping of larger-scale turbulent motions in the roughness sublayer, are however well captured by the model. The list of parameters used for both smooth and rough cases can be found in Tables 2.6–2.8.

Table 2.6 Numerical conditions for plane Couette flow with smooth walls.

Wall	smooth wall
Re_w	1200, 1300, 1400, 1500, 1600, 2000
$L_x \times L_y \times L_z$	$68d \times d \times 34d$
$N_x \times N_y \times N_z$	$512 \times 96 \times 256$
$\Delta x \times \Delta z$	$0.13d, 0.13d$
$\Delta y_{\min}, \Delta y_{\max}$	$0.11 \times 10^{-2}d, 2.44 \times 10^{-2}d$

Table 2.7 Numerical conditions for plane Couette flow with two rough walls.

Wall	two rough walls	
Roughness shape	rectangular profile	Gaussian profile
Re_w	600, 700, 800, 900, 1000, 1100, 1200, 1300, 1400, 1500, 1600	1300
$\alpha_i \delta$	0.5	
h/d	0.025, 0.05, 0.075, 0.1, 0.125	0.025, 0.05, 0.075, 0.1
$L_x \times L_y \times L_z$	$68d \times d \times 34d$	
$N_x \times N_y \times N_z$	$512 \times 96 \times 256$	
$\Delta x \times \Delta z$	$0.13d, 0.13d$	
$\Delta y_{\min}, \Delta y_{\max}$	$0.11 \times 10^{-2}d, 2.44 \times 10^{-2}d$	

Table 2.8 Numerical conditions for plane Couette flow with one rough wall.

Wall	one rough wall	
Roughness shape	rectangular profile	Gaussian profile
Re_w	700, 800, 900, 1000, 1100, 1200, 1300, 1400, 1500, 1600	1300
$\alpha_i \delta$	0.5	
h/d	0.05, 0.075, 0.1, 0.15, 0.2, 0.25	0.05, 0.075, 0.1, 0.125, 0.15, 0.175
$L_x \times L_y \times L_z$	$68d \times d \times 34d$	
$N_x \times N_y \times N_z$	$512 \times 96 \times 256$	
$\Delta x \times \Delta z$	$0.13d, 0.13d$	
$\Delta y_{\min}, \Delta y_{\max}$	$0.11 \times 10^{-2}, 2.44 \times 10^{-2}$	

2.3 Rotating plane Poiseuille flow

The plane Poiseuille flow we consider here is driven by a uniform pressure gradient in the x direction and is subjected to a system rotation about the z axis with angular velocity Ω (≥ 0): see Fig 2.3. In this case, we confirmed the coexistence of the stabilized and destabilized sides in a channel. They are classified as halves of the channel (i.e., the pressure and suction sides are the bottom and top sides, respectively).

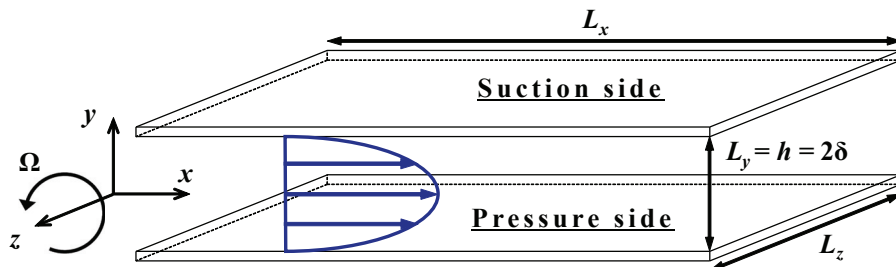


Fig. 2.3 Configuration of plane Poiseuille flow with spanwise system rotation.

In the numerical simulation, the fully-developed state between infinite parallel planes was assumed by the periodic boundary conditions imposed in the horizontal (x and z)

directions. Hence, the ensemble-averaged flow of interest is composed of a unidirectional shear flow having velocity $\bar{u} = \bar{u}(y)$ in the x direction of a Cartesian reference frame rotating with Ω .

The fundamental equations to be computed are the following:
the equation of continuity

$$\frac{\partial u_i^+}{\partial x_i^*} = 0 \quad (2.9)$$

and the Navier-Stokes equation

$$\frac{\partial u_i^+}{\partial t^*} + u_j^+ \frac{\partial u_i^+}{\partial x_j^*} = -\frac{\partial p^+}{\partial x_i^*} + \frac{1}{\text{Re}_\tau} \frac{\partial^2 u_i^+}{\partial x_j^* \partial x_j^*} - \text{Ro}_\tau \epsilon_{i3k} u_k^+. \quad (2.10)$$

Note that the superscripts of $+$ and $*$ indicate the quantities normalized by the wall unit and the outer-scale unit (i.e., half the channel width, δ), respectively, and ϵ_{ijk} represents the Levi-Civita symbol (or Eddington's epsilon). The non-slip condition was applied on the wall surface. The reference velocity of the wall unit, or the friction velocity, is defined as $u_\tau = \sqrt{(\text{d}\bar{p}/\text{d}x^*)/\rho}$. In the channel flow subject to spanwise system rotation, such defined friction velocity is not identical to the local friction velocity at each wall in terms of the alternate definition of $\sqrt{\nu|\text{d}\bar{u}/\text{d}y|_{y^*=\pm 1}}$, where ν is the kinematic viscosity. The local friction velocities are also different between the pressure-side and suction-side walls. Accordingly, we use $u_{\tau\text{p}}$, which denotes the local friction velocity based on the wall shear stress at $y^* = -1$:

$$u_{\tau\text{p}}^2 \equiv u_\tau^2 \frac{\text{d}\bar{u}^+}{\text{d}y^+} \Big|_{y^*=-1}. \quad (2.11)$$

Note again that $u^+ = u/u_\tau$ and $y^+ = yu_\tau/\nu$. Correspondingly, $u_{\tau\text{s}}$ is also given by the wall shear stress at $y^* = 1$.

$$u_{\tau\text{s}}^2 \equiv -u_\tau^2 \frac{\text{d}\bar{u}^+}{\text{d}y^+} \Big|_{y^*=1}. \quad (2.12)$$

In the fully-developed state, u_τ^2 is equal to $(u_{\tau\text{p}}^2 + u_{\tau\text{s}}^2)/2$.

The finite difference method was adopted for the spatial discretization. The fourth-order central scheme was employed in both the streamwise and spanwise directions with uniform grids, while the second-order one was employed for the wall-normal direction with non-uniform grids. For the time integration, the second-order Crank-Nicolson and Adams-Bashforth schemes were used for the wall-normal viscous term and the other terms, respectively.

We performed DNS at three Reynolds numbers of $\text{Re}_\tau = u_\tau \delta / \nu = 54, 64,$ and 80 , which are in the transitional regime between laminar and fully turbulent regimes and are known to exhibit spatially-intermittent turbulent flows in the static system (Tsukahara et al., 2005; Tsukahara et al., 2010a). As for a control parameter of the system rotation, several

Table 2.9 Numerical conditions for rotating plane Poiseuille flow.

Re_τ	54	64
Ro_τ	0.0, 0.01, 0.02, 0.05, 0.1, 0.2, 0.5	
$L_x \times L_y \times L_z$	$102.4\delta \times 2\delta \times 51.2\delta$	
$N_x \times N_y \times N_z$	$2048 \times 192 \times 1024$	
L_x^+, L_z^+	5530, 2765	6554, 3277
$\Delta x^+, \Delta z^+$	2.70, 2.70	3.20, 3.20
$\Delta y_{\min}^+ - \Delta y_{\max}^+$	0.027–0.66	0.032–0.78

Re_τ	80	
Ro_τ	0.0, 0.01, 0.02, 0.05, 0.1, 0.2, 0.5, 1.0, 1.5	
$L_x \times L_y \times L_z$	$102.4\delta \times 2\delta \times 51.2\delta$	
$N_x \times N_y \times N_z$	$2048 \times 192 \times 1024$	
L_x^+, L_z^+	8192, 4096	
$\Delta x^+, \Delta z^+$	4.00, 4.00	
$\Delta y_{\min}^+ - \Delta y_{\max}^+$	0.040–0.98	

rotation numbers of $Ro_\tau = 2\Omega\delta/u_\tau = 0.01$ – 1.5 were tested to investigate the transitional process from a static to a rotating system in terms of structures including stripe pattern and roll cells. In the present study, we have not investigated the flow subjected to a strong system rotation for $Ro_\tau > 1.5$ because the high Ro_τ may give rise to flows dominated by roll cells or a quasi-laminar flow with weak/no contribution of turbulence (Kristoffersen et al., 1993; Iida et al., 2010; Brethouwer et al., 2011).

Table 2.9 summarizes the simulation parameters. We employed a large computational domain to capture several bands of localized turbulence in the flow state of stripe pattern. According to earlier DNS of the static channel flow (Tsukahara et al., 2010a), we expected to capture one or two turbulent band(s) of stripe pattern under the numerical condition described above. As for roll cells, the computational domain was larger than the expected structure dimensions, allowing us to neglect undesirable influences of the periodic boundary. We compare the results at relatively high $Re_\tau = 80$ with that obtained by Iida et al. (2010) using Spectral code, and our DNS results have been validated.

3

Investigations of laminar-turbulent pattern in annular geometry

3.1 Transitional structures depending on radius ratio

In order to demonstrate laminar-turbulent coexistence in the aPf, we begin by displaying in Fig. 3.1 the turbulent fraction F_t , parametrized by η . Its time-averaged value $\langle F_t \rangle$ is plotted as a function of the mean bulk Reynolds number Re_m for easier comparison with other shear flows. F_t measures the instantaneous amount of turbulence in the flow. If $F_t = 0$ the flow is laminar everywhere, whereas when $F_t \sim 1$ the flow is considered fully turbulent. In practice F_t is computed from velocity data on the x - θ cylinder at mid-gap. Laminar regions are identified by monitoring whether $|u_r/u_\tau| < 0.25$ at each (θ, x) position independently of Re , with no significant qualitative dependence on the threshold value. Standard deviations of F_t is displayed as error bars in Fig. 3.1. In order to test the dependence on the wall-normal direction y , the statistics of F_t were also computed closer to the inner and outer cylinders. Again, despite slight shifts of the mean values of F_t the picture remains qualitatively unchanged, therefore we omit these results here.

Whereas F_t is close to unity for $Re_m \geq 2250$, in the range $1750 \leq Re_m \leq 2000$ it fluctuates around a mean value smaller than 0.8, indicating sustained laminar-turbulent coexistence. Moreover, the non-vanishing fluctuations suggest spatiotemporal intermittency. Whereas the results differ quantitatively little among values of $\eta \geq 0.3$, the time-averages of F_t –as well as its fluctuations– stand out in the case of low $\eta = 0.1$: F_t takes high values ≥ 0.8 even for Re_m as low as 1800, and continuously drops to zero over a very narrow interval of values of $Re_m \approx 1500 - 1700$. Note that the amount of statistics and the computational power needed for an accurate determination of the critical values of $Re_m(\eta)$ is several orders of magnitude beyond the present computational capability. This is mainly due to the very large domains needed to accommodate a large number of interacting localized patches near onset, as well as to the huge timescales involved Avila et al. (2011). $\langle F_t \rangle$ should therefore not be interpreted as an order parameter, as in non-equilibrium phase transitions, because

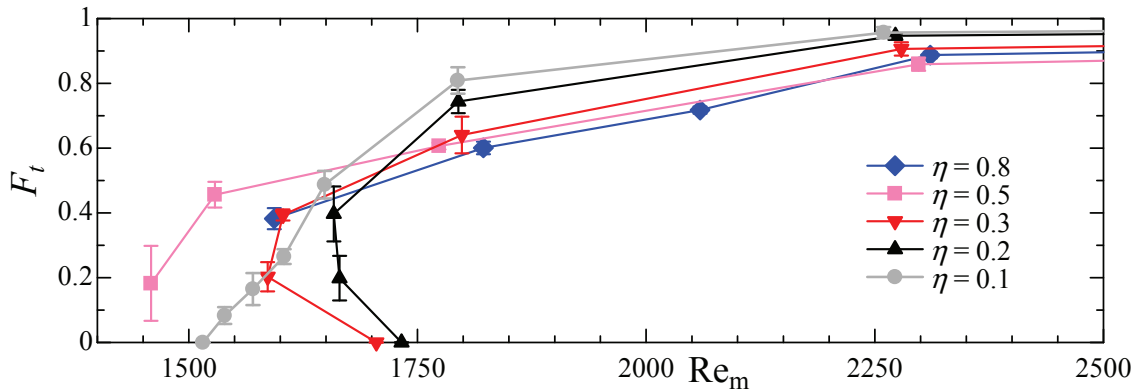


Fig. 3.1 Turbulent fraction as a function of the mean bulk Reynolds number Re_m for each value of η . Laminar and turbulent regions are sorted according to $|u_r/u_\tau|$ (laminar $< 0.25 <$ turbulent). Error bars correspond to the standard mean deviations of F_t over the observation times considered here.

the thermodynamic limit becomes harder to reach as Re_g is approached from above. In the following, we classify large-scale coherent structures typical of each value of η , estimate visually whether they resemble the puffs and stripes of the cPf and the pPf, and show how they are connected to each other through variations of η .

3.1.1 Helical turbulence for $\eta = 0.8$ and $\eta = 0.5$

The typical equilibrium structures observed in the aPf for high $\eta = 0.8$ are first described here. A three-dimensional visualization of instantaneous streamwise velocity fluctuations at $Re_\tau = 72$ ($Re_m = 2060$) is shown in Fig. 3.2(a). Figure 3.2(b) displays two-dimensional contours of wall-normal velocity in an $x-\theta$ cylinder at mid-gap. We use $z = r\theta$ as a modified coordinate unfolding the pipe geometry in Fig. 3.2 and the figures hereafter. We also display in Fig. 3.2(b) the large-scale flow at the same locations using vectors, computed using a low-pass spectral filter selecting all azimuthal and axial wave numbers smaller than 4. For $\eta = 0.8$, we found a spatially periodic arrangement of oblique turbulent regions. Visualizations of turbulent fluctuations closer to the inner or outer wall show negligible differences since $L_{zi} \approx L_{zo}$ and curvature effects are small. These bands have a well-defined pitch angle of about $24 \pm 4^\circ$ with the streamwise direction, depending on the y location at which it is measured. As in Duguet and Schlatter (2013), the large-scale flow evaluated at mid-gap points in a direction almost parallel to the turbulent bands. The pattern is very reminiscent of the laminar-turbulent stripe patterns arising in the pPf or from the barber-pole turbulent structures found in TCf for higher η (Coles, 1965; Prigent and Dauchot, 2002). This pattern wraps endlessly around the inner cylinder because of the azimuthal periodicity. We call this structure a ‘helical turbulence’ in order to distinguish it from the stripe pattern in the pPf and pCf. The large-scale flow possesses both streamwise

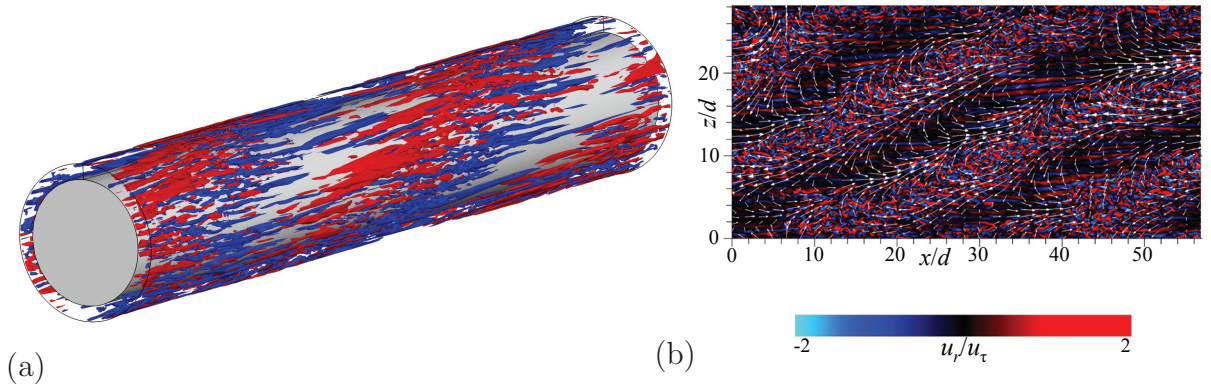


Fig. 3.2 Instantaneous visualization for $Re_\tau = 72$ and $\eta = 0.8$. (a) Three-dimensional visualization of streamwise velocity fluctuations (red, $u'_x > 3$; blue, $u'_x < -3$); (b) two-dimensional contours of instantaneous u'_r at mid-gap. In all figures, the main flow is from left to right. The corresponding large-scale flow around helical turbulence are visualized using arrows in (b).

and spanwise velocity components. From Fig. 3.2(b) it is clear that this large-scale flow also satisfies an approximate helical symmetry, and the corresponding (signed) helix angle can be used to characterize the chirality of the turbulent pattern. For $Re_\tau = 72$, the streamwise and azimuthal extents of the turbulent intervals can be evaluated to $25d$ and $12d$, respectively. Such dimensions are directly comparable to those in the pPf (Tsukahara et al., 2010). For $Re_\tau < 72$, the extent of the turbulent region stays unchanged whereas the laminar intervals between the turbulent regions expand in the streamwise direction, again echoing most observations in the pPf.

Figure 3.3(a) now shows a three-dimensional visualisation of azimuthal velocity for $\eta = 0.5$ at $Re_\tau = 56$ ($Re_m = 1530$). This confirms that helical turbulence is robust and can be observed even for stronger wall curvatures. The velocity contours at mid-gap, shown in Fig. 3.3(b), reveal a turbulent helix with a pitch of $15 \pm 3^\circ$ steeper compared to the cases $\eta = 0.8$ and 1. For comparison, earlier studies of the pPf have reported a regular turbulent stripe pattern with a spanwise spacing of at least $12d$ and an inclination angle of $21 - 25^\circ$ (Tsukahara et al., 2005; Tsukahara et al., 2010a; Tuckerman et al., 2014). For further comparison, we note that for $\eta = 0.5$ outer and inner circumferences are $(L_{zi}, L_{zo}) = (6.28d, 12.56d)$. Comparable spanwise dimensions would not be large enough to sustain stripes in the planar case. This suggests that the annular geometry and the wall curvature make helical turbulence patterns more robust, at the price of steeper angles never reported in the planar case.

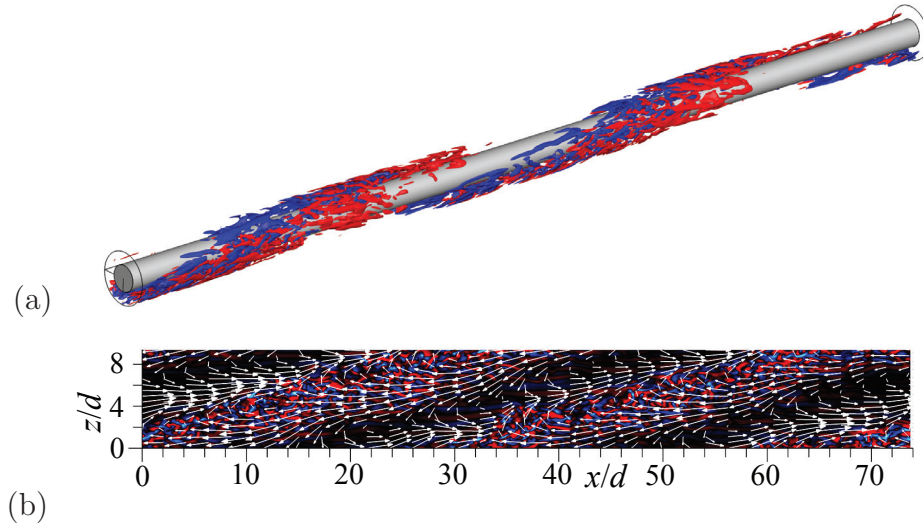


Fig. 3.3 Instantaneous visualization for $Re_\tau = 56$ and $\eta = 0.5$. (a) Three-dimensional visualisation of azimuthal velocity fluctuations (red, $u'_\theta > 1$; blue, $u'_\theta < -1$); (b) two-dimensional contours of instantaneous u'_r at mid-gap. Same color coding as in Fig. 3.2 (b).

3.1.2 Helical puff for $\eta = 0.3$

We consider now the aPf with a lower radius ratio $\eta = 0.3$, for which $(L_{zi}, L_{zo}) = (2.7d, 9.0d)$. Flow visualizations for $Re_\tau = 80$ show almost featureless turbulence on the inner wall while the flow appears intermittent on the outer wall. Further decrease of Re_τ to 64 leads again to a clear stripe pattern, now characterized by stronger intermittency judging from the temporal fluctuations of F_t . The interesting regime occurs for $Re_\tau = 56$ ($Re_m = 1600$). Flow visualisation in Fig. 3.4 for $Re_\tau = 56$ ($Re_m = 1600$) shows, for all velocity components, that the helical structure is still recognizable with a pitch of $9 \pm 3^\circ$, but it is now localized in the streamwise direction. Despite its evident chirality, the helical structure is thus closer to a puff-like shape. The streamwise length of this new localized structure, approximately half the periodic domain length $L_x = 74d$, fluctuates little with time and the localization is robust (Figs. 3.4(a, d)). Analysis of the large-scale flow suggests that the helical puff rotates azimuthally around the inner rod as it propagates downstream (see Figs. 3.4(b, e)). Velocity profiles that are not averaged in the azimuthal direction show two active zones of turbulent fluctuations. Azimuthally-averaged radial velocity profiles show in turn a singly connected zone of turbulent fluctuations, again occupying in average half the domain length (Figs. 3.4(c, f)). From such profiles one could deduce that the upstream front is not sharper than the downstream one, hence violating the upstream/downstream asymmetry typical of turbulent puffs found in the cPf and in the aPf for $\eta = 0.1$. We however note from Figs. 3.4(b, e) that the large-scale flow is at all times strongest near the upstream front, but only in a narrow range of azimuthal angles. Hence the helical puff displays a more subtle upstream/downstream asymmetry

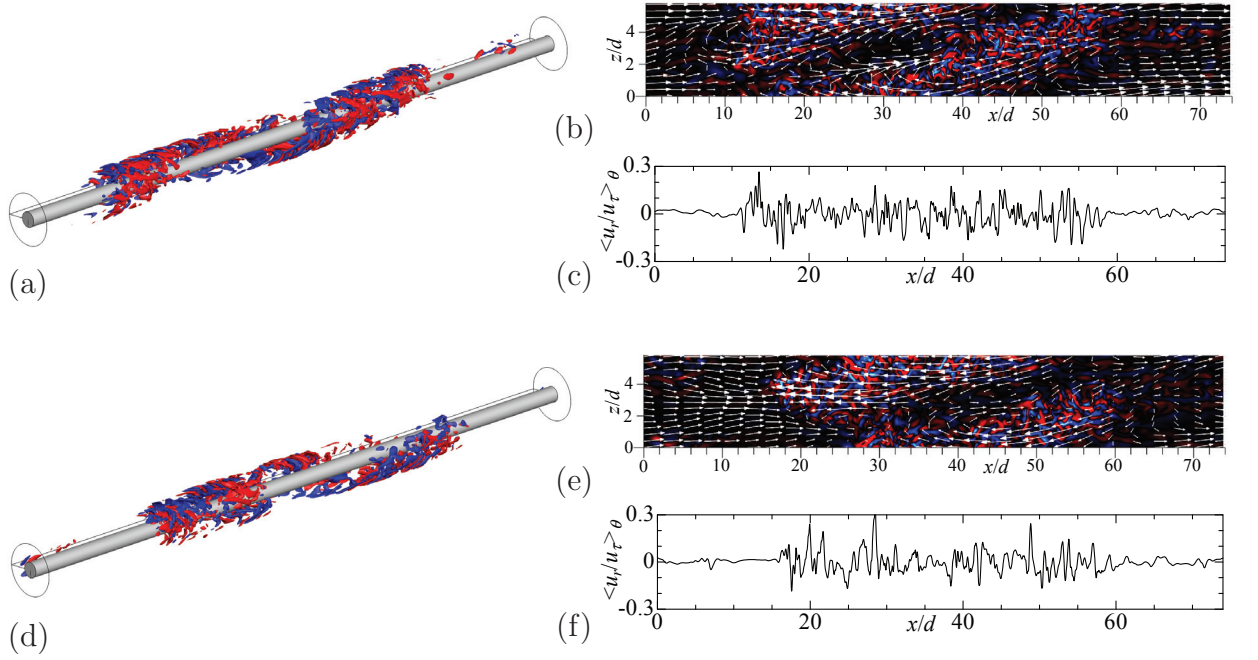


Fig. 3.4 Instantaneous visualizations for $Re_\tau = 56$ and $\eta = 0.3$: (a) and (d), three-dimensional visualization of instantaneous u'_θ ; (b) and (e), contours of instantaneous u'_r and vector at mid-gap same as Fig. 3.2(d); and, (c) and (f), azimuthally-averaged wall-normal velocity along the x axis. The time lapse between (d)–(f) and (a)–(c) is $88.7d/u_m$.

partially hidden by its chiral shape. At the downstream front, the large-scale velocity field on the mid-gap cylinder shows that fluid both enters the puff and exits it depending on the azimuthal coordinate, implying a non-trivial mass balance at the interface. For $Re_\tau < 56$ this helical puff was observed to relaminarize after less than 10^3 time units (in units of d/u_m). Such coherent structures have never been observed before in annular geometries. In particular, the present computation suggests that helical puffs are marginally low- Re structures and represent the simplest form of turbulence for this geometry. Oblique stripes of finite extent have been reported in the pPf, also at marginally low values of Re (Xiong et al., 2015) but it is not clear whether they are robust isolated structures or transients. They do not possess chirality, hence the different parts of the turbulent region do not interact with each other as is the case for the helical case. We note that localized helical structures have not been observed in the present computations for higher η . The exact range of existence and the lifetimes of these helical puffs, both as function Re and in η , deserve further investigation and we will discuss them following sections.

3.1.3 Turbulent puff for $\eta = 0.1$

We consider eventually the case of smaller η and analyze a few simulations of the aPf for $\eta = 0.1$ as Re_τ is gradually decreased. Despite the presence of a rigid rod at the

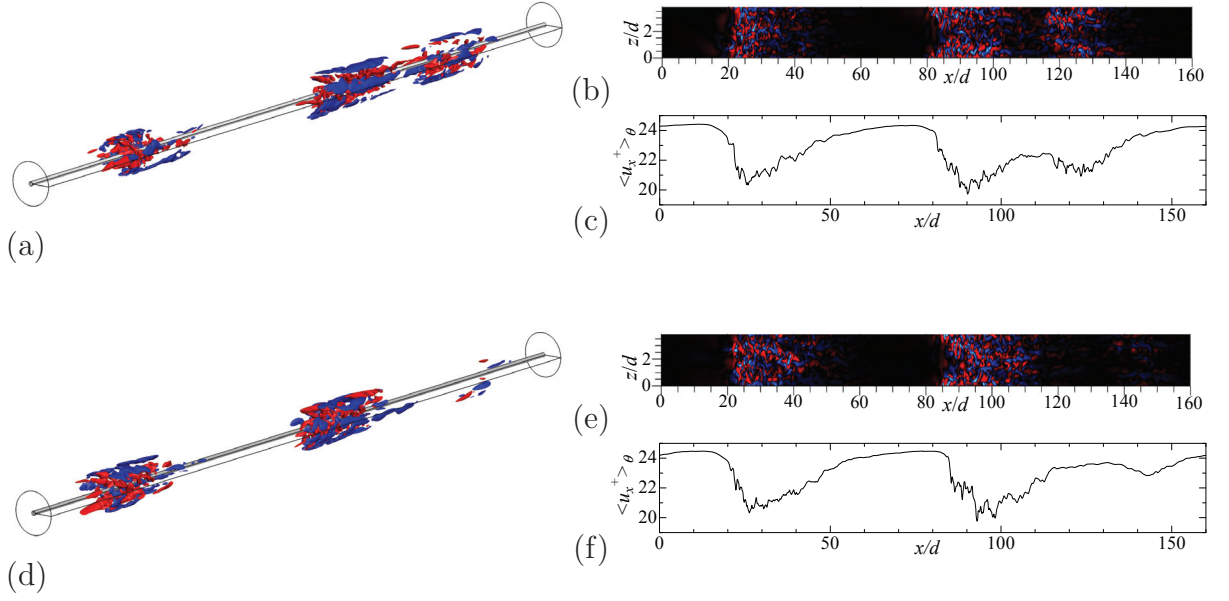


Fig. 3.5 Instantaneous visualizations for $Re_\tau = 52$ and $\eta = 0.1$: (a) and (d), three-dimensional visualization of instantaneous u'_x ; (b) and (e), contours of instantaneous u'_x at mid-gap with the same color range as Fig. 3.2(b); and, (c) and (f), azimuthally-averaged streamwise velocity along the x axis. The time lapse between (a)–(c) and (d)–(f) is $197d/u_m$.

axis, the present phenomenology is very close to that reported in investigations of the cPf (Moxey and Barkley 2010), confirming early speculation. For $Re_\tau \geq 80$, the whole flow is turbulent. However, the time-averaged value of F_t for $Re_\tau = 64$ ($Re_m = 1800$) is 0.8, indicating that short localized laminar pockets occur intermittently (Avila et al., 2013). Reducing Re_τ further to 56 ($Re_m = 1650$), we recognize the classical intermittent sequences of turbulent puffs with sharp upstream fronts. The temporal dynamics of this train of turbulent puffs is complex despite the mild fluctuations of the observable F_t . This steady flow regime shows recurring sequences of instabilities (self-replications) and recombinations (merging) of individual localized puffs. In agreement with experimental observations of pipe flow by Samanta et al. (2011), the term ‘pattern’ is here no longer justified as no clear wavelength emerges, as opposed to the higher- η cases. Further decrease to $Re_\tau = 52$ displays relaminarization or replication events (over longer timescales) but no merging events, see Figure 3.5(a–f).

This dynamics featuring only individual puffs is identical to the regime just above the critical point in the cPf (Avila et al., 2011; Shimizu et al., 2014). Further decrease of Re_τ to 48 shows only puffs with finite lifetimes, but no replication events, suggesting (in the thermodynamic limit) that Re_τ lies here below the critical point. The original streamwise extent of each puff before its possible relaminarization is around $20d$. Because of the finite domain used in simulations, the disappearance of a single puff causes a typical fluctuation

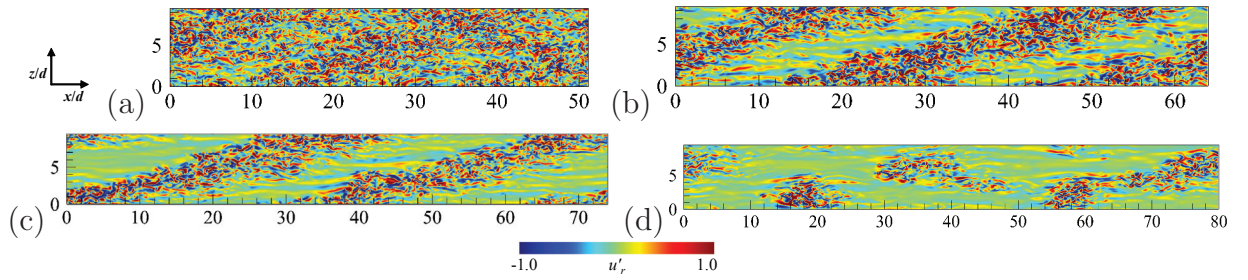


Fig. 3.6 Two-dimensional xz -plane contours of wall-normal velocity fluctuations u'_r at $Re_\tau =$ (a) 80, (b) 64, (c) 56, and (d) 52 for $\eta = 0.5$. The mean flow direction is from left to right.

downwards of F_t . Besides, the lifetimes of individual turbulent puffs in this regime is known to increase very rapidly (typically as double exponential) with Re (Avila et al., 2011). It is hence expected that simulations over observation times several orders of magnitude longer would, for the lowest values of Re_τ , lead to fully laminar flow with $F_t = 0$. The values of $\langle F_t \rangle \approx 0.1 - 0.2$ indicated in Fig. 3.1 for the lowest values of Re_τ can hence be expected to converge to zero with increasing simulation time, making the Re -dependence of $\langle F_t \rangle$ sharper at onset.

3.2 Friction factor and flow statistics influenced by the patterns

3.2.1 Flow regime

The alternations of dominant transitional structures depending on η and Re_τ are discussed in this subsection. Firstly, we would show rather simpler transition processes for high and low η , where observed structures are reminiscent of well-known transition scenarios in the pPf and the cPf. Then, we describe the transition process for intermediate $\eta = 0.3$, which seems to combine features of the transitional structures for lower and higher η , as an anomalous case of the aPf.

As a typical flow regime describing transitional structures, Figs. 3.6–3.8 show the two-dimensional contours of wall-normal velocity fluctuations in the x - z plane for different values of η ($= 0.5, 0.3$, and 0.1).

Firstly, let us focus on the case of a rather high η of 0.5. As visualized in Fig. 3.6(a), featureless turbulence was observed at $Re_\tau \geq 80$ despite the occasional appearance of small laminar patches with wispy obliqueness at $Re_\tau = 80$. Helical turbulence represented by robust oblique laminar-turbulent patterns emerged at $Re_\tau = 64$ and 56. This helical turbulence corresponded to a stripe pattern observed in the plane channel flows (pCf and pPf). The laminar region expanded with a decrease in Re_τ , and the helical turbulence

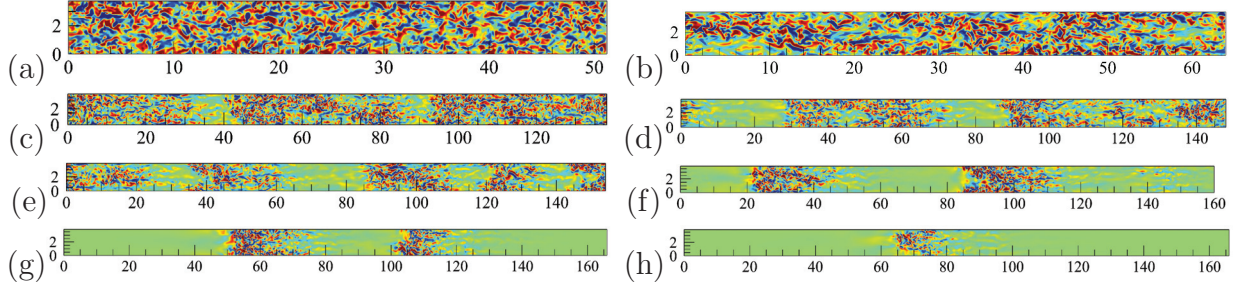


Fig. 3.7 Two-dimensional xz -plane contours of wall-normal velocity fluctuations u'_r at $\text{Re}_\tau =$ (a) 80, (b) 64, (c) 60 (d) 56, (e) 54, (f) 52, (g) 50, and (h) 48 for $\eta = 0.1$. The color range is the same as that in Fig 3.6.

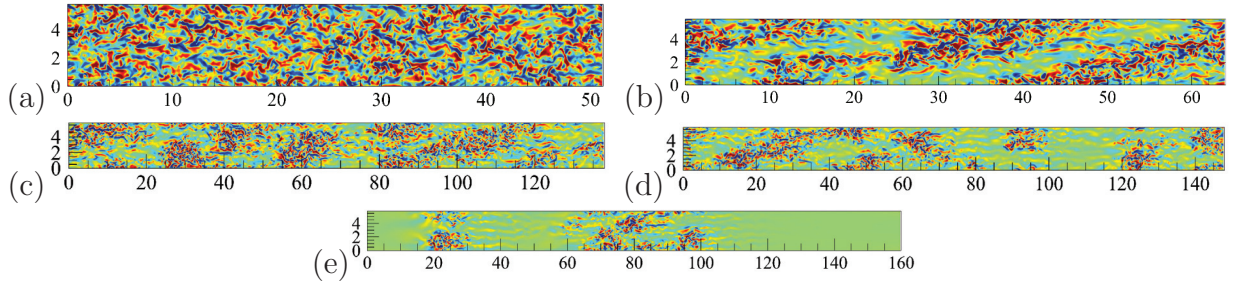


Fig. 3.8 Two-dimensional xz -plane contours of wall-normal velocity fluctuations u'_r at $\text{Re}_\tau =$ (a) 80, (b) 64, (c) 56, (d) 54, and (e) 52 for $\eta = 0.3$. The color range is the same as that in Fig 3.6.

was marginally modulated and collapsed at $\text{Re}_\tau = 52$, as shown in Fig. 3.6(d). Therefore, several helical puffs (with finite streamwise lengths) and turbulent spots were observed for a very low and narrow Reynolds-number range near Re_g . Whereas the previous section suggested that the helical puff occurred only for $\eta = 0.3$, we newly observed the helical puff even for high $\eta = 0.5$. Xiong et al. (2015) also reported similar observations in the pPf at very low Reynolds numbers, demonstrating the occurrence of a localized oblique pattern around Re_g even for the pPf ($\eta \rightarrow 1$). The transition process for $\eta = 0.8$ was similar to that for $\eta = 0.5$. Therefore, clear helical turbulence can be observed for $\eta \geq 0.5$.

A small radius ratio must be expected to reveal transitional states similar to those in the cPf. Figure 3.7 shows the flow fields at $\eta = 0.1$. The featureless turbulence without any laminar patch was confirmed at $\text{Re}_\tau = 150$ and 80. Even at $\text{Re}_\tau = 64$, almost the whole field is dominated by the turbulent region and sometimes small laminar patches occur, as given in Fig. 3.7(b), although helical turbulence emerges for high η . A streamwise localized laminar-turbulent pattern corresponding to the puff in the cPf was found below $\text{Re}_\tau = 60$. Even for small η of 0.1, oblique interfaces between turbulent and laminar region were rarely observed at slightly high values of $\text{Re}_\tau = 60$ and 56. As Re_τ decreased from 60 to 48, the number of puffs or streamwise length of the puff were decreased. The puff in the aPf exhibited splitting, decaying, and combining processes, which were similar to those of

the puff in the cPf (Moxey et al., 2010; Shimizu et al., 2014). At low Re_τ , the combining process could not be detected and the probability of splitting decayed analogous to the previous study (Shimizu et al., 2014). Although the puffs split, one of the separated puffs immediately decayed in the aPf at $Re_\tau = 52$ and 50 . At $Re_\tau = 48$, any puff splitting was not observed, the streamwise size of the puff changed slightly and increased/decreased with time. The flow relaminarized at $Re_\tau = 46$.

As well as the other cases shown above, the intermediate η of 0.3 resulted in the flow state of featureless turbulence at $Re_\tau \geq 80$: see Fig. 3.8(a). At $Re_\tau = 64$, the helical turbulence similar to that observed for $\eta \geq 0.5$ occurred, as shown in Fig. 3.8(b). There was a breaking off point of helical turbulence, and streamwise localized helical turbulence (called helical puff) was observed at $Re_\tau = 60$. Figure 3.8(c) shows the flow field at $Re_\tau = 56$, where mixed helical and straight puffs can be observed. The obliqueness of the helical puff decayed, the straight puff infrequently occurred at lower Re_τ , and the probability of occurrence of a straight puff was increased compared to that of the helical puff, with decreasing Re_τ . At $Re_\tau = 50$, the transitional structure immediately decays and the flow becomes laminar. This complex transition process was also found for $\eta = 0.2$. The occurrence ratio of straight puff increases more compared to $\eta = 0.3$. Additionally, helical turbulence could not be recognized for $\eta = 0.2$ even at high values of Re_τ . Following subsections will discuss the separation of these complex transition processes based on values of both η and Re_τ .

3.2.2 Friction factor

The friction factor, denoted by C_f , is defined by following equation as shown in Fig. 3.9.

$$C_f = \frac{2\tau_w}{u_m^2} \quad (3.1)$$

The Blasius' empirical friction law in the turbulent regime is also shown for a comparison. The laminar solution depends on η . In the laminar solution of $C_f = 8C_\eta/Re_m$, the definition of C_η is as follows:

$$C_\eta = \frac{1 - 2\eta + \eta^2}{1 + \eta^2 + \frac{1-\eta^2}{\ln \eta}} \quad (3.2)$$

With respect to the cPf and the pPf as the limiting cases of the aPf, C_η values are 1.0 and 1.5 , respectively. In order to facilitate an easy understanding of the transition process, the product $Re_m C_f$ as a function of Re_m is also plotted in Fig 3.9 (b) and (c). The friction factor at the high Reynolds numbers are in agreement with the empirical function. Furthermore, C_f maintained high value even at lower Reynolds numbers in the transitional regime, when the flow is accompanied by the helical turbulence (for $\eta = 0.5$ and 0.8). However, given the localization of helical turbulence in the x direction and the emergence of a helical puff, C_f deviated from the empirical function towards a laminar solution, as seen at $Re_\tau = 52$

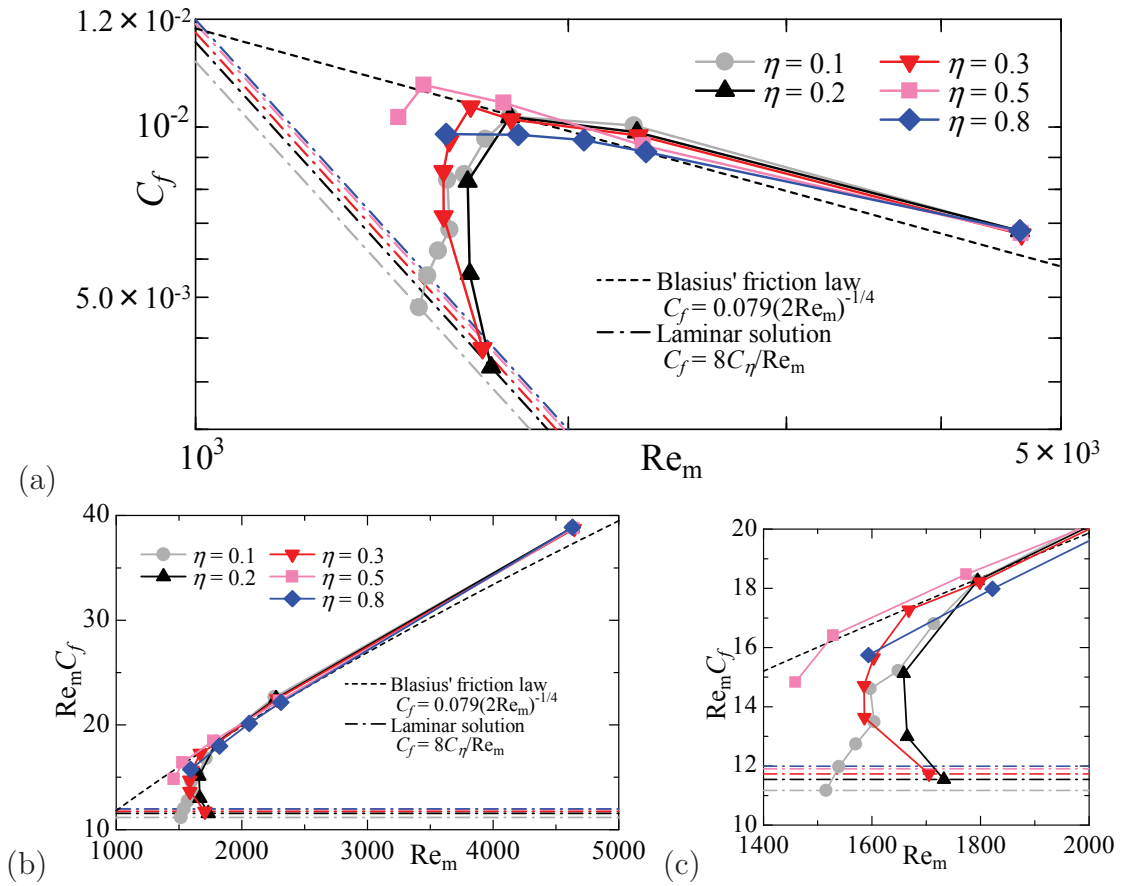


Fig. 3.9 (a) Friction factor C_f , (b) product of $Re_m C_f$, and (c) extended figure of $Re_m C_f$ around the transitional regime.

($Re_m = 1460$) for $\eta = 0.5$. With respect to intermediate η of 0.2–0.3, C_f maintained a high value similar to that for high η . This must be also because of the presence of helical turbulence or helical puff. A further decrease in Re_τ induces a sudden drop of C_f , retaining the same values of Re_m and gradually approaches a laminar solution. It should be noted again that the present flow system is driven by a fixed mean pressure gradient and Re_m depends on the flow state. Under such a condition, once a relaminarization occurs, the bulk Reynolds number Re_m should increase significantly with a fixed Re_τ and lowered C_f . In this sense, there exists an overlapping region around Re_g for $\eta = 0.2$ and 0.3. This must be caused by the alternations of transitional structures from helical turbulence to puffs through helical puff, due to decreases in Re_τ for moderate η . With respect to $\eta = 0.1$, C_f gradually decreased with the Reynolds number after the occurrence of the straight puff. There is no overlapping region, unlike that observed for intermediate η ($\eta = 0.2$ and 0.3) because the transitional structure does not change from straight puff at any Reynolds number for $\eta = 0.1$.

As described above, C_f in the transitional regime considerably depends on the form of transitional structure. Similar aspects can be confirmed from the turbulent fraction that is given in Fig. 3.1. Both C_f and F_t would maintain magnitudes as high as those of featureless

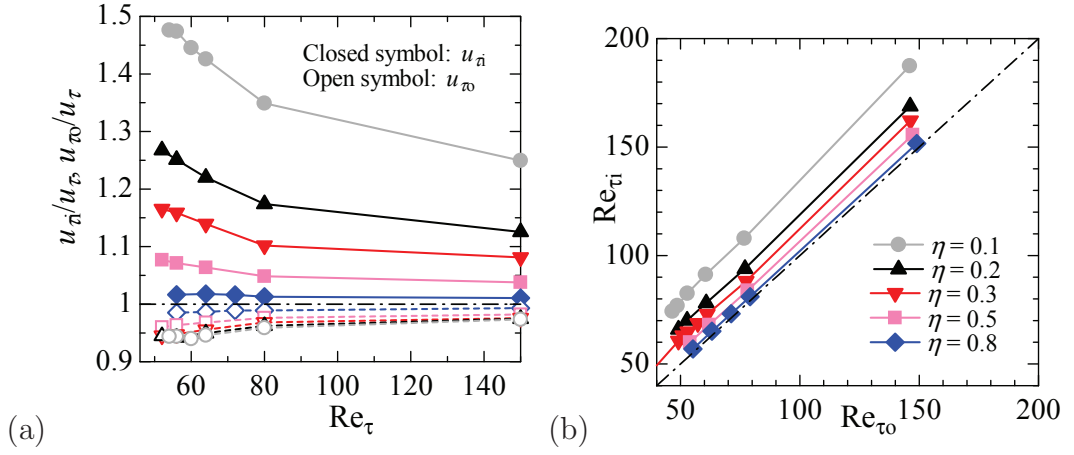


Fig. 3.10 (a) Friction velocity on the inner and outer cylinders ($u_{\tau i}$ and $u_{\tau o}$) as a function of Re_m . (b) Comparison of the friction Reynolds number based on the inner friction velocity *versus* the friction Reynolds number based on the outer friction velocity. If $\eta = 1$, it should be $Re_{\tau i} = Re_{\tau o}$.

turbulence, if the transitional structures forms helical pattern. Such an enhancement of turbulence contributions is weakened in the following order: helical turbulence \rightarrow helical puff \rightarrow straight puff.

Figure 3.10 shows the local friction velocities at the inner and outer cylinders (denoted by $u_{\tau i}$ and $u_{\tau o}$, respectively) and the ratio of the friction Reynolds number on the inner and outer cylinders (denoted by $Re_{\tau i}$ and $Re_{\tau o}$, respectively). The difference between $u_{\tau i}$ and $u_{\tau o}$ increases at low Re_{τ} and small η when compared to the difference at high Re_{τ} and large η . Specifically, the difference enlarges noticeably when $Re_{\tau} = 80 \rightarrow 64$, which corresponds to a shift of the regime from the featureless turbulence to a transitional state of helical/straight puff. On the outer-cylinder side, $u_{\tau o}$ does not depend much on both η and Re_{τ} , and it is approximate to the global friction velocity u_{τ} . In contrast, $u_{\tau i}$ is significantly different from u_{τ} and dependent on η and Re_{τ} . The distribution of the ratios of the friction Reynolds number for all values of η was almost a linear distribution, as shown in Fig. 3.10(b). This implies a less dependency of the ratio $Re_{\tau i}/Re_{\tau o}$ on the global Reynolds number (Re_{τ}).

Here, let us briefly describe a background mechanism of the high friction velocity, i.e., the large velocity gradient, on the inner-cylinder wall, which can be seen in Figs. 3.10(a) and 3.11. In the aPf, the inner cylinder should be associated with a large number of intensive sweep and ejection events that can be attributed to the transverse curvature effect (Liu et al., 2004). In addition, elongated streaky structures near the inner wall are more active than those along the outer wall. The turbulent motions on the outer wall are similar to those near the wall of the cPf and the pPf. These phenomena have also been studied by Satake & Kawamura (1995). They discovered that a high-speed fluid impinging against and across the inner rod would form a wake-like region behind the rod and a large-

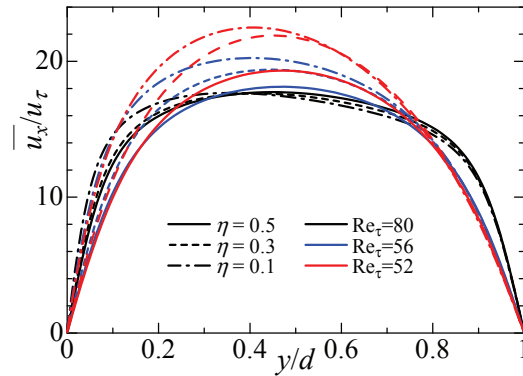


Fig. 3.11 Mean streamwise velocity profiles. The line types indicate different η , and the colors correspond to different values of Re_τ . The inner-cylinder wall corresponds to $y/d = 0$, while the outer one is at $y/d = 1$.

scale wall-normal motion in the large low-pressure region. This distinctive turbulent event increases the friction Reynolds number on the inner cylinder, and this phenomenon leads an asymmetric profile especially for low η . The asymmetric properties are discussed also in the following sections.

3.2.3 Mean flow statistics

The mean velocity profiles are presented in Fig. 3.11. In the figure, the profiles of $\overline{u_x}$ are slightly tilted toward the inner cylinder ($y/d = 0$) showing asymmetric distributions with respect to the gap center. For large values of η , the distributions are rather symmetric at any Re_τ , and similar to the mean velocity profile in the pPf. The peak position shifts to the inner cylinder side, in particular, for low η . As for the Reynolds-number effect, the peak of $\overline{u_x}$ does not move so much when Re_τ decreases from 56 to 52, but both the peak value and the bulk velocity (normalized by u_τ) increase noticeably. This is because those flows are already in the intermittent state and a decrease in the Reynolds number would expand laminar regions. In terms of transitional structures among the helical turbulence and the helical/straight puffs, any significant difference cannot be observed in the $\overline{u_x}$ profiles. However, with respect to the decreasing Re_τ from 80 to 56, the peak position of $\overline{u_x}$ moved towards the gap center ($y/d = 0.5$) and the asymmetric property is suppressed particularly for low $\eta = 0.1$. This implies that the asymmetric property of the core region would be moderated in the transitional regime accompanied by large-scale intermittent structures, while featureless turbulence at a high Reynolds number reveals an asymmetric $\overline{u_x}$ profile due to the aPf geometry. Because of this, the $\overline{u_x}$ profile in the transitional aPf even for $\eta = 0.1$ is more dissimilar to the cPf, in which $\overline{u_x}$ has a peak at $y/d = 1$ and decreases monotonically with $y/d \rightarrow 1$. However, both flows exhibit straight puffs, as shown in Fig. 3.7(f–h). It is interesting to note that the flow statistics including the mean velocity profile in the subcritical regime were dissimilar to the cPf, although the flow structure is

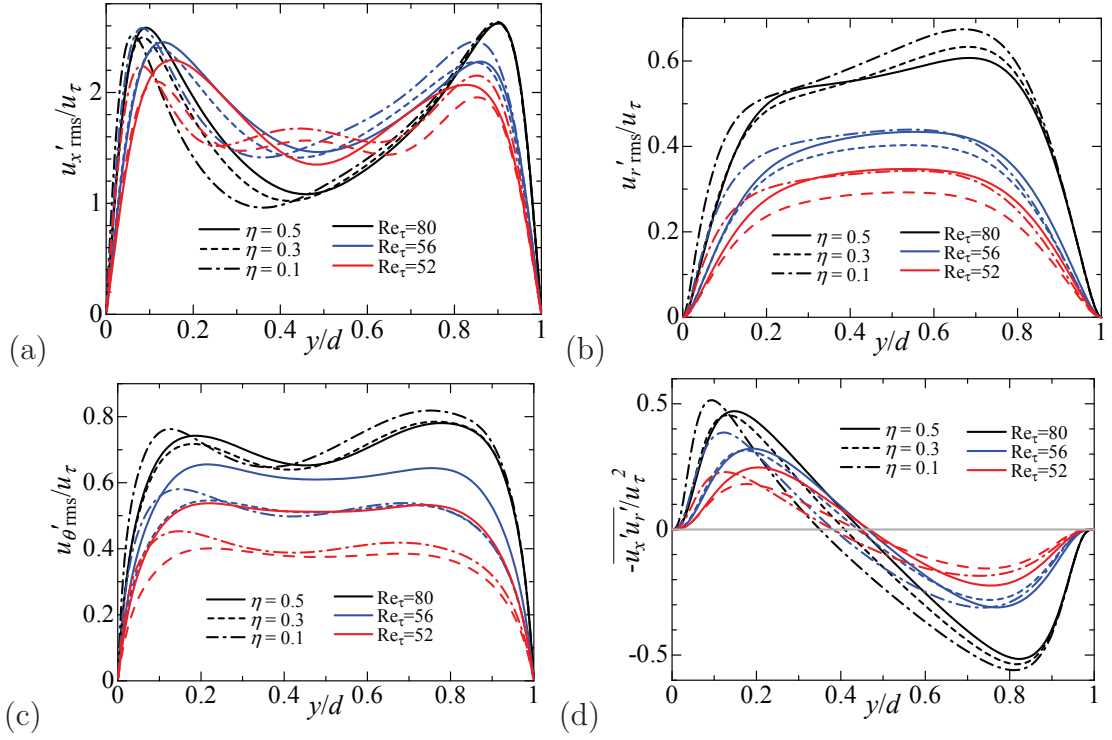


Fig. 3.12 Root-mean-square values of (a) streamwise, (b) wall-normal, and (c) azimuthal velocity fluctuations.

analogous in both flows.

Figure 3.12 shows the root-mean-square value of each fluctuating velocity component. In (a), the streamwise turbulent intensity $u'_{x,rms}$ shows asymmetric distributions with two clear peaks near the inner and outer cylinders. The difference between the two peaks increases with smaller values of η , and the peak near the inner cylinder is larger than that near the outer cylinder. It should be noted that, if scaled with each friction velocity (either $u_{\tau i}$ or $u_{\tau o}$), the inner peak of $u'_{x,rms}/u_{\tau i}$ is much lower than the outer one of $u'_{x,rms}/u_{\tau o}$. In a manner dissimilar to the $\overline{u_x}$, the asymmetricity in a profile is increased at low values of Re_τ as well as η . The two near-wall peaks for the high Re_τ of 80 exhibit the almost same magnitude. At this Reynolds number, the fully-turbulent state might reduce the intensity gap between both sides and, as a result, three curves with different η are roughly matched. This aspect can be similarly seen in the other components. An interesting distribution of $u'_{x,rms}$ is observed at $Re_\tau = 52$ for $\eta = 0.1$ and 0.3 , and a third peak is observed around the gap center. This centerline peak must be attributed to localized (straight) puffs with very-large laminar regions, as shown in Figs. 3.7(f) and 3.8(e).

In Fig. 3.12(b) and (c), $u'_{r,rms}$ and $u'_{\theta,rms}$ indicate skewed profiles with higher peaks near the outer cylinder at a high value of $Re_\tau = 80$. Given decreases in Re_τ , the difference between the peaks near the inner and outer cylinder of $u'_{r,rms}$ decreases and an almost plateau region is observed around the gap center. With respect to this plateau region, we found that the cases in the presence of helical turbulence always provide large $u'_{r,rms}$ and

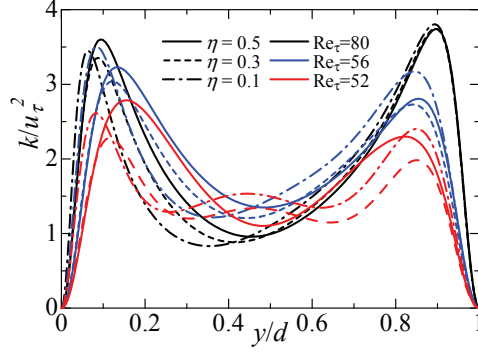


Fig. 3.13 Turbulent energy.

$u'_{\theta\text{rms}}$ compared to the cases of puff. For instance, $u'_{\theta\text{rms}}$ for $\eta = 0.5$ is 10–20% larger than that for $\eta \leq 0.3$, as given in Fig. 3.12(c). These results suggesting an enhanced turbulent intensity in the helical turbulence are in consistency with the above-mentioned high C_f in the transitional regime. A high value distribution of $u'_{\theta\text{rms}}$ near the inner cylinder is the same trend with that of $u'_{x\text{rms}}$ for low η .

Figure 3.12(d) shows the Reynolds shear stress ($-\overline{u'_x u'_r}$). The radial position of the zero Reynolds shear stress moves slightly towards the inner cylinder for low values of η , while the zero value for the pPf should be located at the center of the gap. The zero position shifted to the channel center with a decrease in the value of Re_τ from 80 to 56, as does the peak position of $\overline{u_x}$ (Fig. 3.11). The zero position approaches the center of the gap even for low values of η with decreases in the Re_τ . With respect to the magnitude of Reynolds shear stress, we may detect tendencies similar to those in the turbulent intensity: the larger peak near the inner cylinder for low η , the weakening due to decay from featureless turbulence, and the enhancement by a presence of helical turbulence.

Figure 3.13 shows the turbulent energy, denoted by $k = (u_x^2 + u_r^2 + u_\theta^2)/2$. As widely known, turbulent motion is vigorous near the wall. With respect to the aPf, the turbulence is more activated near the inner cylinder than near the outer cylinder. In contrast, the peak of k near the outer cylinder is slightly higher only at the high value of $\text{Re}_\tau = 80$. Therefore, this enhanced turbulent fluctuation near the inner cylinder was prominent when the transitional structure occurred. Note again that, in terms of normalization by each wall units, the magnitude of k becomes lower on the inner cylinder side than on the outer side. It may implies that the near-wall coherent structure common to plane-wall turbulence may tend to be absent near the inner cylinder, in particular, under the transitional state. Hanks et al. (1971) proposed a picture of the dual flow, i.e., the first transition from the inner-cylinder side, in the aPf. In contrast, our DNS have demonstrated no dual flow and shown a less active turbulence near the outer cylinder wall. For $\eta = 0.1$, the streamwise localized puff with a large laminar regime led to high fluctuations around the gap center, as discussed in the distribution of $\overline{u_x}$.

3.3 Transition between straight and helical puff

Up to this section, transitional structures depending on radius ratio and effects of transitional structures on the flow statistics have been described. We find that the transitional structures in the aPf bridge the structures in two different flow systems of the cPf and the pPf. In this section, the connection between the straight puff and helical puff is considered quantitatively. Firstly, the flow regime of the straight puff and helical puff is reintroduced by showing the time development of structures and flow visualizations. Then, we consider the effect of azimuthal length and the difference between the straight puff and the helical puff, scrutinized using the probability density function of an azimuthal large-scale flow.

3.3.1 Temporal dynamics of localised turbulent structures

The temporal dynamics of the straight and the helical puff is described using a space time diagram of azimuthal-averaged streamwise velocity ($\langle u_x \rangle |_{\theta} = \int_0^{2\pi} u_x d\theta$) at the center of the gap in Figs. 3.14, 3.16, and 3.18 for $\eta = 0.1, 0.2,$ and 0.3 . The horizontal axis shows the streamwise distance (of a moving frame of reference) and the vertical axis is time. In the space time diagram, the red and blue regions correspond to turbulent and laminar state. Figures 3.15, 3.17, and 3.19 show two-dimensional contours of wall-normal velocity fluctuations at the gap center in the x - θ plane at an arbitrary time of $Re_{\tau} = 52$ for each $\eta = 0.1, 0.2,$ and 0.3 .

For $\eta = 0.1$, the classical intermittent sequences of turbulent puffs are recognized, as in Figure 3.15. The interaction between localized puffs is best understood from (x, t) diagrams in Fig 3.14.

For $Re_{\tau} = 56$, the flow consists of a train of four to five several puffs dynamics interacting via sequences of replication and merging events. At $Re_{\tau} = 52$ and 50 , the number of puffs interacting drops to two or three, with relaminarisation or replication (“splitting”) events occurring on longer timescales and no merging event. For $Re_{\tau} = 48$, a single isolated puff survives over the whole observation time, though at several occasions its internal fluctuations bring it close to splitting or to collapsing. For $Re_{\tau} = 46$, the isolated puff is tempted to split into two parts that collapse both after less than $5d/u_{\tau}$. This description is completely consistent with that of turbulent puffs in circular pipe flow in Moxey and Barkley, (2010), Avila et al. (2011), and Shimizu et al. (2014). This suggests that the transition is continuous, with the critical point Re_{τ} for this value of η lying around 48 ± 1 .

The spatiotemporal diagrams for $\eta = 0.2$ at $Re_{\tau} = 56, 52,$ and 50 in Fig. 3.16(a-c) do not differ much from those for $\eta = 0.1$, except perhaps at $Re_{\tau} = 56$ where the turbulent flow exhibits a stronger tendency toward patterning (emergence of a well-defined streamwise wavelength) than for lower η . For $\eta = 0.2$, the puff sustaining at $Re_{\tau} = 52$ may split and avoid its decay, while the puff at $Re_{\tau} = 50$ decays completely. This suggests a critical point around $Re_{\tau} = 51 \pm 1$. The spatial fluctuations of $u'_r(x, z)$ at mid-gap in Fig. 3.17 show a

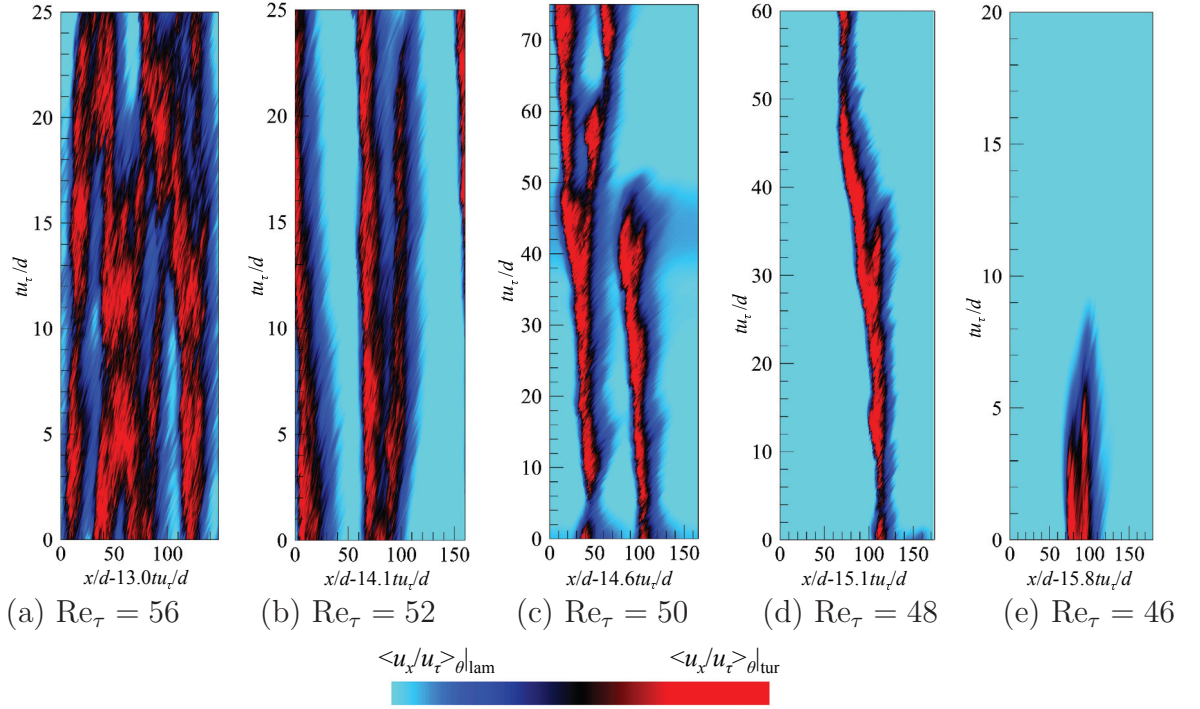


Fig. 3.14 Space-time diagram of azimuthally-averaged streamwise velocity at mid-gap for $\eta = 0.1$ and different $Re_\tau =$ (a)56, (b)52, (c)50, (d)48 and (e)46. Colormap of $(\langle u_x/u_\tau \rangle|_{\text{tur}}, \langle u_x/u_\tau \rangle|_{\text{lam}})$: (a) (18, 22), (b) (19, 24), (c) (20, 25), (d) (21, 25), and (e) (21, 25).

surprising property: some of the laminar-turbulent interfaces identified display obliqueness with respect to the streamwise direction while other do not.

Similar data for $\eta = 0.3$ confirms above-mentioned trend, with an even stronger patterning property and the same critical value: Fig. 3.18(c) provides a particular evidence that, for $Re_\tau = 50$, three puffs separated by a comparable wavelength collapse in synchrony. The occurrence of oblique laminar-turbulent interfaces appears also more pronounced, judging from the fluctuations of u'_r shown in Fig. 3.19.

The resulting intermittent regime for $\eta=0.2$ and 0.3 appears hence as a mixture of both classical straight puffs analogous to those found for $\eta = 0.1$, and helical puffs as identified in the previous section in shorter domains. We insist on the coexistence in space as in time

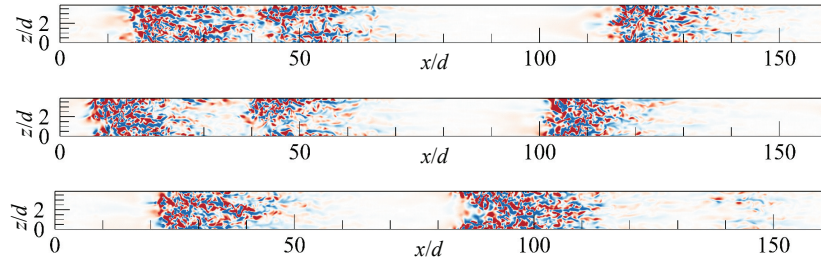


Fig. 3.15 Two-dimensional contours of instantaneous u'_r/u_τ at mid-gap for $\eta = 0.1$ at $Re_\tau = 52$ at different time. Contours range from -0.5 (blue) to 0.5 (red).

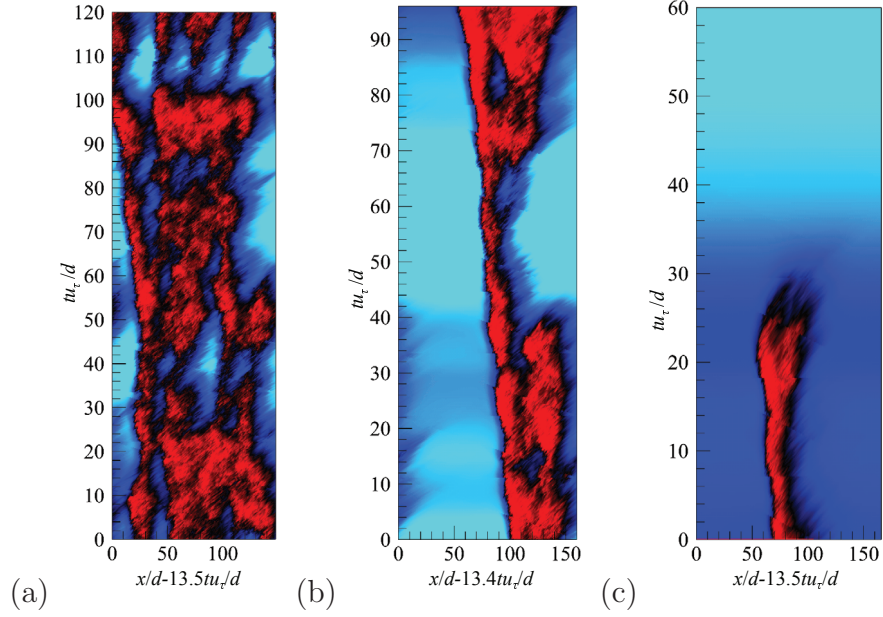


Fig. 3.16 Space-time diagram of azimuthally-averaged streamwise velocity at mid-gap for $\eta = 0.2$ and different $Re_\tau =$ (a)56, (b)52, and (c)50. Colormap of $(\langle u_x/u_\tau \rangle_\theta|_{\text{tur}}, \langle u_x/u_\tau \rangle_\theta|_{\text{lam}}) =$ (a) (18, 23), (b) (20, 25), and (c) (20, 27).

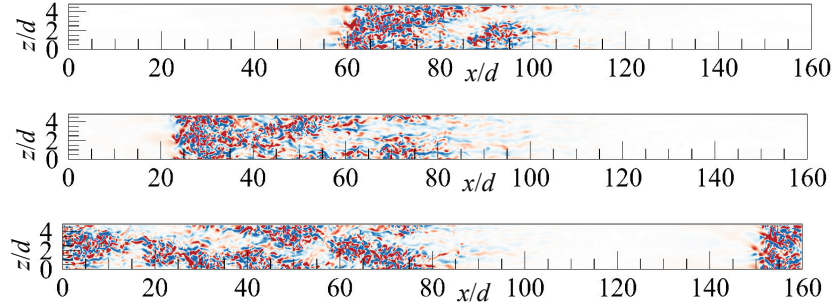


Fig. 3.17 Two-dimensional contours of instantaneous u'_r/u_τ at mid-gap for $\eta = 0.2$ at $Re_\tau = 52$ at different time. Contours range from -0.5 (blue) to 0.5 (red).

and for a given set of parameters, of both types of structures. This immediately suggests that the transition from (straight) puffs to (oblique/helical) stripes cannot be treated as deterministic, but rather requires a statistical treatment. Some statistical analysis to be presented in following subsections are based on the probability density function of large-scale azimuthal velocity that is related to the obliqueness of pattern.

3.3.2 Azimuthal length depending on radius ratio

Bifurcations from one turbulent regime to another one are difficult to investigate because, unlike for bifurcations of exact steady/periodic states, the presence of turbulent fluctuations both in time and space makes the choice of a well-defined bifurcation param-

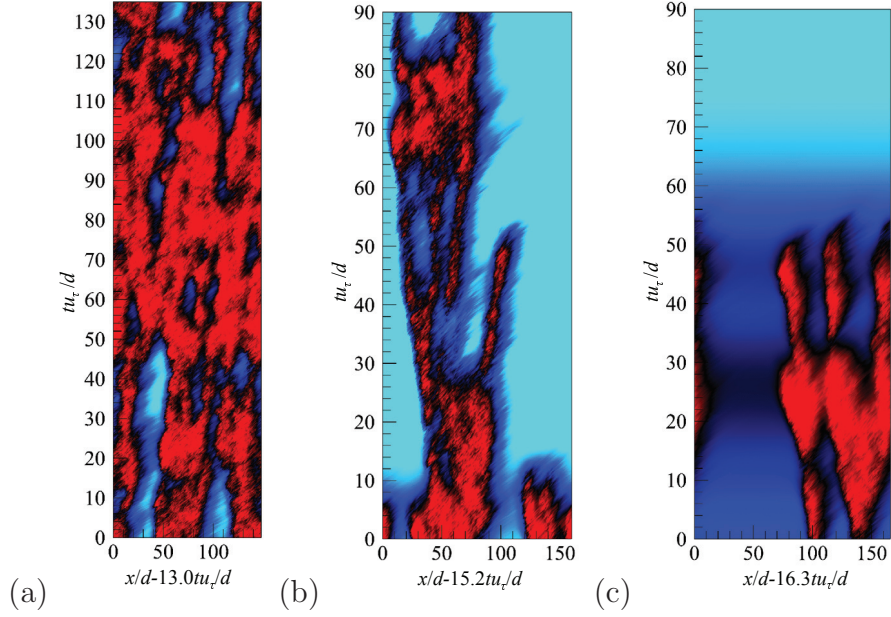


Fig. 3.18 Space-time diagram of azimuthally-averaged streamwise velocity at mid-gap for $\eta = 0.3$ at different $\text{Re}_\tau =$ (a) 56, (b) 52, and (c) 50. Colormap of $(\langle u_x/u_\tau \rangle_\theta|_{\text{tur}}, \langle u_x/u_\tau \rangle_\theta|_{\text{lam}}) =$ (a) (18, 22), (b) (19, 23), and (c) (19, 26).

eter non obvious. Moreover, we intend here to characterize the bifurcation of the shape of coherent structures, where no particularly obvious Eulerian indicator emerges to describe for instance the obliqueness of the interfaces. We suggest to link the present study to the limiting planar case $\eta \rightarrow 1$, which has been already discussed in Duguet and Schlatter (2013), and to generalize it to curved geometries corresponding to $0 < \eta < 1$. This represents an opportunity to test the limitations of the planar theory in the presence of finite curvature. Moreover, we keep in mind the observation that both types of structures, straight or helical, have been detected for the same parameters at intermediate values of η . The relevant bifurcation parameter chosen should hence be quantified in a probabilistic manner, with statistics carried out, for each set of parameters η and Re_τ , over both time

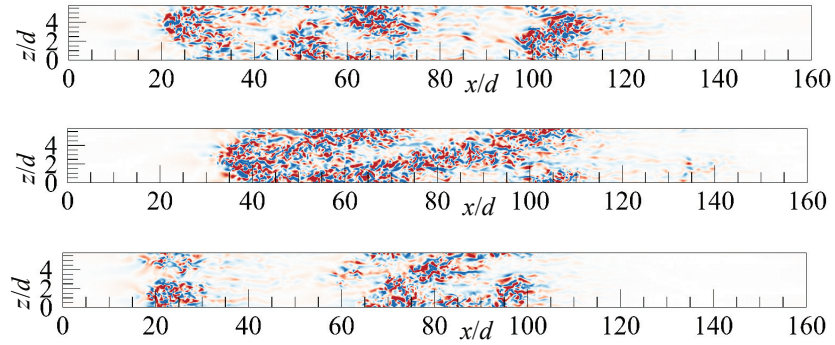


Fig. 3.19 Two-dimensional contours of instantaneous u'_r/u_τ at mid-gap for $\eta = 0.3$ at $\text{Re}_\tau = 52$ at different time. Contours range from -0.5 (blue) to 0.5 (red).

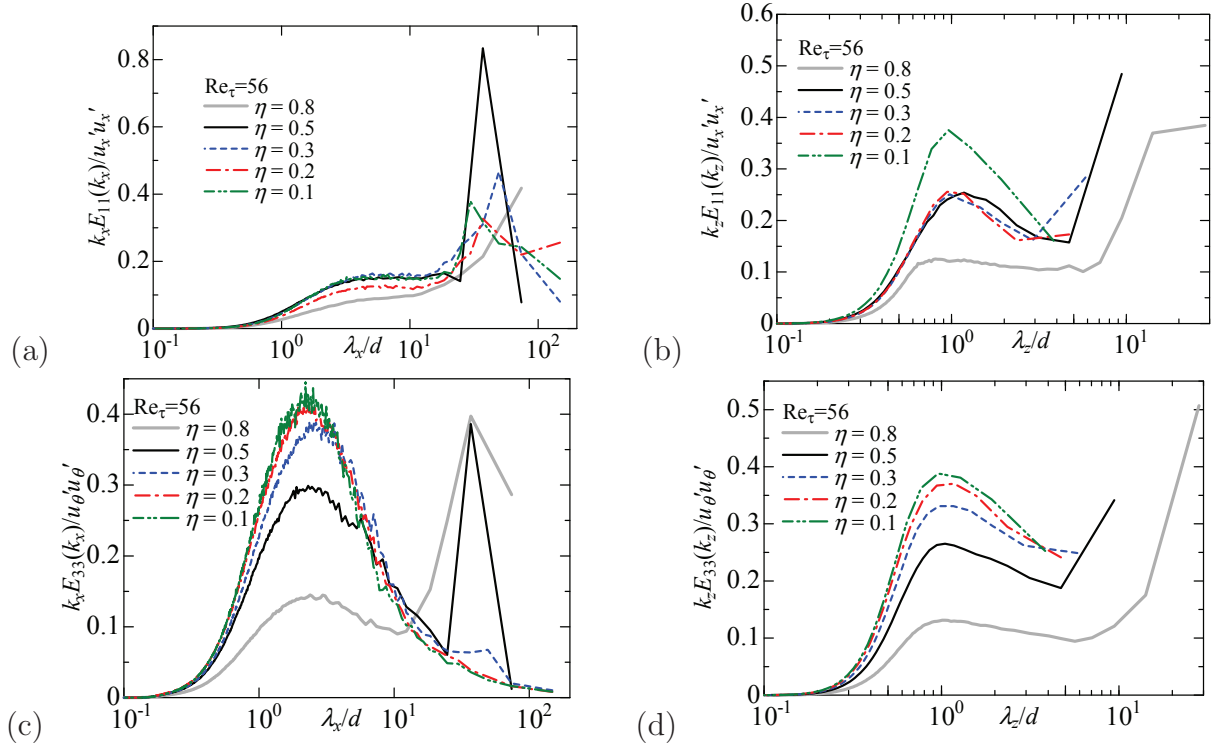


Fig. 3.20 Pre-multiplied energy spectra for u'_x and u'_θ as a function of either wavelength λ_x/d or λ_z/d at mid-gap: (a) streamwise spectra of u'_x , (b) spanwise spectra of u'_x , (c) streamwise spectra of u'_θ , and (d) spanwise spectra of u'_θ . The streamwise and azimuthal wavenumbers are defined as $k_x = 2\pi/\lambda_x$ and $k_z = 2\pi/\lambda_z$, respectively. The spectra are normalized by an ensemble-averaged value of $u'_i u'_i$ at mid-gap

and space.

For planar flows, it was suggested in Duguet and Schlatter (2013) that the obliqueness of interfaces could be explained qualitatively by the existence of large-scale flows. In the presence of a sufficiently marked scale separation between small scales (the turbulent fluctuations) and large scales, it was shown analytically that large scales advect the small scales of weakest amplitude. Interfaces between laminar and turbulent motion correspond precisely to the zones where the fluctuations decay from their turbulent amplitude towards zero. It is thus expected that the planar orientation of the interface corresponds precisely to the orientation of the large-scale flow advecting the small scales at the edges of the turbulent patches. In particular the global angle of the periodic stripe patterns corresponds accurately to the angle of the large-scale flow: a non-zero angle is linked with the existence of a spanwise component for the large scales.

In order to evaluate which large-scale components are present here, time-averaged pre-multiplied energy spectra evaluated at gap center are shown in Fig. 3.20 for $Re_\tau = 56$ (for which all flows are spatially intermittent) and different values of η from 0.1 to 0.8. Careful analysis of Fig. 3.20 reveals robust features. Small scales associated with turbulent fluctuations are present around $\lambda_x/d \approx 2-3$ and $\lambda_z/d \approx 1$ in all directions for all

components. The situation is different for large-scale velocity components: out of the four figures, only u_x as a function of x displays large scales for all value of η . These large scales do not appear strongly separated from the smaller ones, and are located at $\lambda_x/d \approx 15\text{--}70$. Neither u_θ as a function of either x or θ , nor u_x as a function of θ , possesses such a robust large-scale component. As η exceeds 0.3, well-separated peaks at similar large scales emerge in each spectrum. Important informations can be deduced from these spectra. First, should large-scales be found, the corresponding cut-off can be located safely in the intervals $\lambda_x/d \approx 10\text{--}20$ and $\lambda_z/d \approx 2\text{--}5$. Secondly, by construction the wavelengths in the spectra are limited by the box dimensions L_x and L_z . A clear difference emerges between Figs. 3.20(a, c) on one hand (showing the λ_x dependence), and Figs. 3.20(b, d) on the other hand (showing the λ_z dependence). In other words, the spanwise large-scale component is present only for sufficient azimuthal extent, whereas streamwise large-scale modulations are always present as long as the flow features spatial intermittency. We emphasize here that the azimuthal extent should be measured in units of $d = r_o - r_i$, since streaks and streamwise vortices (forming the small scales) scale with the gap size d rather than with any of the two radii r_o or r_i . (The wall unit is another candidate, but large-scale structures of interest should be generally scaled with outer units.) Our hypothesis here is that the occurrence of azimuthal large-scale flows depends on the azimuthal extent L_z/d , itself a function of η .

The quantity L_z however depends on the value of r . It is simpler to focus on the inner and outer azimuthal extents L_{zi} and L_{zo} , given respectively by

$$L_{zi} = 2\pi d \frac{\eta}{1 - \eta} \quad (3.3)$$

$$L_{zo} = 2\pi d \frac{1}{1 - \eta}. \quad (3.4)$$

Both quantities (expressed in units of d) are plotted as functions of the radius ratio η in Fig. 3.21. Let us fix rather arbitrarily a cut-off value of λ_z . The intersection of the horizontal line $L_z = \lambda_z$ with the curves $L_{zo}(\eta)$ and $L_{zi}(\eta)$ in Fig. 3.21 defines two values of η , respectively η_1 and η_2 . This leads to three distinct ranges of values for η :

- for $0 < \eta \leq \eta_1$, there is no space for large scales in the azimuthal direction, neither at the inner not at the outer wall.
- for $\eta_2 \leq \eta \leq 1$, azimuthal large scales can form at both inner and outer walls. The situation is then analogous to the planar case.
- for $\eta_1 \leq \eta \leq \eta_2$, the situation is mixed: azimuthal large scale flows cannot be accommodated at all locations in the cross-section. A probabilistic approach is required.

For instance, choosing a cut-off value $\lambda_z = 3\pi$ leads to $\eta_1 = 1/3$ and $\eta_2 = 3/5$, which is consistent with our observations. While the classification above is not useful in practice to predict accurately the transition thresholds η_1 and η_2 (mainly because of the difficulty to

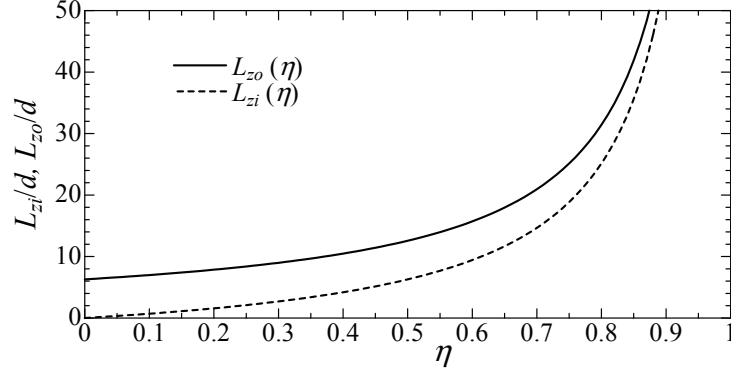


Fig. 3.21 Azimuthal length as a function of radius ratio.

define a unique cut-off value $\lambda_z(\text{Re}_\tau)$, it captures the main physical idea: the presence of confinement in the azimuthal direction defines the two extreme regimes of straight interfaces (associated with puffs) or oblique interfaces (associated with oblique stripes), and there is a range of value of η for which there is a probability to observe both types of interfaces (and hence both puffs and stripes) in the same flow at different times and/or different positions.

It can be useful to investigate cross-sections of the flow in the different regime to understand the implications of the previous hypothesis. The two-dimensional contours of u'_x and u'_θ in arbitrary chosen r - θ cross-sections are shown in Figs. 3.22 and 3.23 for different values of η .

The isocontours of u'_x in Fig. 3.22 allow one to count the numbers of streaks present in the vicinity of each wall. Each of these streaks has a radial and azimuthal extent $\approx /2d$, and the analysis of the spectra in Fig. 3.20 also suggests that their streamwise extent is approximatively $2d$. In principle one would expect the streak size to scale in inner units ν/u_τ , however the range of values of Re_τ investigated here is relatively narrow and we prefer to report the dimensions of the streaks in (outer) units of d , as the relation $\lambda_z \approx d$ emphasizes their quasi-circular cross-section. In the case of the straight puffs found for $\eta = 0.1$, u'_x is almost axisymmetrically distributed, and two or six high-speed streaks can be found in the azimuthal direction. With increasing η , the number of streaks increases as the azimuthal extent increases, a supplementary confirmation that the relevant length-scale here is d rather than r_o or r_i . For $\eta = 0.4, 0.5$ and 0.8 (Fig. 3.22(d, e, f)), the non-axisymmetric modulation of u'_x is the direct signature of the helix-shaped turbulence. To a lesser degree, such a modulation can also be visually detected for $\eta = 0.2$ and 0.3 (Fig. 3.22(b, c)). Similar conclusions can be drawn from the isocontours of u'_θ in Fig. 3.23 as well.

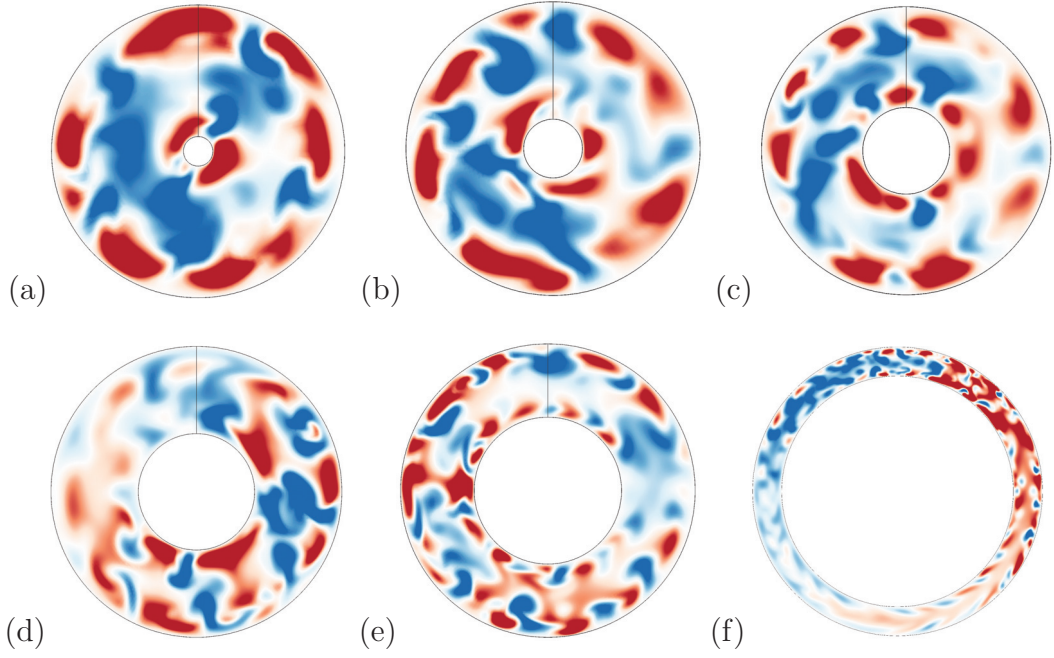


Fig. 3.22 Two-dimensional cross-sections (r, θ) of instantaneous u'_x for $\eta =$ (a) 0.1, (b) 0.2, (c) 0.3, (d) 0.4, (e) 0.5, and (f) 0.8 at $\text{Re}_\tau = 52$. Colourmap from $-3.0u_\tau$ (blue) to $+3.0u_\tau$ (red).

3.3.3 Probability density function of azimuthal velocity

This section is now devoted to a quantitative investigation of the orientation of the large-scale flow near the interfaces for varying radius ratio η . We begin by describing in more detail how data from the previous direct numerical simulations is post-processed. Based on the apparent scale separation in the spectra from Fig. 3.20, we consider a low-pass filter L whose kernel in spectral (k_x, k_θ) space reads

$$|k_x| \leq \frac{2\pi}{20d}, \quad |k_z| \leq \frac{2\pi}{2d} \quad (3.5)$$

The original velocity fields $u_i(r, \theta, x, t)$ are transformed via L into filtered fields $U_i(r, \theta, x, t)$. The two-dimensional wall-integrated large-scale flow (\bar{U}_θ) is then computed using the following definition.

$$\bar{U}_\theta = \int_{r_i}^{r_o} U_\theta d\theta. \quad (3.6)$$

Statistics of \bar{U}_θ have been gathered for all parameters over the numerical grid (x_i, z_j) and over different times. Since we are mainly interested in the values of \bar{U}_θ at the laminar-turbulent interfaces, we exclude from the statistics fully laminar portions of the flow which would overestimate the statistical weight of the $\bar{U}_\theta \approx 0$ contribution. This is achieved by conditioning all statistics by the additional constraint $|u'_r|/u_\tau > 0.2$ (which is never fulfilled in laminar zones where $u'_r \approx 0$). Probability distribution function (PDF) for $|\bar{U}_\theta|$ is obtained by considering bins of width $\Delta\bar{U}_\theta = 0.025$.

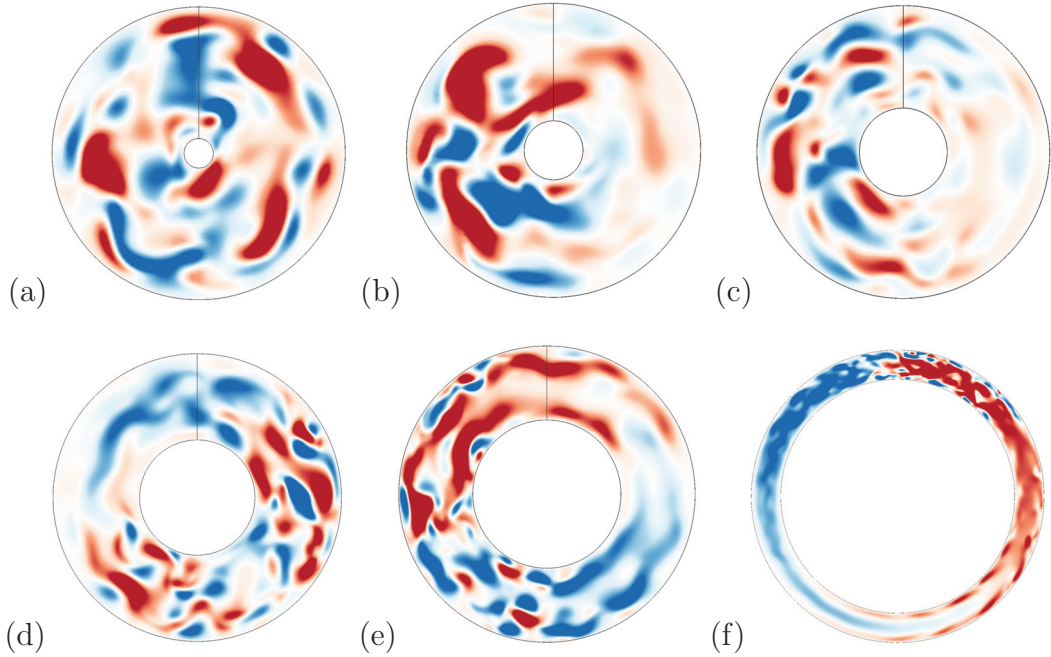


Fig. 3.23 Two-dimensional cross-sections (r, θ) of instantaneous ru'_θ for $\eta =$ (a) 0.1, (b) 0.2, (c) 0.3, (d) 0.4, (e) 0.5, and (f) 0.8 at $\text{Re}_\tau = 52$. Colourmap from $-1.0u_\tau$ (blue) to $+1.0u_\tau$ (red): the positive direction of θ is clockwise in the plots.

We first describe the PDF of $|\overline{U}_\theta|$ (normalised by u_τ) obtained for several values of η and parametrised by Re_τ , shown in Fig. 3.24.

For $\eta = 0.1$ and above, the PDF looks reasonably Gaussian in the fully turbulent regime at $\text{Re}_\tau = 150$. For $\eta = 0.1$ and 0.2, decreasing Re_τ into the intermittent regime reveals a flatter Gaussian profile for the PDF, still centered at zero. For increasingly high values of $\eta \geq 0.3$, the tendency for the PDF to flatten away from zero becomes stronger, thereby enlarging the range of values of $|\overline{U}_\theta|$. For $\eta = 0.4$, a new peak has emerged in the PDF from the former tail in the range $\overline{U}_\theta = 0.2\text{--}0.3u_\tau$, and this peak outweighs the $\overline{U}_\theta = 0$ contribution. This shows how increasing η beyond 0.4 leads with increasing probability to the emergence of a transverse large-scale flow component, interpreted as responsible for the oblique interfaces observed. Focusing on the lowest values of $\text{Re}_\tau = 52$ and 56 where intermittency has been observed, we plot PDF of $|\overline{U}_\theta|/u_\tau$ parametrised by η in the range 0.1–0.8.

The standard mean deviation σ of $|\overline{U}_\theta|/u_\tau$ is defined by

$$\sigma^2 = \int_0^\infty (|\overline{U}_\theta|/u_\tau)^2 \text{PDF}(|\overline{U}_\theta|/u_\tau) d(|\overline{U}_\theta|/u_\tau), \quad (3.7)$$

and is plotted for different values of η and Re_τ in Fig. 3.25. The widening of the distribution with increasing η appears as a general trend for all values of Re_τ , except for $\text{Re}_\tau = 150$ which corresponds to fully turbulent flow without intermittency (and hence does not feature any sustained laminar-turbulent interface). All other cases illustrate well the general idea: as η increases in the intermittent regime, the azimuthal confinement is reduced, allowing

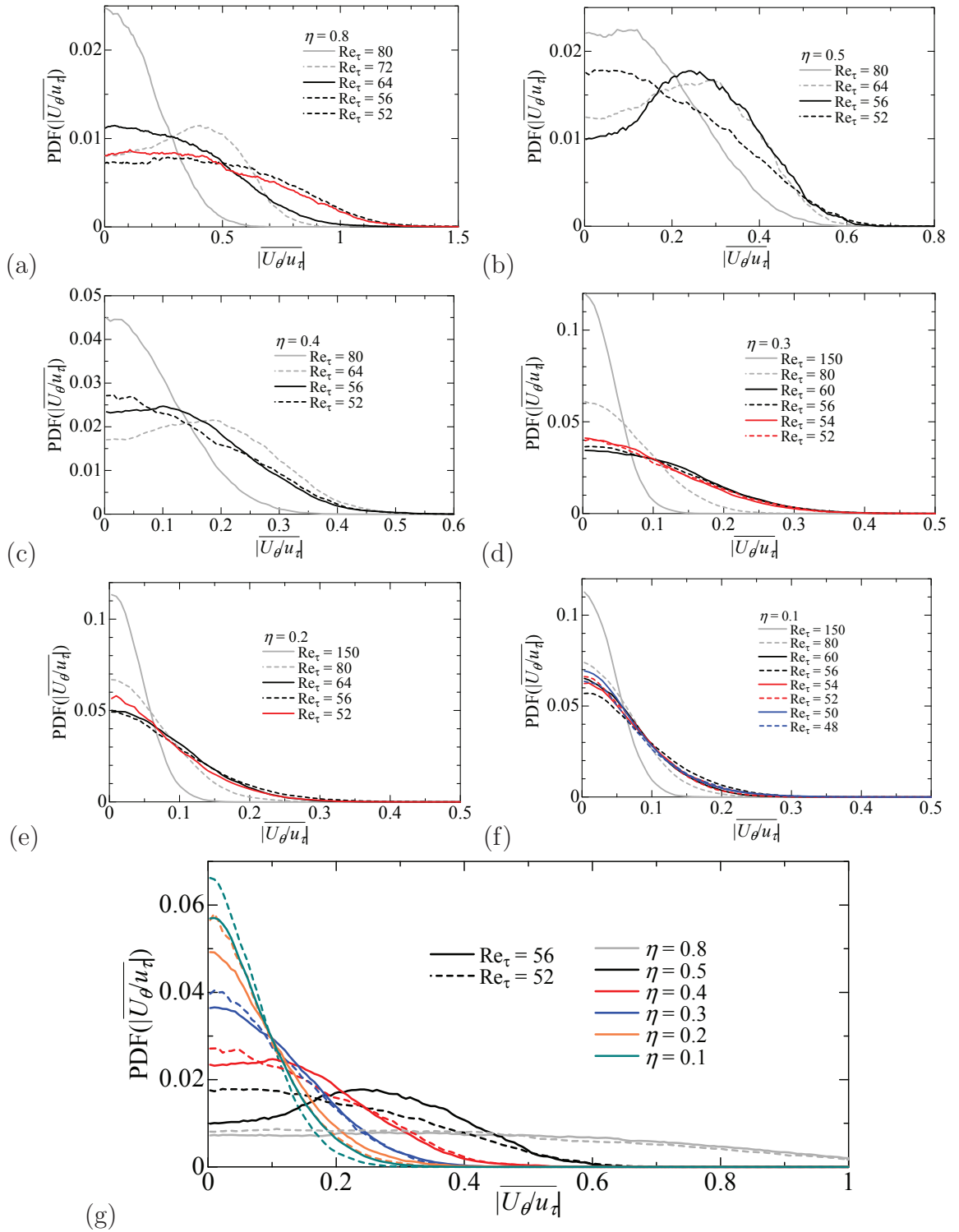


Fig. 3.24 Probability density function for $\eta =$ (a) 0.8, (b) 0.5, (c) 0.4, (d) 0.3, (e) 0.2, and (f) 0.1. The radius ratio dependency is shown in (g).

for larger fluctuations in the orientation of the large-scale flows. When L_{zi} exceeds the natural cut-off of λ_z , large-scale flows with a genuine transverse component $\bar{U}_\theta \neq 0$ emerge and stabilize the oblique patterns. As η is decreased, a probabilistic transition from a well-

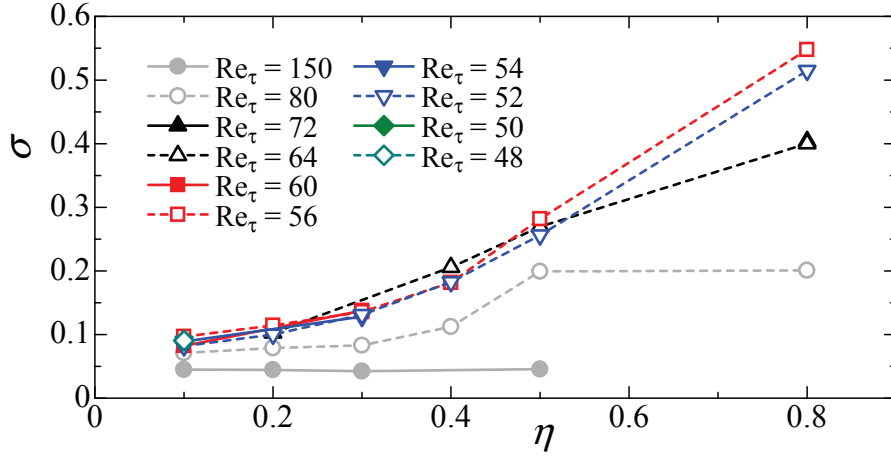


Fig. 3.25 Standard variance of the PDF($\overline{U}_\theta/u_\tau$).

ordered stripe pattern to a disordered sequences of straight puffs featuring occasionally helical puffs. Further reduction of η below 0.2 towards zero is accompanied by a narrowing of the PDF of \overline{U}_θ , corresponding to a increasingly exclusive selection of straight puffs at the expense of the helical ones.

3.4 Modal analysis for laminar-turbulent patterning

Transitional structures in incompressible pressure-driven flows in annulus were investigated and we found various transitional structures, namely straight/helical puffs and helical turbulence. In the previous section, the probability density function of azimuthal velocity was analyzed to determine the transition from straight puff to helical puff. In this section, we consider a new method to obtain the whole transition process in the aPf quantitatively. To this end, mode analysis is performed to extract the dominant mode of streamwise localization, helix, and turbulence (streaks), and classify them by possession of each mode.

3.4.1 Methods (e.g. $\eta = 0.5$)

As an example, we first consider the helical turbulence in the aPf for $\eta = 0.5$. For $\eta = 0.5$, helical turbulence is time independent and is the robust structure at $Re_\tau = 56$ and 64. Therefore, it is very useful to start with this parameter when applying a new method. Figure 3.26 shows two-dimensional contours of streamwise and azimuthal velocity fluctuations (u'_x and u'_θ) in the x - θ plane for $\eta = 0.5$ of $Re_\tau = 56$ at the gap center. Clear oblique turbulent-laminar interfaces are observed as positive and negative u'_x and u'_θ . Firstly, we extract each velocity component of all modes $\hat{u}'_i(m_x, r, m_\theta, t)$ through wavenumber space by Fourier transform from $u'_i(x, r, \theta, t)$. For instance, \hat{u}'_i of (m_x, y, m_θ)

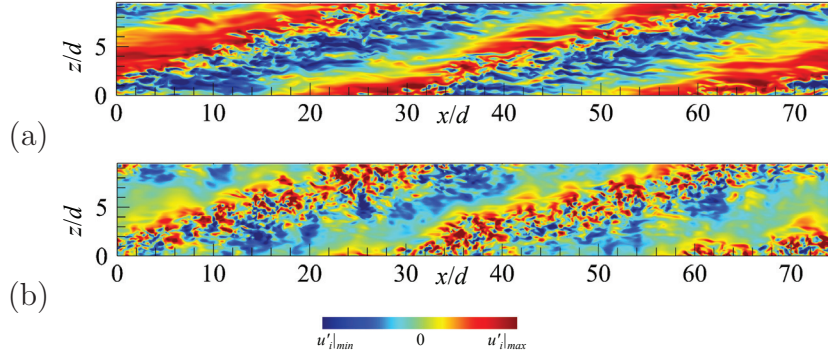


Fig. 3.26 Two-dimensional contours of instantaneous (a) streamwise and (b) azimuthal velocity fluctuations for $\eta = 0.5$ of $Re_\tau = 56$ at the gap center. Color ranges are (a) $(u'_x|_{min}/u_\tau, u'_x|_{max}/u_\tau) = (-3, 3)$ and (b) $(u'_\theta|_{min}/u_\tau, u'_\theta|_{max}/u_\tau) = (-1.5, 1.5)$.

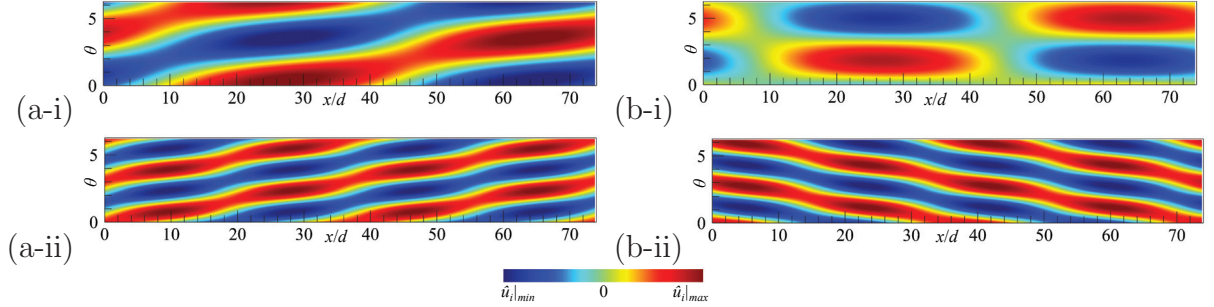


Fig. 3.27 Two-dimensional contours of instantaneous (a) streamwise and (b) azimuthal mode velocity for $\eta = 0.5$ of $Re_\tau = 56$ at the gap center. Modes are $(m_x, m_\theta) =$ (i) (1, 1) and (ii) (2, 2). $(\hat{u}'_i|_{min}/u_\tau, \hat{u}'_i|_{max}/u_\tau)$ are (a-i) $(-0.35, 0.35)$, (b-i) $(-0.015, 0.015)$, (a-ii) $(-0.2, 0.2)$, (b-ii) $(-0.045, 0.045)$.

$= (1, d/2, 1)$ and $(2, d/2, 2)$ at the same time in Fig. 3.26 are displayed in Fig. 3.27. The mode (m_x, m_θ) displays a wavenumber.

Second, to obtain the dominant mode, the mean turbulent intensity of each mode is calculated by following equations (Eqs. (3.8) and (3.9)).

$$\dot{u}_x(m_x, m_\theta) = \int \int_{r_i}^{r_o} \hat{u}'_x{}^2(m_x, r, m_\theta, t) r dr dt \quad (3.8)$$

$$\dot{u}_\theta(m_x, m_\theta) = \int \int_{r_i}^{r_o} \frac{\hat{u}'_\theta{}^2(m_x, r, m_\theta, t)}{u_\tau^2} dr dt \quad (3.9)$$

Figure 3.28 shows two dimensional contours of \dot{u}_x and \dot{u}_θ in the m_x - m_θ plane for $\eta = 0.5$. At high $Re_\tau = 150$, the intensity is broadly distributed. However, a clear peak at $(m_x, m_\theta) = (2, 1)$ is observed at $Re_\tau = 80$ and 56 , and this point may clarify the helical mode irrespective of Re_τ for $\eta = 0.5$ although the streamwise mode m_x depends on the numerical domain. To confirm the reliability of the dominant mode, $(m_x, m_\theta) = (2, 1)$ is only extracted from the instant flow field at the same time in Fig. 3.26. Figure 3.29 shows (a) wall-normal velocity fluctuations u'_r , vectors of wall-normal averaged (b) instantaneous velocity

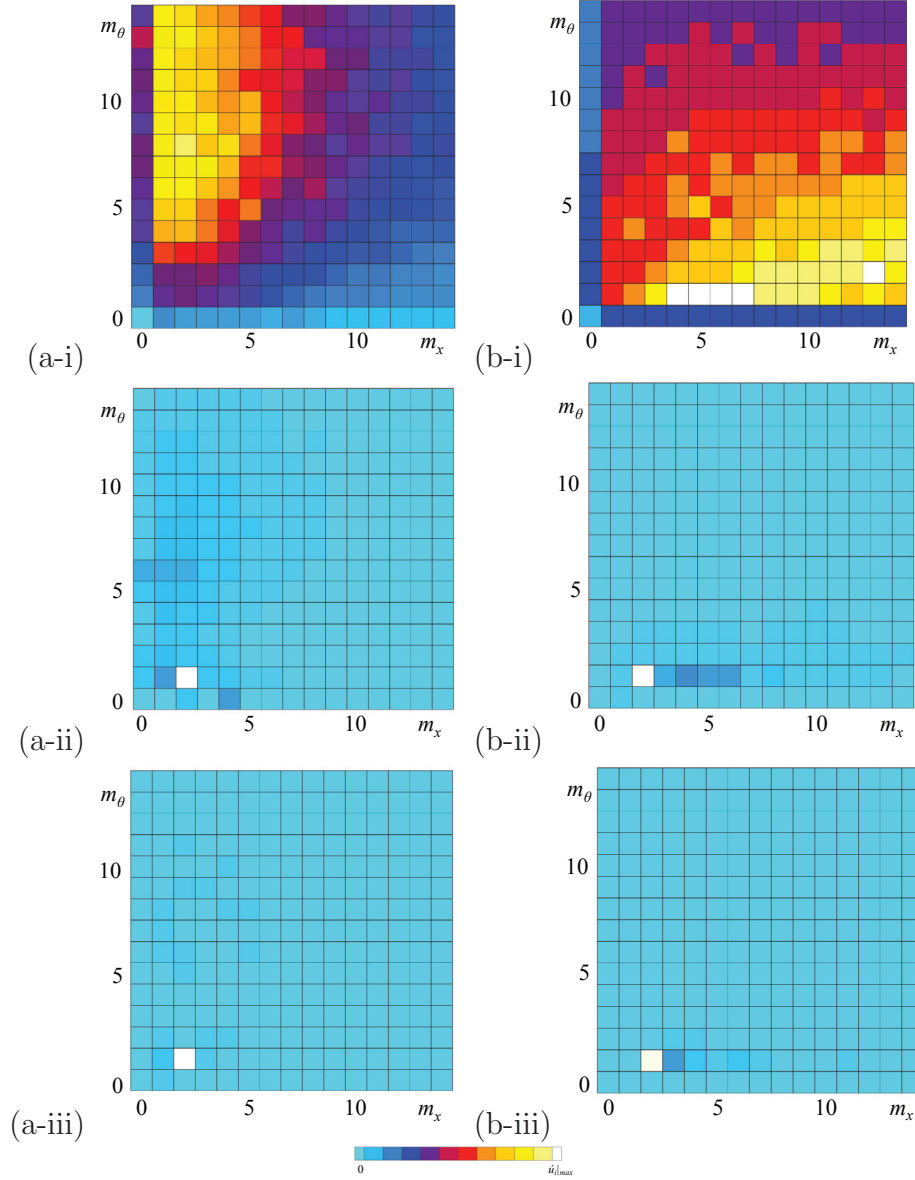


Fig. 3.28 Two-dimensional contours of mean (a) streamwise and (b) azimuthal turbulent intensity (\hat{u}_x and \hat{u}_θ) of each mode for $\eta = 0.5$ at $\text{Re}_\tau =$ (i) 150, (ii) 80 and (iii) 56. ($\hat{u}_i|_{max}/u_\tau$) are (a-i) (0.01), (b-i) (0.001), (a-ii) (0.45), (b-ii) (0.046), (a-iii) (1.3), and (b-iii) (0.1).

($\int_{r_i}^{r_o} u'_x(x, r, \theta) r dr$, $\int_{r_i}^{r_o} u'_\theta(x, r, \theta) dr$), and (c) mode extracted velocity ($\int_{r_i}^{r_o} \hat{u}'_x(2, r, 1) r dr$, $\int_{r_i}^{r_o} \hat{u}'_\theta(2, r, 1) dr$). The row data (b) shows small scale fluctuations observed in and around the turbulent region. In contrast, the extracted data displays only the large-scale flow along the turbulent region corresponding to helical turbulence (c). Therefore, this dominant mode (m_x, m_θ) = (2, 1) can clearly clarify helical mode.

Thirdly, the turbulent intensity of each mode $\hat{u}_x(m_x, m_\theta)$ is averaged along m_x (Eq. (3.10) and (3.11)) because azimuthal mode m_θ is more important than streamwise mode m_x for

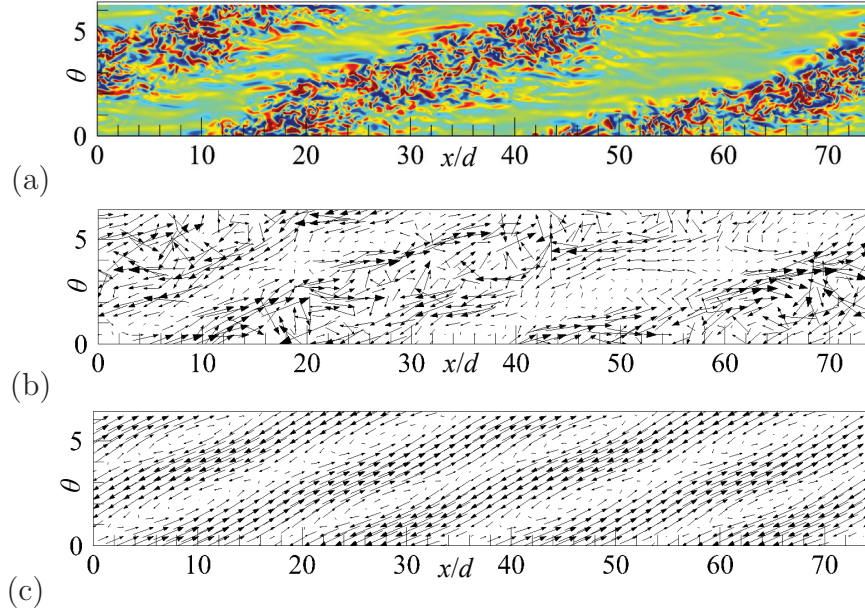


Fig. 3.29 Two-dimensional contours of instantaneous (a) wall-normal velocity fluctuation at the gap center, (b) r -averaged streamwise and azimuthal velocity fluctuations as a vector, and (c) r -averaged streamwise and azimuthal mode velocity of $(m_x, m_\theta) = (2, 1)$ as a vector for $\eta = 0.5$ at $\text{Re}_\tau = 56$. Color ranges (a) $(u'_r|_{\min}/u_\tau, u'_r|_{\max}/u_\tau) = (-1, 1)$.

obtaining the helical mode.

$$U_T(m_\theta) = \int \dot{u}_x(m_x, m_\theta) dm_x \quad (3.10)$$

$$W_T(m_\theta) = \int \dot{u}_\theta(m_x, m_\theta) dm_x \quad (3.11)$$

As shown in Fig. 3.30, a discontinuous peak of U_T and W_T is located at $m_\theta = 1$ corresponding to the helical mode. Similar distributions of U_T and W_t are observed for $\eta = 0.4$ and 0.8 as shown in Fig 3.31 By adopting these methods, the dominant modes for each structure are analyzed in the following subsections.

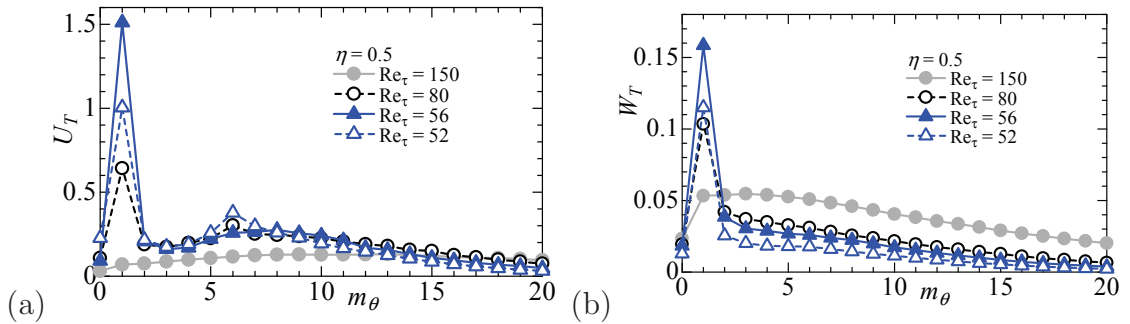


Fig. 3.30 Mean turbulent (a) streamwise and (b) azimuthal intensity of each mode $\dot{u}_x(m_x, m_\theta)$ averaged along m_x for $\eta = 0.5$.

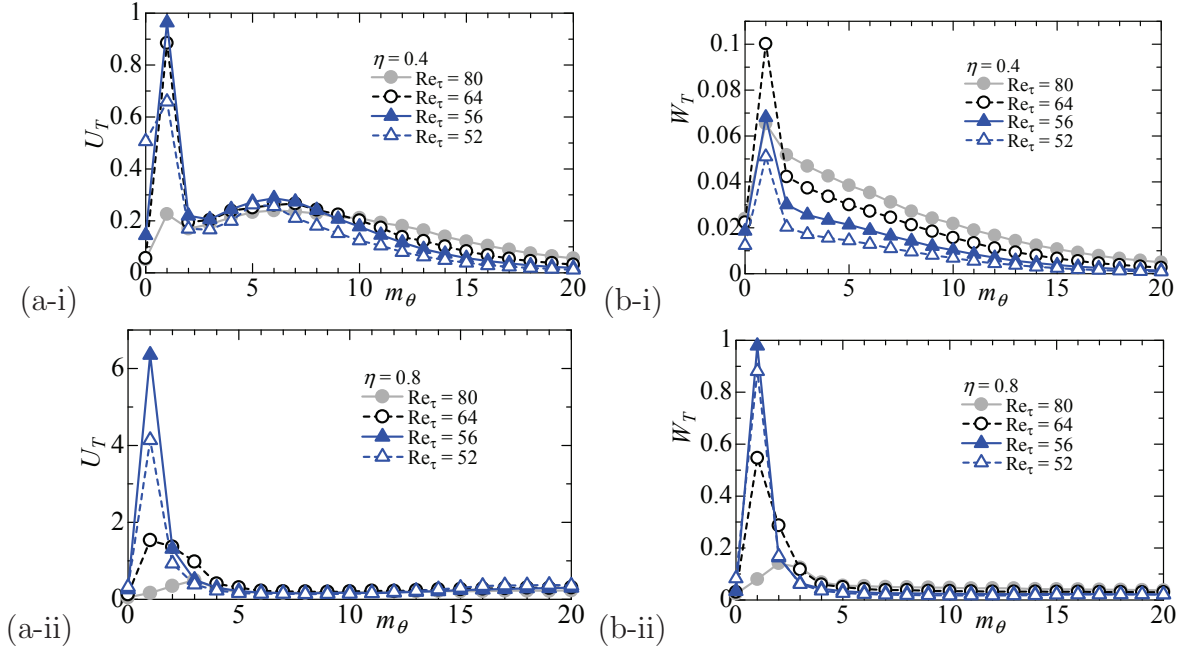


Fig. 3.31 Mean turbulent (a) streamwise and (b) azimuthal intensity of each mode $\hat{u}_x(m_x, m_\theta)$ averaged along m_x for $\eta =$ (i) 0.4, (ii) 0.8.

3.4.2 Dominant modes for $\eta = 0.1$

The same methods are used for all η . As for considering the puff mode, we investigate $\hat{u}_x(m_x, m_\theta)$ and $\hat{u}_\theta(m_x, m_\theta)$ in the m_x - m_θ plane for $\eta = 0.1$ (Fig. 3.32). Compared to $\eta = 0.5$, we cannot observe the peak at $m_\theta = 1$ but a clear peak is at $m_\theta = 0$ for \hat{u}_x especially at low Re_τ . Unlike the helical mode, \hat{u}_θ does not show any peaks and high \hat{u}_θ with a very broad base with respect to the azimuthal mode is observed.

Figure 3.33 presents (a) instantaneous wall-normal velocity fluctuations u'_r and wall-normal averaged streamwise velocity extracted at $(m_x, m_\theta) = (1, 0)$ at $Re_\tau = 48$. This extracted mode velocity can separate turbulent and laminar regions of a straight puff. Because a straight puff is a streamwise localized structure without any azimuthal secondary flow, this mode ($m_\theta = 0$) is determined as a straight puff to differentiate it from the helical mode.

As for quantitative value, $U_T(m_\theta)$ and $W_T(m_\theta)$ are also displayed in Fig. 3.34. At low $Re_\tau \leq 52$, the peak of U_T is at $m_\theta = 0$ showing the puff mode. However, at $Re_\tau = 56$, U_T of $m_\theta = 1$ and 2 are also dominant because the flow regime is turbulence with some laminar spot taking the form of a wispy oblique interface. As for W_T , there is clear peak at $m_\theta = 1$ similar to high η . However, compared to $\eta = 0.5$, this peak does not show a discontinuous value and smoothly decrease with increasing m_θ . Then, the meaning of the high W_T of $m_\theta = 1$ differs from the helical mode and this continuous distribution shows the difficulty of separating large- and small-scale flows.

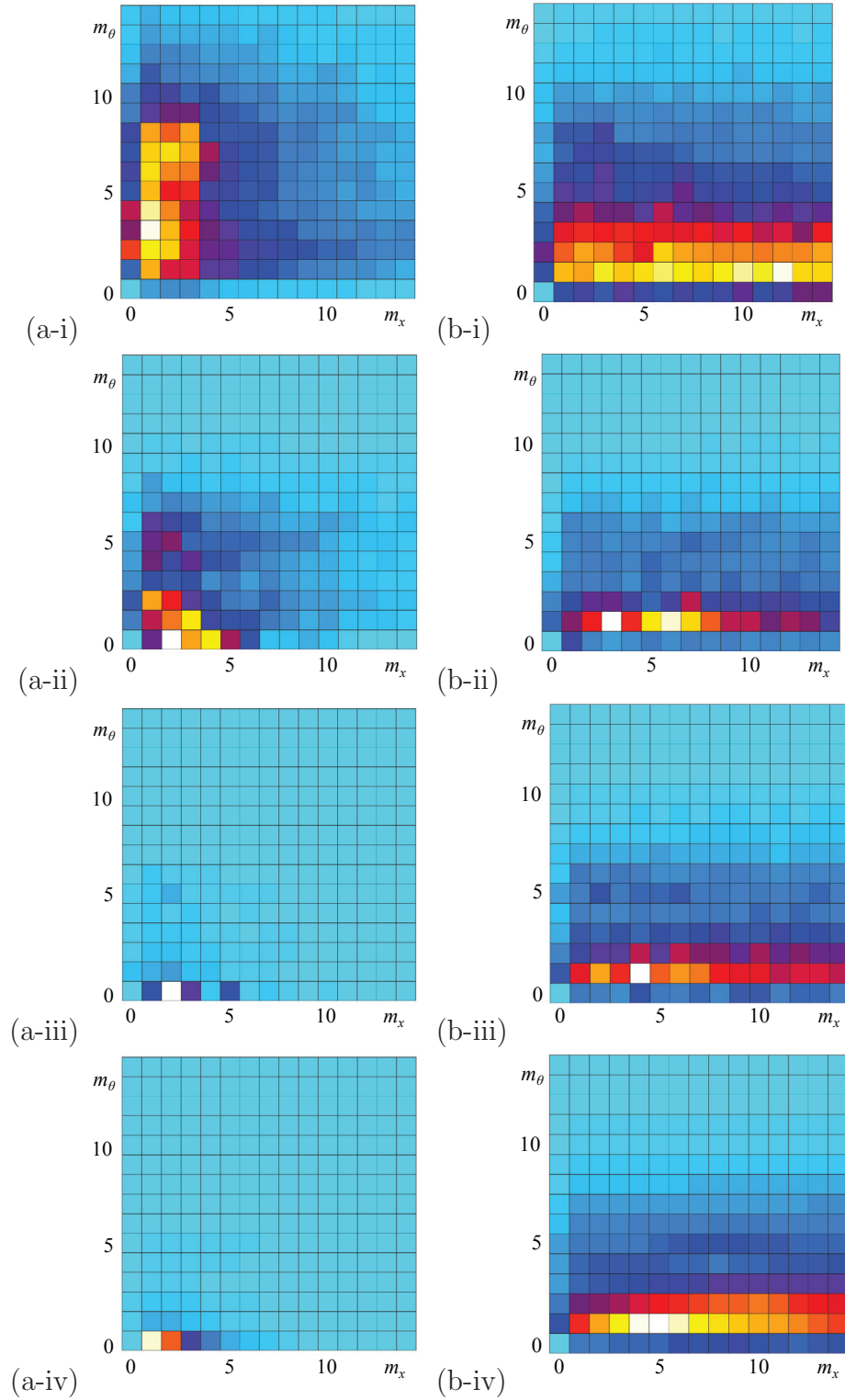


Fig. 3.32 Two-dimensional contours of mean (a) streamwisw and (b) azimuthal turbulent intensity of each mode for $\eta = 0.1$ at $Re_\tau =$ (i) 80, (ii) 56, (iii) 52, and (iv) 48. ($\hat{u}_i|_{max}/u_\tau$) are (a-i) (0.028), (b-i) (0.0017), (a-ii) (0.066), (b-ii) (0.001), (a-iii) (0.28), (b-iii) (0.00046), (a-iv) (0.14), and (b-iv) (0.00012).

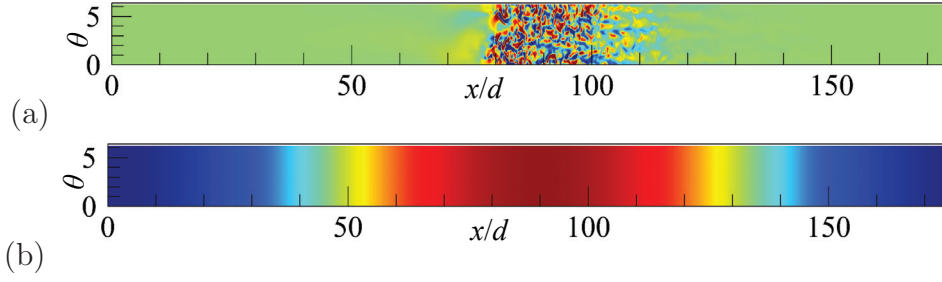


Fig. 3.33 Two-dimensional contours of instantaneous (a) wall-normal velocity fluctuation at the gap center, (b) r -averaged streamwise mode velocity of $(m_x, m_\theta) = (1, 0)$ for $\eta = 0.1$ at $Re_\tau = 48$. Color ranges (a) $(u'_r|_{min}/u_\tau, u'_r|_{max}/u_\tau) = (-1, 1)$ and (b) $(\hat{u}'_r|_{min}/u_\tau, \hat{u}'_r|_{max}/u_\tau) = (-0.0027, 0.0027)$.

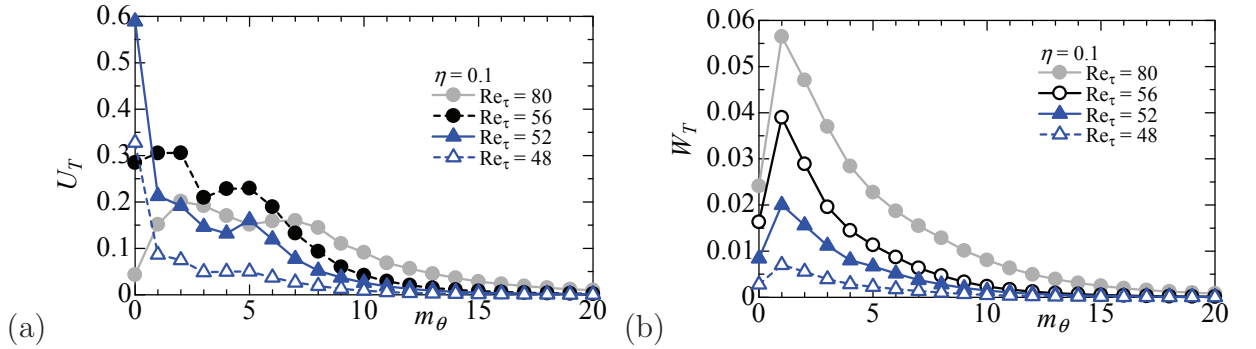


Fig. 3.34 Mean turbulent (a) streamwise and (b) azimuthal intensity of each mode $\hat{u}_x(m_x, m_\theta)$ averaged along m_x for $\eta = 0.1$.

3.4.3 Dominant modes for $\eta = 0.2$ and 0.3

As for intermediate radius ratios, $\hat{u}_x(m_x, m_\theta)$ and $\hat{u}_\theta(m_x, m_\theta)$ in the m_x - m_θ plane for $\eta = 0.2$ and 0.3 are shown in Figs. 3.35 and 3.36.

For $\eta = 0.2$ and 0.3 at high $Re_\tau = 80$, $\hat{u}_x(m_x, m_\theta)$ and $\hat{u}_\theta(m_x, m_\theta)$ are broadly distributed and no peak is observed. However, at $Re_\tau = 64$ for $\eta = 0.2$, the peak at $(m_x, m_\theta) = (3, 1)$ corresponding to the helical mode is observed although some intermediate values representing small scale structures are also distributed. A similar distribution is obtained at $Re_\tau = 56$ for $\eta = 0.3$. In contrast, a lower Re_τ of 52 for $\eta = 0.2$ and 0.3 where turbulence is sustained, the helical mode disappears but the puff mode of $(m_x, m_\theta) = (1, 0)$ appears. At the intermediate $Re_\tau = 56$ for $\eta = 0.2$, although the most dominant mode is at $(m_x, m_\theta) = (1, 0)$, there are high intensity region around $m_\theta = 1$ with small m_x . As for $\eta = 0.3$, a similar trend is observed at $Re_\tau = 54$ and the turbulent intensity of $(m_x, m_\theta) = (3, 1)$ is higher than that of $(1, 0)$. This change of dominant mode with Re_τ explains why the dominant structure of turbulence does not change only by η but also by Re_τ .

These two different dominant modes of $(m_x, m_\theta) = (3, 1)$ and $(1, 0)$ characterize helical and straight modes, respectively. Therefore, as for mode analysis, the helical puff is

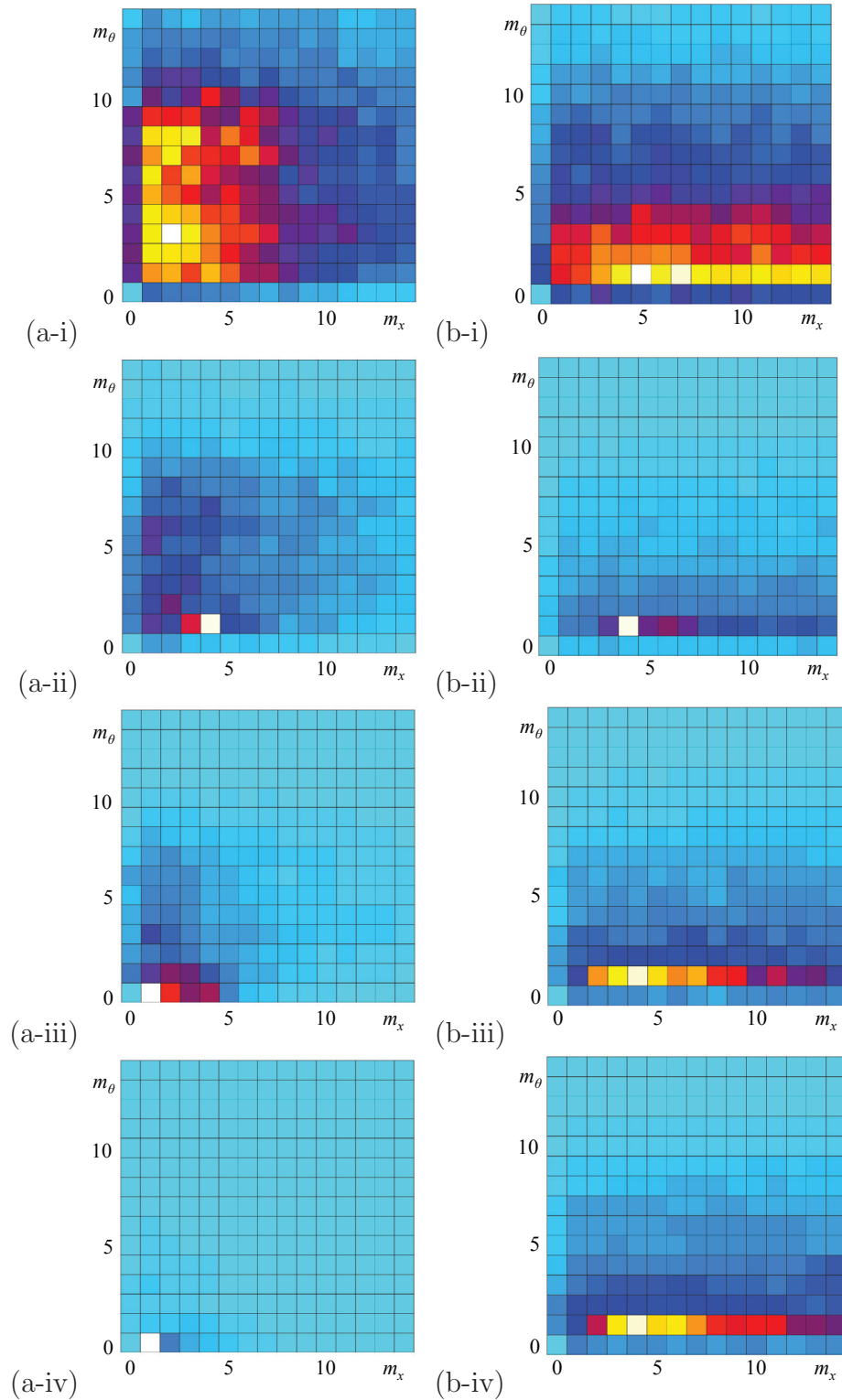


Fig. 3.35 Two-dimensional contours of mean (a) streamwise and (b) azimuthal turbulent intensity of each mode for $\eta = 0.2$ at $\text{Re}_\tau =$ (i) 80, (ii) 64, (iii) 56, and (iv) 52. $(\hat{u}_i|_{max}/u_\tau)$ are (a-i) (0.017), (b-i) (0.001), (a-ii) (0.064), (b-ii) (0.003), (a-iii) (0.13), (b-iii) (0.0014), (a-iv) (0.42), and (b-iv) (0.0005).

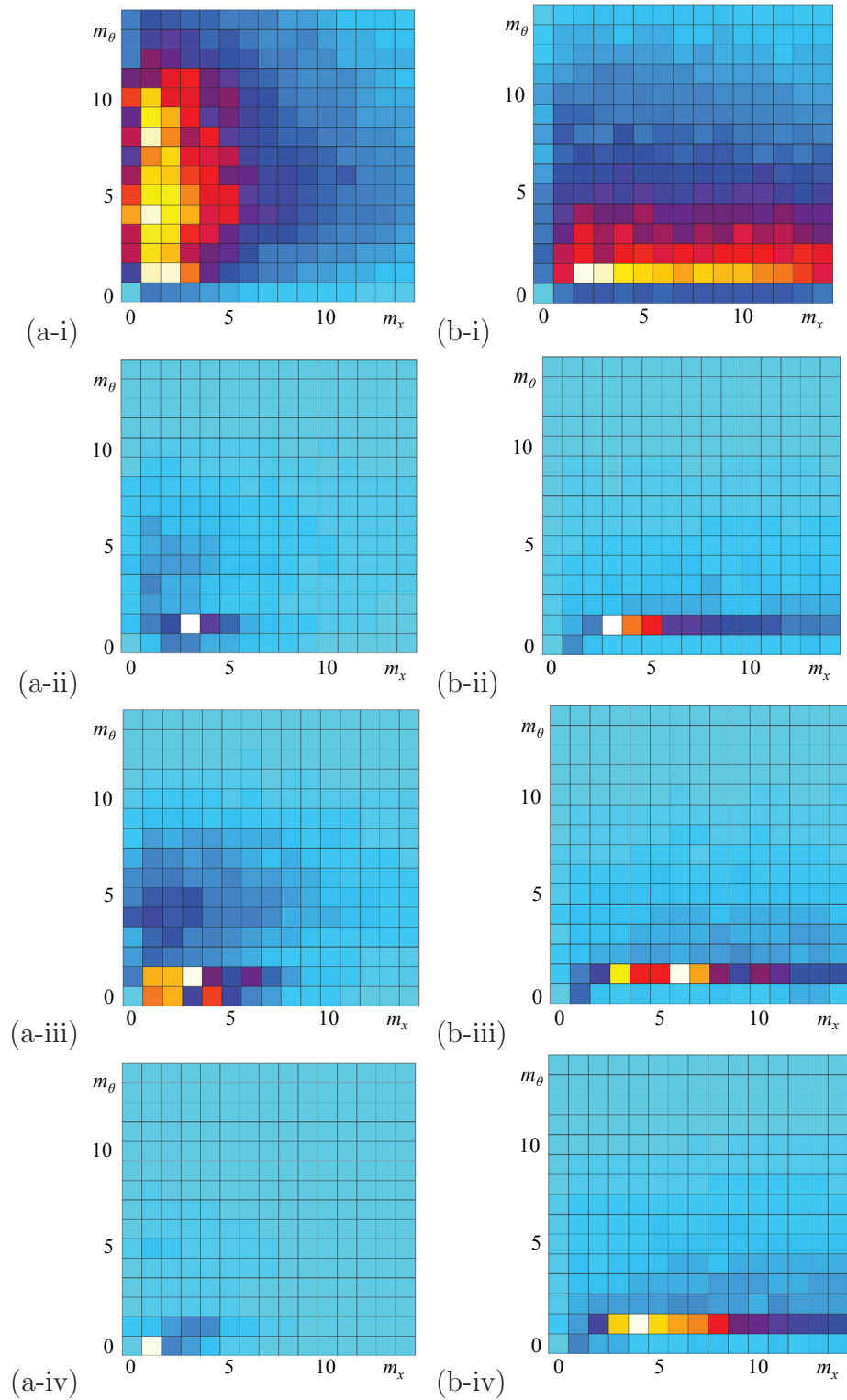


Fig. 3.36 Two-dimensional contours of mean (a) streamwise and (b) azimuthal turbulent intensity of each mode for $\eta = 0.3$ at $Re_\tau =$ (i) 80, (ii) 56, (iii) 54, and (iv) 52. ($\hat{u}_i|_{max}/u_\tau$) are (a-i) (0.03), (b-i) (0.0025), (a-ii) (0.15), (b-ii) (0.003), (a-iii) (0.1), (b-iii) (0.0023), (a-iv) (0.39), and (b-iv) (0.0014).

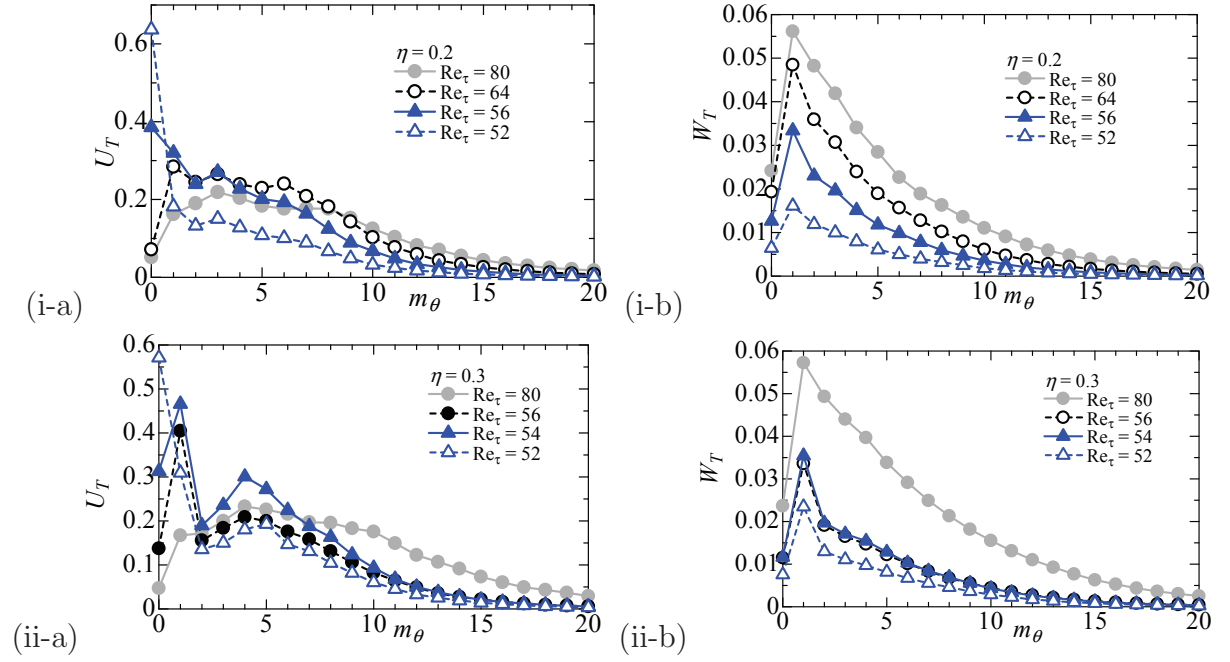


Fig. 3.37 Mean turbulent (a) streamwise and (b) azimuthal intensity of each mode $\hat{u}_x(m_x, m_\theta)$ averaged along m_x for (i) $\eta = 0.2$ and (ii) $\eta = 0.3$.

characterized by the equilibrium state of two different modes of $(m_x, m_\theta) = (1, 0)$ as the straight puff and of $(3, 1)$ as the helical mode. Then, we predict the equilibrium puff would be seen when the intensity at $(m_x, m_\theta) = (3, 1)$ and $(1, 0)$ is the same.

$U_T(m_\theta)$ and $W_T(m_\theta)$ for $\eta = 0.2$ and 0.3 are also shown in Fig. 3.37. As described above, the dominance of m_θ for U_T is changed with Re_τ . Although it is not very clear compared to high η , W_T displays discontinuous distribution at low Re_τ especially for $\eta = 0.3$.

3.4.4 Possession of dominant modes

Based on the mode analysis as noted above, the dominant mode of the straight puff and helix are obtained at $m_\theta = 0$ and 1 of U_T , respectively. Therefore, possessions of dominant mode is analyzed by the following equations.

$$\gamma_0 = \frac{U_T(0)}{U_T(0) + U_T(1)} \times 100 \quad (3.12)$$

$$\gamma_1 = \frac{U_T(1)}{U_T(0) + U_T(1)} \times 100 \quad (3.13)$$

γ_0 and γ_1 correspond to a percentage of the puff mode and helical mode. As shown in Fig. 3.37, γ_0 and γ_1 are clearly classified. However, this method cannot differentiate helical and turbulence (streaks) mode especially for low η and for high Re_τ . There is not discontinuous peak at $m_\theta = 1$ for the fully turbulent regime and a clear difference between turbulence and helical mode for low η is recognized since the helical and turbulence modes are at the

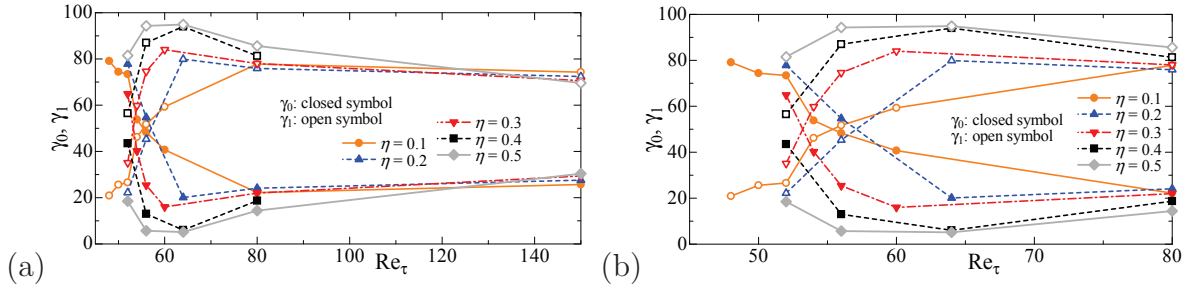


Fig. 3.38 Percentages based on mean turbulent intensity of $m_\theta = 0$ and 1. Extended figure of (a) around low Re_τ is shown in (b).

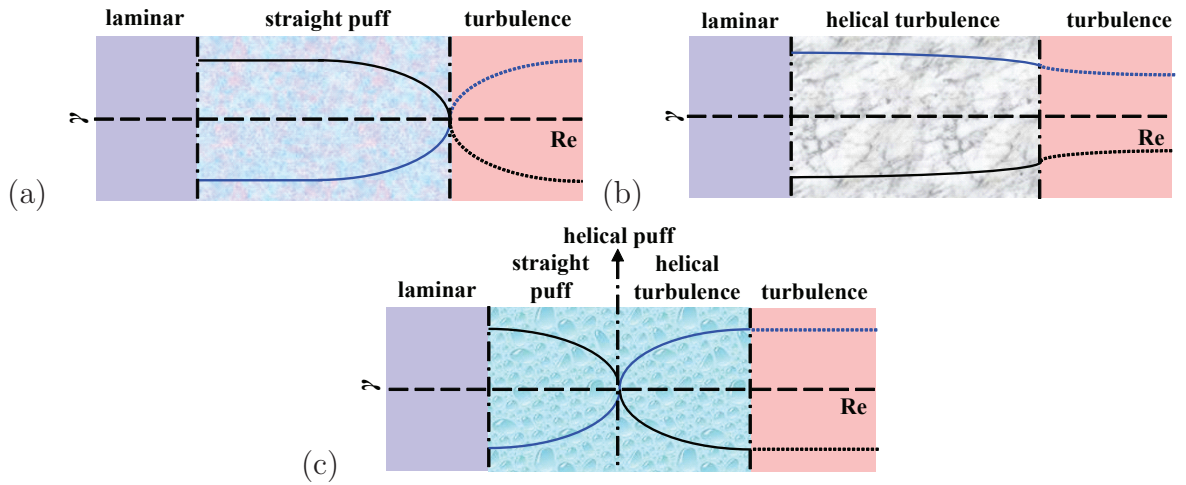


Fig. 3.39 Conceptual bifurcation diagram for three different regime of η (a) ≤ 0.1 , (b) ≥ 0.5 , and (c) $= 0.2$ and 0.3 . Black and blue lines correspond to γ_0 and γ_1 , respectively.

same m_θ . This is caused by the narrow azimuthal length (L_z) for small η and few streaks could only be in the azimuthal domain as shown in the previous section. Therefore, γ_1 is higher than γ_0 in the high Re_τ region. With decreasing Re_τ , γ_1 increases for high η . This reveals that fully-developed turbulence changes helical turbulence. To ignore the criterion of helical and fully-developed turbulence, we only consider the low Re_τ region as shown in Fig. 3.38(b). The dominance of γ_0 and γ_1 switches with decreasing Re_τ for $\eta = 0.2$ and 0.3 . This crossing point may indicate the occurrence of the equilibrium helical puff. In contrast, there is only one clear dominant peak of γ_1 for high $\eta = 0.5$. In addition, γ_0 for low $\eta = 0.1$ is dominant in the low Re_τ region. A conceptual bifurcation diagram for the three different regimes is shown in Fig 3.39.

At high Re_τ , γ_1 is dominant and the flow regime is fully-turbulent for $\eta \leq 0.1$ (Fig 3.39(a)). The dominance of γ_0 and γ_1 switches at the critical point with decreasing Re_τ and γ_0 as the puff mode increases. Below lower critical Re , the flow relaminarizes. For high $\eta \leq 0.4$, γ_1 is higher than γ_0 in all Re_τ ranges (Fig 3.39(b)). Helical turbulence occurs at the critical point although it is difficult to separate the helical and turbulence modes by this analysis. For intermediate $\eta = 0.2$ and 0.3 , the boundary between helical turbulence

and fully-turbulence is similar to that for $\eta = 0.8$ (Fig 3.39(c)). In addition, the switching point of γ_0 and γ_1 is the same as that for $\eta = 0.1$. Differing from the point for $\eta = 0.1$, the switching point for $\eta = 0.2$ and 0.3 delimits the puff and helical modes. Then, as discussed above, the crossing point for $\eta = 0.2$ and 0.3 may correspond to the occurrence of the equilibrium helical puff.

Because the classification of γ cannot separate the helical and turbulent modes, we consider another mode as fully-turbulence (streaks) for new separation. For this object, we consider three $U_T(m_\theta)$, which are $U_T(0)$ as puff, $U_T(1)$ as helical, and $\text{Max}(U_T(\text{w/o } 0 \text{ and } 1))$ as streak modes. Possessions of the dominant mode is analyzed by the following equations.

$$\Gamma_0 = \frac{U_T(0)}{U_T(0) + U_T(1) + \text{Max}(U_T(\text{w/o } 0 \text{ and } 1))} \times 100 \quad (3.14)$$

$$\Gamma_1 = \frac{U_T(1)}{U_T(0) + U_T(1) + \text{Max}(U_T(\text{w/o } 0 \text{ and } 1))} \times 100 \quad (3.15)$$

$$\Gamma_{\text{w/o } 0 \text{ and } 1} = \frac{\text{Max}(U_T(\text{w/o } 0 \text{ and } 1))}{U_T(0) + U_T(1) + \text{Max}(U_T(\text{w/o } 0 \text{ and } 1))} \times 100 \quad (3.16)$$

Compared to γ , Γ can classify helical and turbulence modes as shown in Fig 3.40. A conceptual bifurcation diagram for the three different regime is also shown in Fig 3.41.

Γ_0 shows low values and the crossing point of Γ_1 and $\Gamma_{\text{w/o } 0 \text{ and } 1}$ exists for $\eta = 0.5$. Therefore, this new analysis can separate the helical and turbulent mode differing from γ . As for $\eta = 0.1$, the distribution of Γ are similar to that of γ . The value of Γ_1 and $\Gamma_{\text{w/o } 0 \text{ and } 1}$ is almost same because the mode at $m_\theta = 1$ and 2 (as w/o 0 and 1) represents turbulence (streaks). For very low η , $m_\theta = 1$ represents turbulence not the helical mode since L_z is too narrow to sustain many streaks. For intermediate η of 0.2 and 0.3 , with increasing Re_τ , the dominant value changes from Γ_0 to $\Gamma_{\text{w/o } 0 \text{ and } 1}$ through Γ_1 . As discussed in γ , the crossing point of Γ_0 and Γ_1 indicates an equilibrium helical puff and $\Gamma_{\text{w/o } 0 \text{ and } 1}$ increases with increasing Re_τ . With increasing $\Gamma_{\text{w/o } 0 \text{ and } 1}$, the turbulent region expands and some laminar spots occur. Because a laminar spot has obliqueness, Γ_1 still has high value, but the laminar region disappear and only Γ_0 is dominant at high Re_τ .

3.5 Summary

Laminar turbulent coexistence corresponding to localized turbulent structures of the transitional aPf have been investigated. Robust and clear helical turbulence similar to the pPf have been identified for $\eta = 0.8$ and 0.5 . However, the laminar region expands with decreasing Re and helical turbulence is marginally modulated and collapsed at the lowest $\text{Re}_\tau = 52$ for $\eta = 0.5$. Therefore, even for such a high η , helical puffs emerged in a very narrow range of Reynolds number around Re_g .

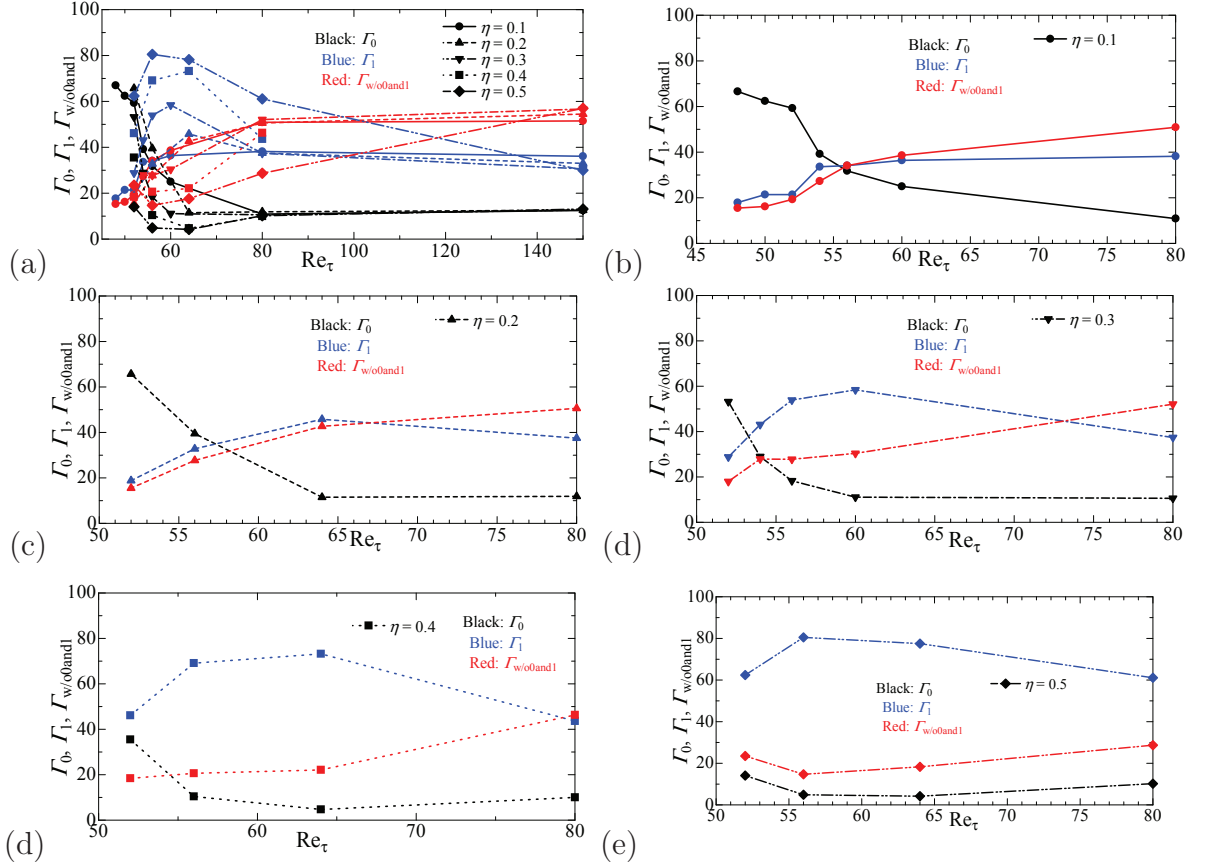


Fig. 3.40 Percentages of percentage based on mean turbulent intensity of $m_\theta = 0$ and 1, and on maximum mean turbulent intensity without $m_\theta = 0$ and 1. Figures (b–e) show percentages for each radius ratio separated from (a).

At a lower radius ratio, $\eta = 0.3$, sustained turbulence appears first in the form of helical stripe patterns with stronger fluctuations similar to higher $\eta = 0.5$ and 0.8. The pitch angle of such patterns decreases with decreasing η . For $\eta = 0.3$, at marginally low Re_τ , the flow relaminarizes partly and helical puff emerges. This indicates a possible change towards a new phenomenology as η will be further decreased. This complex transition process is also obtained for $\eta = 0.2$. However, compared to $\eta = 0.3$, helical turbulence has not been recognized for $\eta = 0.2$ even at high Re_τ . For these middle radius ratio of 0.2 and 0.3, the streamwise localized structure without obliqueness is also recognized at very low Re_τ and the ratio of the straight puff increases with decreasing η .

For smaller η (0.1 and probably also below), the large-scale flow becomes axisymmetric, and the turbulent fluctuations occur in finite-length turbulent patches similar to equilibrium puffs in the cPf. However, at high Re_τ for $\eta = 0.1$, when a laminar spot occurs in the turbulent regime or when the straight puff is first observed, misty oblique interfaces between the turbulent and laminar region are observed, although the azimuthal length is too narrow to maintain the azimuthal secondary flow. This similarity can be surprising, because the presence of the inner rod makes the geometry of the aPf quite different from that of the

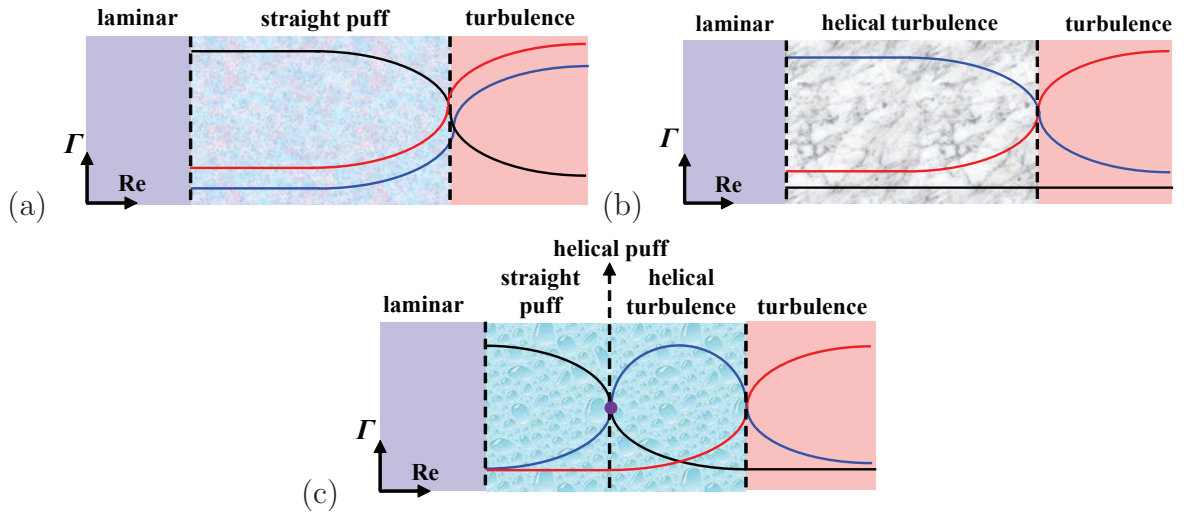


Fig. 3.41 Conceptual bifurcation diagram for three different regime of η (a) ≤ 0.1 , (b) ≥ 0.5 , and (c) $= 0.2$ and 0.3 . Black, blue, and red lines correspond to γ_0 , γ_1 , and $\gamma_{w/0}$, respectively

cPf: boundary layers are present near the inner rod. Moreover, the laminar base flows display few quantitative differences between the cases $\eta = 1$ and $\eta = 0.1$: the maximum streamwise velocity occurs respectively at $y/d = 0.5$ and 0.4 (and 0.2 for η as low as 10^{-5}). The geometry of the aPf hence definitely differs from that of the cPf but the transitional phenomenology is similar.

As discussed above, the results indicated that the transition process for the aPf depended both on Re_τ and η . To obtain the whole transitional scenario for the aPf which bridge the cPf and the pPf, two different and new analyses are performed. One is of the azimuthal length depending on radius ratio to reveal the occurrence of helical shapes caused by the azimuthal large-scale flow. The other is a modal analysis to classify the dominant mode corresponding to straight/helical puffs, helical turbulence, and fully-turbulence. The analysis of the PDF of azimuthal velocity can determine the difference between helical turbulence and helical/straight puff. In addition, modal analysis clearly classifies the transitional structures. Three dominant modes corresponding to straight puff, helical shape, and turbulence are determined and the whole transition process for the aPf is obtained. For high $\eta \geq 0.5$, the helical mode is always dominant in the transitional regime. In contrast, the puff mode is dominant for small $\eta = 0.1$. For intermediate η of 0.2 and 0.3 , with increasing Re_τ , the dominant mode changes from puff to turbulence through the helical mode. The crossing Reynolds number (Re_{ehp}) of the puff and helical modes is predicted by this new analysis. This reveals that the equilibrium helical puff is only observed at Re_{ehp} and there is competition between a straight puff and a helical puff at $Re < Re_{ehp}$ or a helical puff and helical turbulence $Re_{ehp} < Re$.

The occurrence of the transition structures considerably influence the friction factor C_f and turbulent fraction F_t . When the flow regime corresponds to helical turbulence, the

friction factor and turbulent fraction maintain a high value that is similar to that for a fully turbulent regime. However, the friction factor immediately decreases, once the transitional structure is localized in the streamwise direction and formed the helical/straight puff. For low $\eta \leq 0.1$, only the straight puff is organized independently of Re_τ , and C_f decreases towards the laminar solution monotonically. In contrast with this monotonic trend, an overlapping region exists around Re_g for intermediate $\eta = 0.2$ and 0.3 . These non-monotonic trends of C_f and F_t must be caused by the alternations of transitional structures. As mentioned above, the shape of the transitional structure depends not only on η but also on Re_τ . For $\eta = 0.3$, helical turbulence is sustained only in a small range of high Re_τ , where the intermittent regime occurs. With decreases in Re_τ , the helical turbulence changes into the straight puff through the helical puff. Attributed to these alternations of transitional structures for a fixed intermediate η , both C_f and F_t follow two different paths of the helical turbulence and the straight puff.

The turbulence statistics in the aPf corresponds to asymmetric distributions with respect to the gap center. With respect to the streamwise mean velocity $\overline{u_x}$ profile, the asymmetry is strong when Re_τ is high and η was small. Even for low values of η ($\eta = 0.1$), the distributions become symmetric, once the transition from featureless to intermittent turbulence occurs. The transitional structure for low η is a puff (similar to that in the cPf but different from the oblique pattern in the pPf). Hence, in the subcritical regime, it is interesting to note that $\overline{u_x}$ exhibits dissimilarity with the cPf, although the flow structure is analogous for both flows. In contrast, the distributions and magnitude of turbulent intensities exhibit complex behaviors. The turbulent intensities display strong peaks near the inner cylinder with decreases in Re_τ , whereas the peak near the outer cylinder is higher at high Re_τ . This is due to the difference in the local friction velocity between the outer and inner cylinder, which becomes significantly large after a shift from featureless turbulence to the transitional regime. With respect to the transitional regime, the turbulent intensities were enhanced, in particular, when the helical turbulence occurred. The third peak appeared around the gap center, when the straight puffs existed, among which large laminar regions emerged.

4

Investigations of roughness effect on laminar-turbulent pattern

4.1 Quasi-linear stability analysis

A necessary condition for laminar-turbulent coexistence is the stability of the laminar regime to infinitesimal disturbances, which is an established mathematical property of smooth pCf (Romanov, 1973). The issue of the robustness of laminar-turbulent patterns to wall roughness must hence start with the following question: can roughness elements render the (modified) laminar flow regime linearly unstable? We first note that the purely laminar solution is valid only for smooth walls (i.e. $\alpha d = 0$ or $hd = 0$), while in the presence of finite roughness the new laminar solution mimics a linear function of y only sufficiently away from the roughness elements. This can be seen in Fig. 4.1 for simulations performed at relatively low $Re_w = 700$. The α - and h -dependence of the laminar solution renders modal linear stability analysis of the laminar solution, usually based on modified Orr-Sommerfeld equations (Floryan, 2007), relatively tedious. Besides modal linear stability analysis is often poorly adapted to shear flows because of the non-normal nature of the linearized operator. Non-modal stability approach (Schmid and Henningson, 2001; Floryan, 2006) is then traditionally used to investigate the receptivity properties of the flow to finite-amplitude disturbances. We circumvent all these elegant tools in favor of a more pragmatic approach based on a small set of fully nonlinear computations: the laminar flow is first simulated at low enough Re_w (in the presence of non-vanishing roughness), and it is later used as an initial condition for a new nonlinear simulation for different parameters, both in the absence and in the presence of computationally added finite-amplitude disturbances. The parameters tested are $(Re_w, h/d) = (700, 0.125)$ for one rough wall and $(1100, 0.25)$ for two rough walls, while several different finite values of the roughness density parameter αd have been tested from 0.25 to 2, without any clear influence on the stability results. The other parameters for the simulations are $L_x \times L_z = 17d \times 8.5d$, and $N_x \times N_y \times N_z = 2^7 \times 96 \times 2^6$. The various initial perturbations considered here are a) no disturbance,

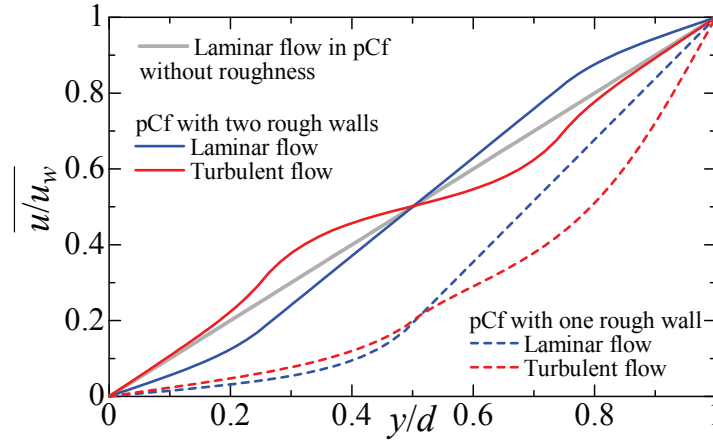


Fig. 4.1 Streamwise mean velocity for laminar and turbulent flows of the pCf with one/two rough walls for rectangular profiles at $Re_w = 700$, $h/d = 0.125$, and $\alpha d = 0.5$.

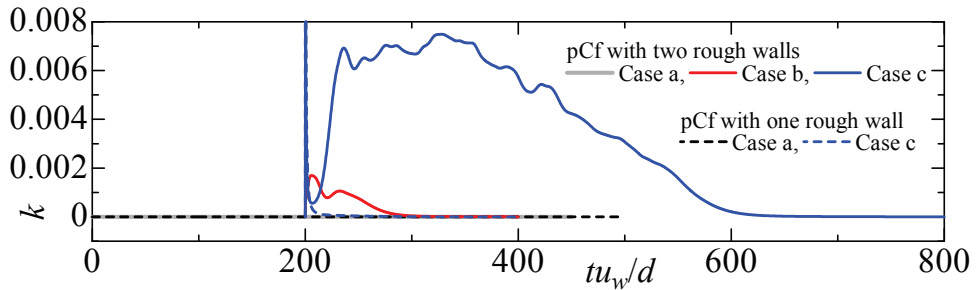


Fig. 4.2 Time evolution of turbulent energy $k(t)$ with or without disturbance in the pCf with one/two rough walls for rectangular profiles with $\alpha d = 0.5$. The Reynolds number and roughness height for one- and two-rough wall cases are $(Re_w, h/d) = (700, 0.125)$ and $(1100, 0.25)$, respectively. See text for details on cases a , b and c .

b) a vortex pair similar to that used in (Lundbladh and Johansson, 1991; Duguet et al., 2009), and c) delocalized finite-amplitude noise (the disturbances in cases b and c were added after a time of $200d/u_w$). The arbitrariness in choosing these disturbances ensures that for each set of parameters, a return to the laminar flow (not followed by any departure again) implies its linear stability. This is indeed the case here for all parameters tested, as can be seen in Fig. 4.2, where the kinetic energy $k(t) = (u_x'^2 + u_y'^2 + u_z'^2)/2$ is monitored versus time (prime denotes here root-mean-square deviation with respect to the spatial xz -average) despite case b for the pCf with one rough wall. The laminar flow remains hence linearly stable a priori for most roughness cases, making laminar-turbulent coexistence and patterning possible. The rest of the paper is devoted to numerical evidence (or not) of such regimes depending on the parameters Re_w and h/d , with αd fixed to 1.0. Note that in the literature, the notion of ‘hydraulically active roughness’ can have several meanings. The usually accepted meaning is that roughness is ‘active’ (or ‘fully rough’) if the mean flow does not depend on viscosity (i.e., on the Reynolds number) any longer (Schlichting, 1968).

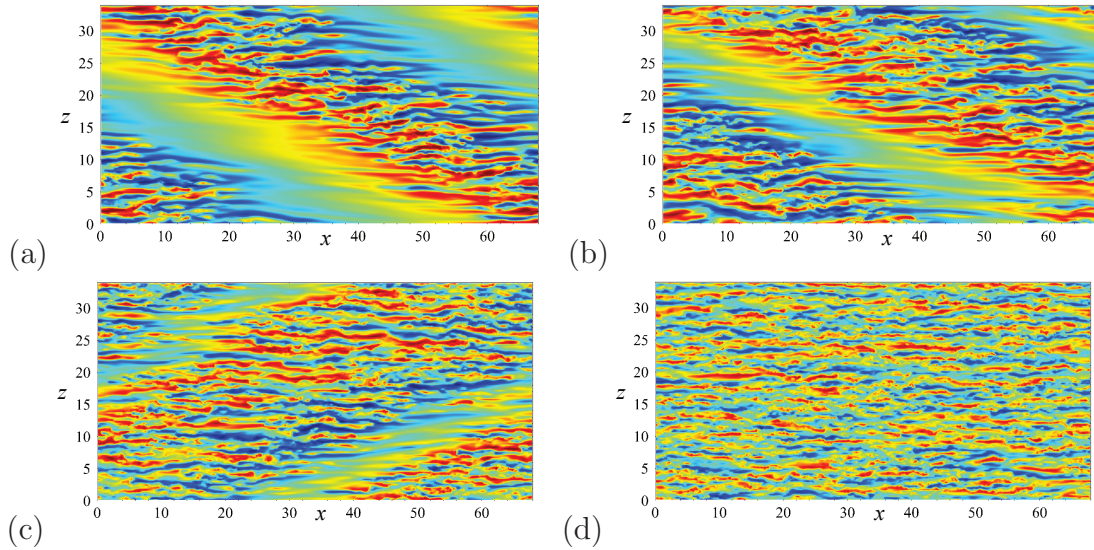


Fig. 4.3 Two dimensional contours of u'_x in x (horizontal: L_x)- z (vertical: L_z) plane at mid-gap (the channel center of $y = 0.5d$) in the pCf with smooth walls at $Re_w =$ (a) 2000, (b) 1600, (c) 1400, and (d) 1300. Contours range from blue to red are from -0.25 to 0.25 .

Floryan (2007) instead defines it by the property that the (rough) laminar flow is linearly unstable. Our stability assessments suggest that the present roughness in the pCf does not qualify as active in the stability sense, whereas the rest of the paper will confirm that the considered roughness can actually not be qualified as active in any of the meanings above.

4.2 Plane Couette flow with two smooth walls

Before addressing the effect of finite roughness on the system, it is useful to address the reference case of the pCf with smooth walls, using exactly the same computation domain with the same numerical resolution. In this case the only free parameter is the Reynolds number Re_w . The computational strategy used in both smooth and rough cases is similar to the ‘adiabatic decrease’ considered in Philip and Manneville(2010): a turbulent flow is realized at a sufficient high Re_w , and then Re_w is discrete in discrete steps (of about 100 in Re_w) until statistical equilibrium is reached (judging from temporal fluctuations of the spatial averages). Re_w is decreased until full relaminarization occurs. The adiabatic procedure ensures that the smallest value of Re_w for which turbulence is found sustained, approximates the onset Re_g of turbulence in the present finite-size system. Note that in principle Re_g is expected to depend on the roughness parameters. The list of parameters used both for the smooth and rough cases can be found in Tab. 2.6.

For the smooth case, the computations were initiated at $Re_w = 2000$, where the turbulent flow features mainly elongated streamwise streaks and no laminar part. Results of the adiabatic decrease in the smooth case are reported in Fig. 4.3 using two-dimensional contours of the streamwise velocity fluctuations at mid-gap. From $Re_w = 1600$ down to

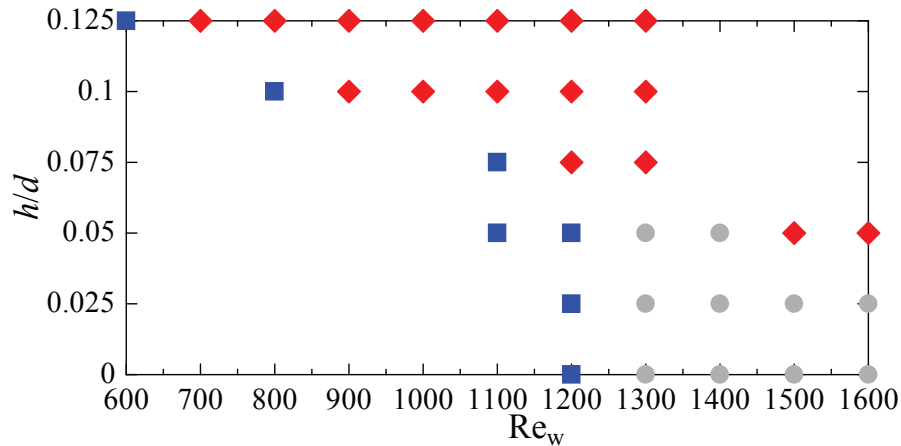


Fig. 4.4 Flow regimes of the pCf with two rough walls and rectangular-shaped roughness : patternless turbulence (red/diamonds); laminar (blue/squares); laminar-turbulent stripes (gray/circles).

1300, an oblique large-scale turbulent stripe emerges while quasi-laminar zones appear. The area occupied by turbulence monotonously drops from 100% down to a finite value at $Re_w = 1300$. The flow relaminarizes between $Re_w = 1300$ and 1200, suggesting the approximate value of $Re_g \approx 1300$, in good agreement with larger-size experiments and simulations (Prigent, 2001; Duguet et al., 2010).

4.3 Plane Couette flow with two rough walls

We now consider the case of two rough walls modelled using the Busse-Sandham approach. We focus more extensively on the case with rectangular-shaped roughness elements. The roughness density parameter αd is fixed to unity, so that the parametric study reduces to two parameters: the Reynolds number Re_w and the roughness height h/d varied here from 0 (smooth wall) to 0.25 (strong roughness). The computational strategy is again the adiabatic decrease procedure described in the preceding subsection.

4.3.1 Rectangular-shaped roughness elements

A bifurcation diagram for the different flow regimes is shown in Fig. 4.4. It reveals that a) the apparent value of Re_g decreases monotonically with increasing h/d , at least for $h/d > 0.05$; b) stripe patterns are robust for $h/d = 0.025$ in the range $Re_w \in [1300 : 1600]$, as well as for $h/d = 0.05$ for $[1300 : 1400]$, and they are no longer encountered for $h/d \geq 0.075$. This leads to the immediate interesting (perhaps expected) conclusion that laminar-turbulent patterns are indeed robust to the presence of roughness elements (at least with $\alpha d = 1$), except for too large values of the roughness height. In order to appreciate how stripe patterns get destroyed by high enough roughness elements, we fix

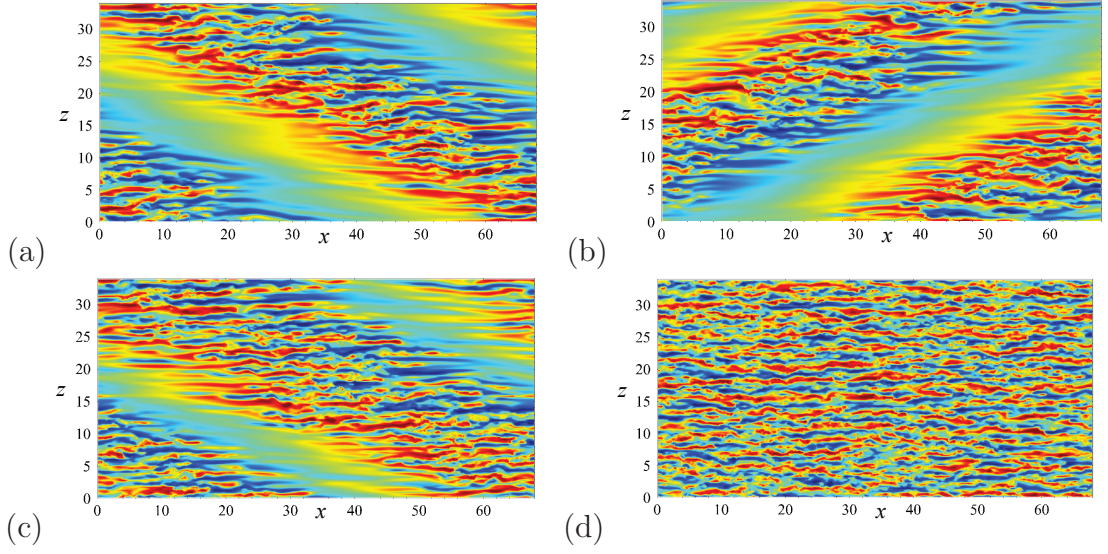


Fig. 4.5 Two dimensional contours for u'_x in x (horizontal: L_x/d)- z (vertical: L_z/d) plane at channel center in the pCf with two rough walls and a rectangular-shaped roughness profile for $Re_w = 1300$ and for $h/d =$ (a) 0, (b) 0.025, (c) 0.05 and (d) 0.075. Contours range from -0.25 (blue) to 0.25 (red).

Re_w to 1300 (where stripe patterns can be found even with smooth walls), and increase h/d in discrete steps of 0.025. Two-dimensional contours of instantaneous streamwise velocity u'_x are displayed at mid-gap in Fig. 4.5. Increasing h/d leads to the slight widening of the turbulent stripe in the streamwise direction, making higher h/d cases resemble visually the smooth simulations at higher Re_w . The flow appears patternless for all $h/d \geq 0.075$. The mean streamwise velocity profiles are shown in Fig. 4.6 (a) for $Re_w=1300$ and varying h/d , along with its y -derivative in Fig. 4.6 (b). The sharpness of the rectangular-shaped function F is reflected in the gradients of the mean velocity profile as a singularity, except for the patternless turbulent cases at high h/d . This suggests the possibility for inflectional instabilities providing continuous disturbances into the flow.

The friction factor is classically defined as $C_f = 2\tau_t/(\rho u_m^2)$, where τ_t is the total mean shear stress needed to drive the walls at the desired velocities. The normalization involves the bulk mean velocity $u_m = \frac{1}{d} \int_{y=0}^d \bar{u}_x dy$, where the over line denotes the temporal and spatial average at the walls. Since our model has flat walls and considers the effect of roughness indirectly through the roughness term $-\alpha|u_i|u_i F(y, h)$, τ_t differs from the usual wall shear stress $\tau_w = 1/2(\mu \partial \bar{u} / \partial y|_{y=0} + \mu \partial \bar{u} / \partial y|_{y=d})$ (where $\mu = \rho \nu$ is the dynamic viscosity). However the presence of the roughness term with $F \neq 0$ for $y < \eta$ makes the computational value of $\partial \bar{u} / \partial y$ at the walls not directly relevant for the estimation of the total drag τ_t .

To circumvent this issue we apply the conservation of mean streamwise momentum across

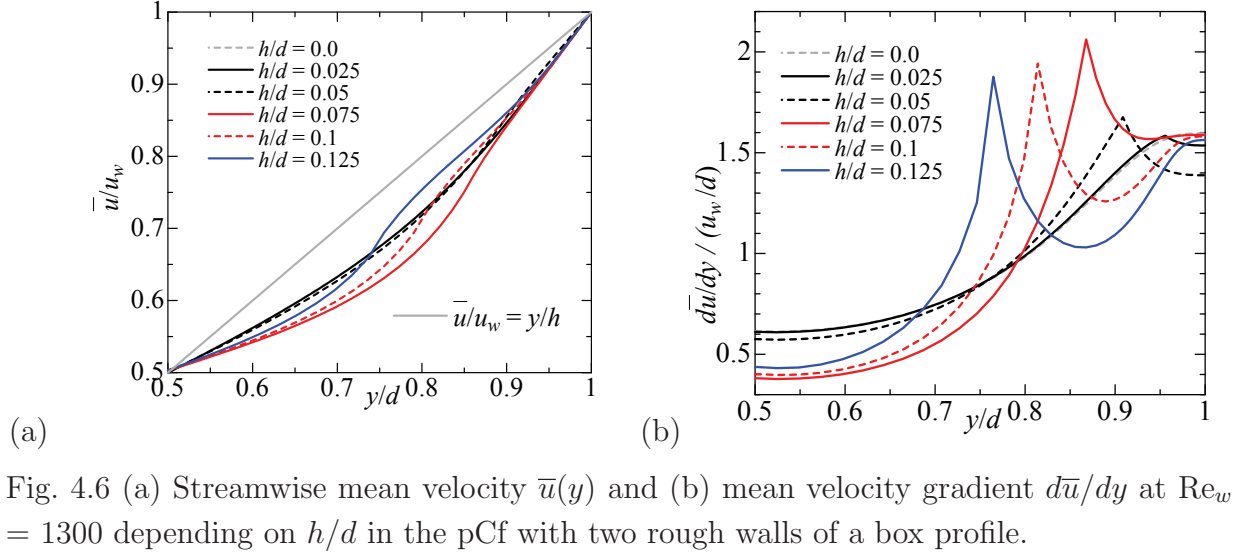


Fig. 4.6 (a) Streamwise mean velocity $\bar{u}(y)$ and (b) mean velocity gradient \bar{du}/dy at $Re_w = 1300$ depending on h/d in the pCf with two rough walls of a box profile.

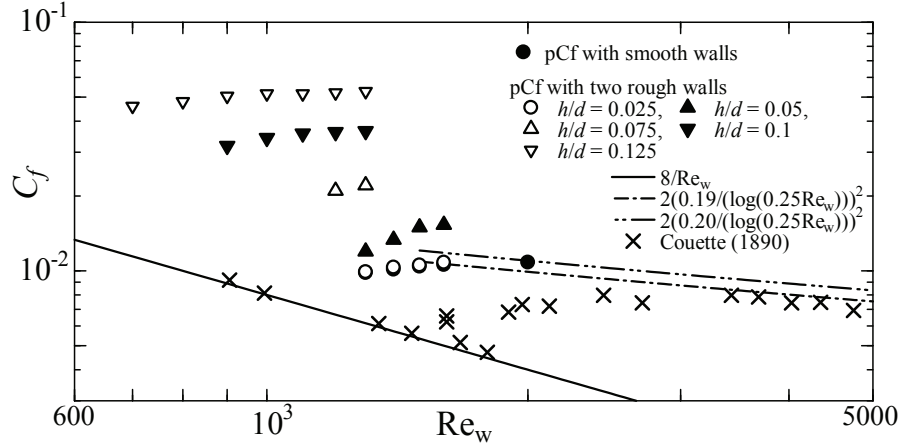


Fig. 4.7 Friction factor of two-rough-walls pCf with rectangular-shaped roughness elements.

a zero-pressure gradient channel (Pope, 2000) to the full model:

$$\frac{d}{dy} \left(\overline{u'_x u'_y}(y) - \nu \frac{\partial \bar{u}_x}{\partial y}(y) \right) + \alpha \overline{|u_x| u_x F_x}(y) = 0. \quad (4.1)$$

This expression allows one to evaluate τ_w directly from the knowledge of the flow field for any $y > \eta(h)$ (where $F(y)$ can be neglected), via:

$$\tau_w := \mu \frac{\partial \bar{u}_x}{\partial y} - \rho \overline{u'_x u'_y} - \rho \alpha \int_0^{\eta(h)} \overline{|u_x| u_x F_x} dy', \quad y \geq \eta(h). \quad (4.2)$$

The total mean shear stress τ_t contains both the usual mean shear stress at the flat wall and the contribution of the roughness term, such as $\tau_t = \tau_w + \rho \alpha \int_0^{\eta(h)} \overline{|u_x| u_x F_x} dy$ for $y \geq \eta(h)$, thus

$$\tau_t = \mu \frac{\partial \bar{u}_x}{\partial y} - \rho \overline{u'_x u'_y}, \quad y \geq \eta(h), \quad (4.3)$$

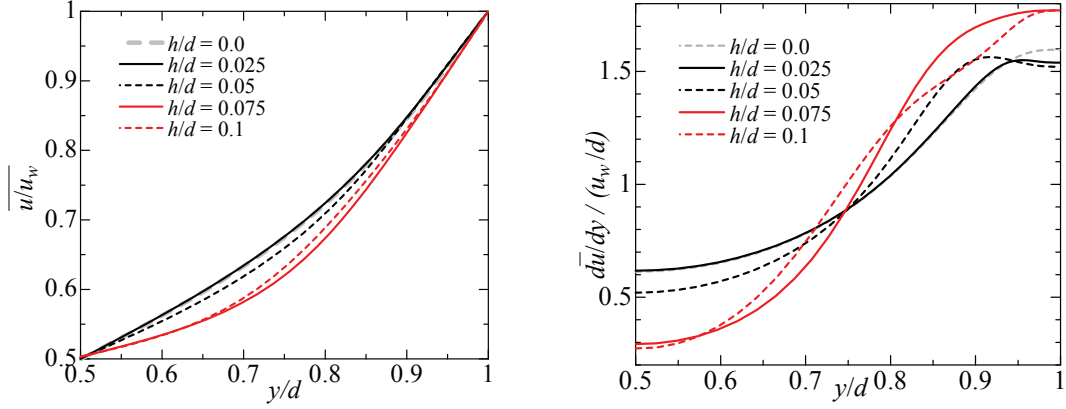


Fig. 4.8 Streamwise mean velocity (left) and mean velocity gradient (right) at $Re_w = 1300$ for varying h/d in the pCf with two rough walls. Gaussian roughness profile.

which is the usual expression for an arbitrary wall geometry in the absence of roughness modelling. In the present case, τ_t and thus C_f are evaluated at mid-gap. It was carefully verified that $\overline{u'_x u'_y} - \nu \partial_y \overline{u_x}$ is a conserved quantity for each value of h/d away from the walls, i.e. for $\eta(h) \leq y/d \leq 1 - \eta(h)$; however, this constant value depends strongly on h/d . The resulting equivalent Moody diagram, expressing the friction factor as a function of the wall Reynolds number Re_w , is shown in Fig. 4.7, in comparison with the usual laminar and turbulent asymptotes for smooth pCf. The signature of the higher roughness cases is the high drag found in the range $700 \leq Re_w \leq 1600$. It is striking that $C_f(Re_w)$ displays an overshoot in this transitional range, with the overshoot appearing more pronounced with stronger h/d . Such effects have been also frequently reported for cylindrical Poiseuille flows.

4.3.2 Gaussian-shaped roughness elements

The previous analysis is repeated for the case of another roughness distribution $F(y)$, considered now as a Gaussian-shaped profile of width $\eta(h)$. Note that this case is numerically less steep than the rectangular-shaped roughness case since the profile of $F(y)$ is smoother.

The parametric study was restrained here to the parameter values $\alpha d = 1$ and $Re_w = 1300$, leaving the roughness height h/d as the only free parameter. The mean streamwise velocity profiles and streamwise velocity gradients are shown in Fig. 4.8 (respectively left and right), while instantaneous mid-gap contours of u'_x are displayed in Fig. 4.9 for increasing h/d . The mean velocity gradients display now smoother and more realistic profiles, as shown in Fig. 4.8. The sequence of flow fields visualized in Fig. 4.9 is qualitatively similar to the rectangular-shaped case: the oblique stripe patterns adapt to the increasing roughness

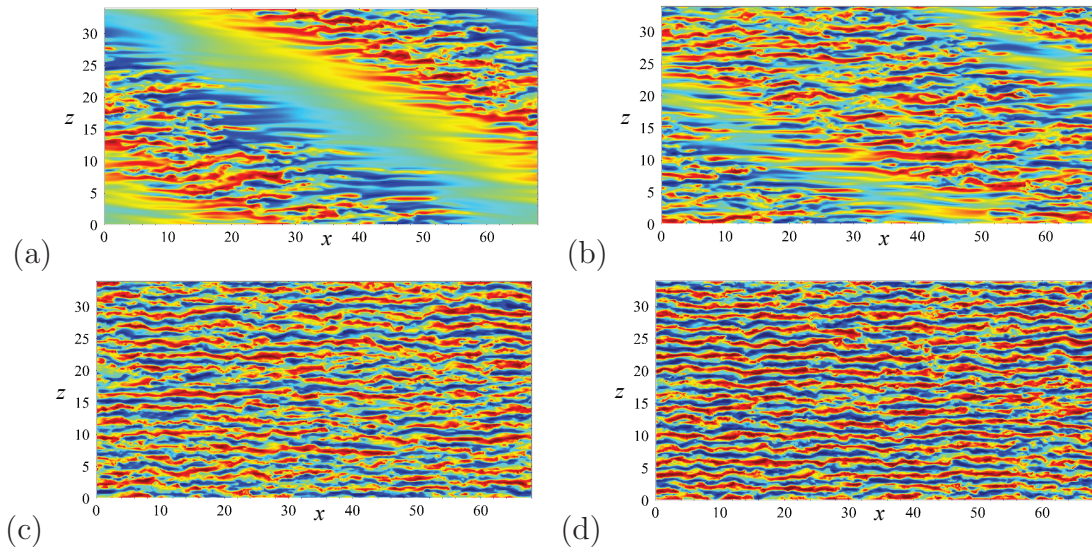


Fig. 4.9 Two-dimensional contours of u'_x at mid-gap in the pCf with two rough walls and a Gaussian-shaped roughness profile for $Re_w = 1300$ and $h/d =$ (a) 0.025, (b) 0.05, (c) 0.075, and (d) 0.1. Contours range from -0.25 (blue) to 0.25 (red).

by widening their turbulent part until it fills the whole domain. Note that the turbulent region for $h/d=0.05$ appears, for the same parameters, wider than in the rectangular-shaped case. Besides, in analogy with the results in (Busse and Sandham, 2012) obtained for six different roughness distributions at higher Re_w , it is tempting to speculate that the current phenomenology does not strongly depend, for fixed αd , on the exact shape of F .

4.4 Plane Couette flow with one rough wall

We focus now on the situation where only one of the two walls is rough, the other being smooth. By convention the rough wall is located at $y/d = 0$ whereas the smooth wall is at $y/d = 1$. There are several reasons for considering this case: firstly the set-up is asymmetric, which is an opportunity to test a more difficult case. Secondly, we believe that one-rough wall geometries lend themselves better to experimental verification in the case of the pCf. The reason is that most the pCf experiments so far (with the exception of Aydin and Leutheusser (1991)) relied on the use of endless elastic belts, either one belt or two depending on whether mean advection is introduced or not. In either case, engineering roughness elements on an elastic belt is technologically difficult. Considering a smooth belt while the other wall is static with roughness, seems a more promising set-up in practice. The present section is devoted to the analysis of this case using the Busse-Sandham model. As in this section, a parametric and energetic study is shown for the case of rectangular-shaped elements, and it is verified within a reduced parameter range that the results also hold for Gaussian roughness elements.

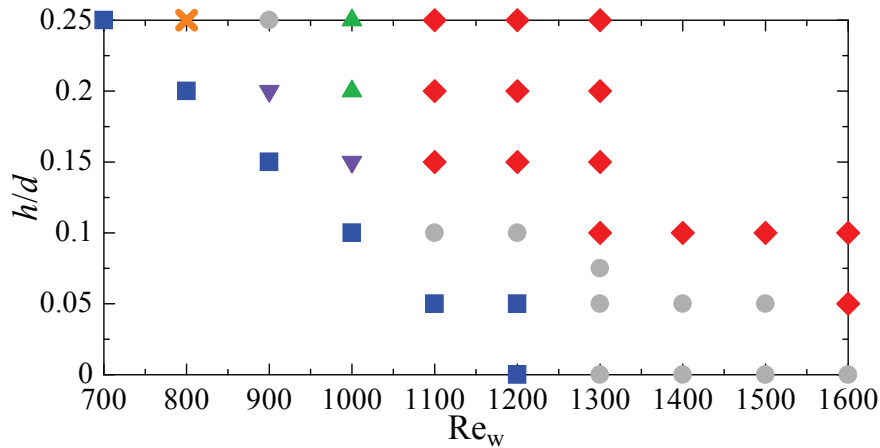


Fig. 4.10 Flow regimes of the pCf with one rough wall and rectangular-shaped roughness : patternless turbulence (red diamond); laminar flow (blue square); oblique stripe pattern (gray circle); laminar spot in turbulent environment (green triangle); turbulent spot in laminar environment (purple inverted triangle); staggered vortex pattern (orange cross).

4.4.1 Rectangular-shaped roughness elements

The parametric study with one rough wall, and rectangular-shaped roughness elements, has again been conducted with $\alpha d = 1$ and with two free parameters Re_w and h/d , following the same adiabatic decrease procedure. The zoology of regimes encountered is listed in Fig. 4.10. For relatively small roughness heights ($h/d \leq 0.05$ and to some extent ≤ 0.1), the situation is unchanged compared to the smooth case. This is also verified in Fig. 4.11 by visualizing the flow patterns at fixed $Re_w=1300$ for increasing h/d : the plot is similar to Fig. 4.5 for two rough walls in that the width of the turbulent zone increases with increasing h/d . Note that in contrast with Fig. 4.5, the current asymmetry does not allow to make meaningful comparisons at the exact mid-gap value of $y = 0.5$. Instead the velocity contours are plotted at the 'apparent' mid-gap value defined by the minimum of $\bar{u}_x(y)$ in the non-rough region $y \geq \eta(h)$. For $h/d = 0.1$, Fig. 4.10 alone suggests that the range of existence of the oblique laminar turbulent pattern shifts down to lower values of $\approx [1100 : 1300]$. In particular, the stripe pattern is maintained for $Re_w=1100$ and 1200 , whereas the pCf relaminarizes both in the smooth case and the two-roughness case. One-wall roughness seems hence able to shift down Re_g , whereas Re_g was reported as insensitive to h/d for two rough walls. This trend actually continues for increasing values of h/d : Re_g is approximatively 900 for $h/d = 0.2$ and 800 for $h/d = 0.25$.

New interesting regimes departing from the results of the previous section emerge however for $h/d \geq 0.15$ inside the range $Re_w \in [Re_g(h):1000]$. These regimes do neither correspond to standard oblique laminar-turbulent stripe patterns nor to anything ever reported in the pCf. We will describe each of them, keeping in mind that they are outputs from a specific model and thus require experimental validation. Surprisingly, we will see that the appearance of those new exotic flow regimes, even within the frame of the current roughness

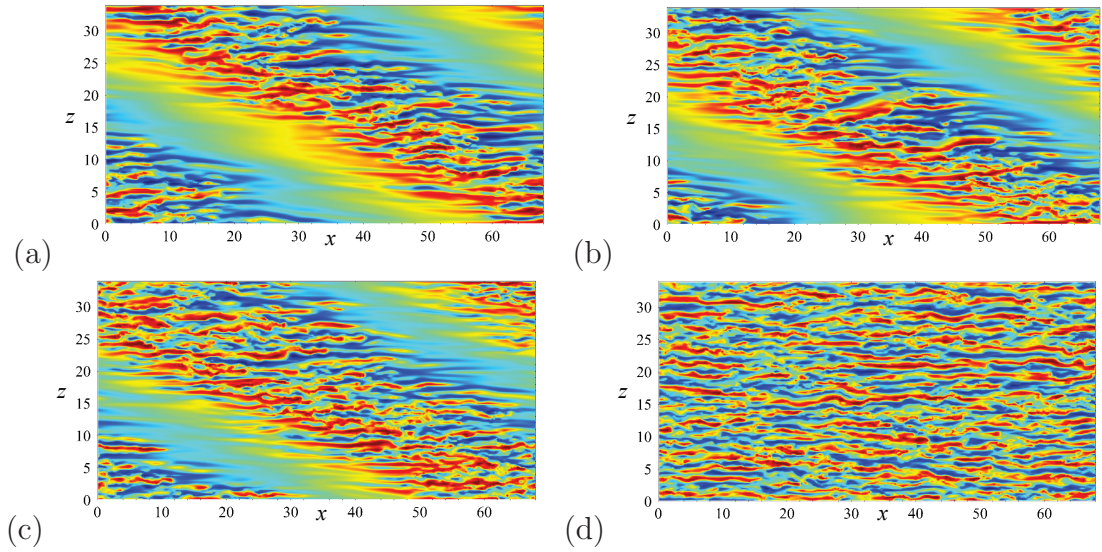


Fig. 4.11 Contours of u'_x near mid-gap for one rough wall and rectangular-shaped profile for $Re_w = 1300$ and $h/d =$ (a) 0 (b) 0.05, (c) 0.075, (d) 0.1. Contours range from -0.25 (blue) to 0.25 (red). The wall-normal position corresponds to the minimum of the mean velocity gradient outside the rough region.

model, can shed light on the mechanisms ruling laminar-turbulent patterns.

The first regime to be described is shown in Fig. 4.12 using the same planar representation as in Fig. 4.11. The flow feature shown in Fig. 4.12 corresponds to stripe patterns found for Re_w below the reference value of $Re_g(h = 0) \approx 1300$. In the smooth case, such patterns would in principle be reported as transients, with mean lifetimes decreasing fast for smaller Re_w , see Manneville (2011). Identifying a sustained stripe pattern at $Re_w = 1100$ and 900 , i.e. respectively 15% and 30% below $Re_g(h = 0)$, suggests that strong roughness on one wall can prevent the pattern from breaking up and from subsequently relaminarizing: the additional force mimicking the drag induced by roughness elements also triggers instability mechanisms able to continuously force the stripe pattern. Note that the pattern identified for $Re_w = 900$ displays wavelengths of approximately half their usual size. Given that the wavelength of the pattern is expected to scale as d . This phenomenon is at least consistent with the decrease of the effective gap $d_{\text{eff}}(h) = d - \eta(h)$ seen by the turbulent structures away from the rough layer. The exact factor $1/2$ observed here is most likely linked to the periodicity constraint that prevents the wavelength from varying continuously as a function of η or h .

Another interesting regime is shown in Fig. 4.13 and is marked with green triangles in Fig. 4.10. The flow exhibit one or several laminar spots evolving in a turbulent environment. These laminar regions have finite lifetimes but recurrently regenerate from the fluctuating turbulent environment (Duguet et al., 2010). They also display the usual oblique laminar-turbulent interface. Such regimes are encountered in the smooth case for $Re \approx Re_t$, where $Re_t > Re_g$ (despite the genuine difficulty in defining Re_t) marks the

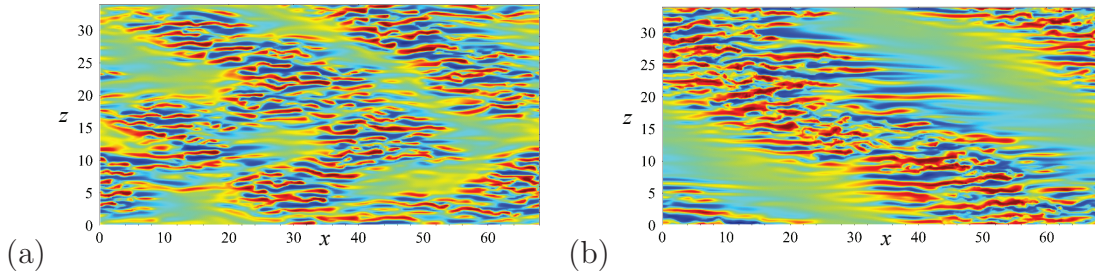


Fig. 4.12 Contours of u'_x near mid-gap for one rough wall and rectangular-shaped profile for $(\text{Re}_w, h/d) =$ (a) (900, 0.25) and (b) (1100, 0.1). Contours range from -0.25 (blue) to 0.25 (red). Wall-normal position where mean velocity gradient is minimal outside the roughness region.

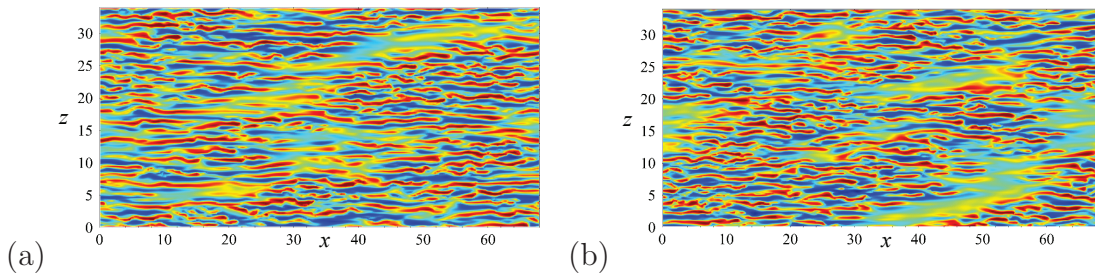


Fig. 4.13 Contours of u'_x near mid-gap for one rough wall and rectangular-shaped profile for $(\text{Re}_w, h/d) =$ (a) (1000, 0.2) and (b) (1000, 0.25). Contours range from blue to red are from -0.25 to 0.25 . Wall-normal position where mean velocity gradient is minimal outside the roughness region.

boundary between stripe patterns and patternless turbulence. Taking into account that high roughness shifts the whole pattern regime (including the value of Re_t) down in Re_w , it is a-posteriori not surprising to identify stripe patterns for $\text{Re}_w < \text{Re}_g(h = 0)$ as soon as $\text{Re}_t(h \neq 0) < \text{Re}_g(h = 0)$. The parameter corresponding to our observations, namely $\text{Re}_w = 1000$, indeed verifies the hypothesis $\text{Re}_t(h \neq 0) < \text{Re}_g(h = 0)$ (see Fig. 4.10).

The next interesting regime has this time no strict equivalent in smooth pCf. This regime occurs for $(\text{Re}_w, h/d) = (900, 0.2)$ and $(1000, 0.15)$, which are marked with purple inverted triangles in Fig. 4.10. The flows are visualized in Fig. 4.14(a-b) and corresponds to a turbulent zone localized in the streamwise direction only. Perhaps even more is the quasi-absence of oblique laminar-turbulent interface. In order to verify that this regime is not influenced by periodic boundary conditions, another simulation has been performed in a numerical domain with doubled L_x and L_z for $(\text{Re}_w, h/d) = (900, 0.2)$. Figure 4.14 demonstrates that the regime is robust to the domain change and is not a numerical artifact due to boundary conditions. Duguet and Schlatter (2013) justified the usual presence of oblique interfaces in planar shear flows by invoking continuity to resolve the mismatch of streamwise flow rates at any laminar-turbulent interface. This unavoidable mismatch is resolved by the presence of a large-scale spanwise flow advecting the interfaces obliquely. The present situation obviously violates this mechanism, which represents an interesting

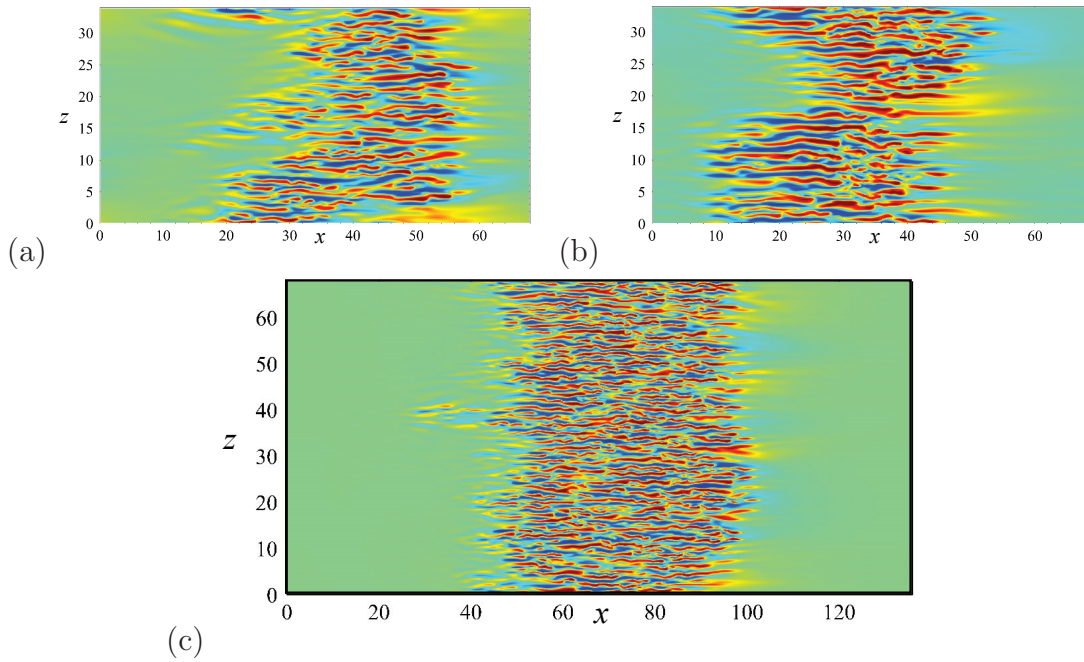


Fig. 4.14 Contours of u'_x near mid-gap for one rough wall and rectangular-shaped profile for $(\text{Re}_w, h/d) =$ (a) (900, 0.2) and (b) (1000, 0.15). Contours range from blue to red are from -0.25 to 0.25 . (c) Larger computational domain $(L_x, L_z) = (136d, 68d)$ for $(\text{Re}_w, h/d) = (900, 0.2)$.

opportunity to test its limits. The argument in Duguet and Shlatter (2013) relies on the two-dimensionalised continuity equation

$$\frac{\partial \overline{U}_x}{\partial x} = -\frac{\partial \overline{U}_z}{\partial z}, \quad (4.4)$$

where capital letters and ovelines denote large-scale flow and y -integration from wall to wall, respectively. In the presence of smooth walls, y -integration makes the term $\partial U_y / \partial y$ vanish because of the zero relative flux across the two walls. As a consequence the streamwise acceleration/deacceleration at the laminar-turbulent interface is compensated by a large-scale spanwise flow. The situation is less clear in the presence of roughness, since the non-rough region $y \in [\eta(h) : d]$ is not characterized by a genuinely zero wall-normal flux: fluid can be ejected inwards or outwards from the rough region $[0 : \eta(h)]$. This yields a non-zero $\partial \overline{U}_y / \partial y$ in the roughness-free area of $\eta(h) < y < d - \eta(h)$ and, thereby, Eq. (4.4) must be replaced by

$$\frac{\partial \overline{U}_x}{\partial x} = -\frac{\partial \overline{U}_y}{\partial y} - \frac{\partial \overline{U}_z}{\partial z}. \quad (4.5)$$

The main consequence of Eq. 4.5 is that streamwise mean flow modifications can either be compensated by spanwise or wall-normal transport, or by a combination of both. Depending on the ratio between the spanwise and the wall-normal flow rates, the in-plane angle of the laminar-turbulent interface with the streamwise direction can vary from finite to 0

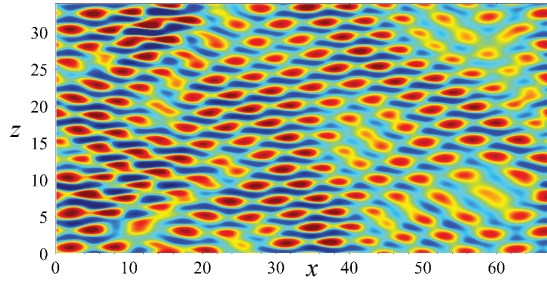


Fig. 4.15 Two dimensional contours for u'_x in x (horizontal: L_x/d)- z (vertical: L_z/d) plane in the pCf with one rough wall of a box profile at $Re_w = 800$ and $h/d = 0.25$. Contours range from blue to red are from -0.025 to 0.025 . Wall-normal position is at where mean velocity gradient is minimum value without roughness region.

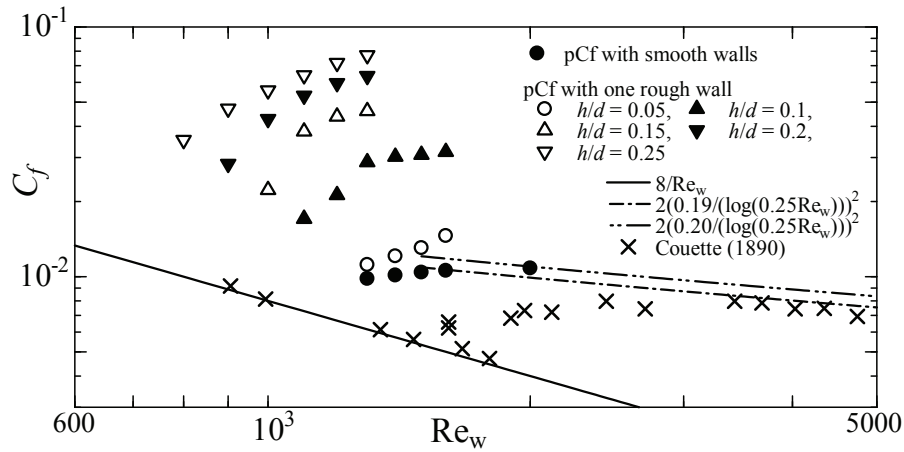


Fig. 4.16 Friction factor of one-rough-wall pCf with rectangular-shaped roughness elements.

(or 90 degrees) if U_y dominates over U_z . This is apparently the situation occurring here for high h/d and low Re_w , justifying the observed non-obliqueness of the laminar-turbulent interfaces. Note that a similar mechanism has been advanced to explain the lack of oblique interfaces in a boundary layer flow with suction (Khapko et al., 2016).

The last non-trivial regime detected was found for $(Re_w, h/d) = (800, 0.2)$, i.e., the lowest value of Re_w and the largest value of h/d we tested, which is marked with an orange cross in Fig. 4.10. It consists of an almost regular staggered array of vortical structures (see Fig. 4.15) sustained in time, with velocity magnitudes of one order magnitude than those in the previous cases. This flow hardly features any coherent structure like ‘elongated streamwise streaks’. Note that the same pattern was also identified transiently during relaminarization for neighboring parameters sets $(Re_w, h/d) = (800, 0.2)$ and $(700, 0.25)$. It remains to be investigated how spurious such structures are, and whether they have an experimental counterpart.

The friction factor C_f , defined again as $C_f = 2\tau_t/(\rho u_m^2)$ is shown in Fig. 4.16. Differences from the two-rough wall case are minor except for the lowest values of Re_w , at which one rough wall clearly displays less friction than with two rough walls.

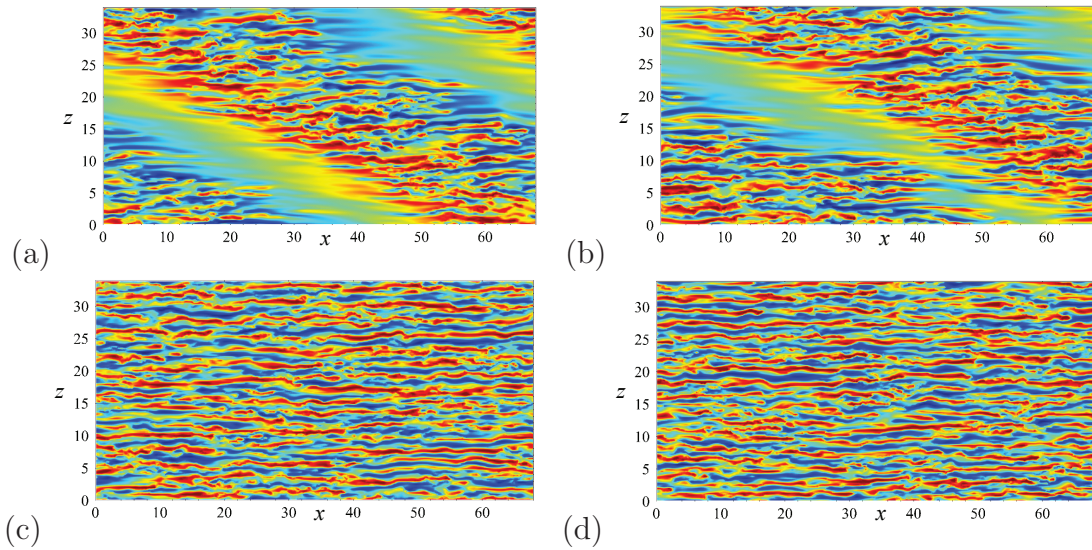


Fig. 4.17 Contours of u'_x near mid-gap for one rough wall and Gaussian-shaped profile for $Re_w = 1300$ and at $h/d =$ (a) 0.025, (b) 0.05, (c) 0.075 and (d) 0.1. Contours range from -0.25 (blue) to 0.25 (red).

4.4.2 Gaussian-shaped roughness elements

In order to test the robustness of the results in the presence of a single rough wall, a restrained set of simulations of the model is conducted with Gaussian rather than rectangular-shaped roughness elements. The value of Re_w is held fixed at 1300 (close to $Re_g(h = 0)$) and the roughness height is increased in steps of 0.5. The results with Gaussian and rectangular-shaped roughness elements are hardly indistinguishable (see Fig. 4.17 and compare with Fig. 4.11) : the turbulent fraction slowly grows with increasing h/d until the patterns are destroyed. As similarly to the two-rough wall case, the Gaussian-shaped roughness provides rather enhanced fluctuations, or wider bands of localized turbulence.

4.5 Summary

The robustness of laminar-turbulent patterns in plane Couette flow to wall roughness has been investigated numerically using direct numerical simulation in a plane geometry coupled with the Busse-Sandham model. The roughness density was fixed to $\alpha d = 1$ and a parametric study was performed using two free parameters: the Reynolds number Re_w and the mean roughness height h/d , for either one or two rough walls. It was demonstrated that oblique stripe patterns are typically robust for small roughness $h/d \leq 10\%$, at the price of a wider turbulent region. This is consistent with their observation in experiments where the walls possess small but finite roughness. No oblique pattern was detected for larger values of h/d but laminar-turbulent coexistence could be maintained in some form (oblique or not) for h/d up to 20% in the cases with one rough wall. The onset Reynolds number Re_g for the sustenance of such oblique patterns was found to be robust (≈ 1300)

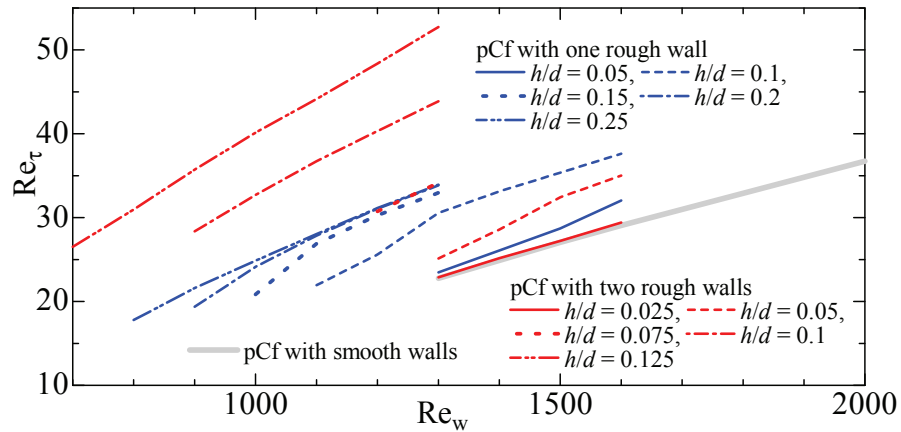


Fig. 4.18 Friction Reynolds number Re_τ vs. bulk Reynolds number Re_m for all cases discussed in Sections 3 and 4.

for two rough walls but typically decreases with increasing h/d for the cases with one rough wall only.

The energetic efficiency of rough plane Couette flow has been compared to that of smooth plane Couette flow using the friction factor plots $C_f(Re_w)$ analogous to a Moody diagram for cylindrical pipe flow (Figs. 4.7 and 4.16). The determination of C_f involves an estimation of the total shear stress τ_t (involving the roughness term) rather than the sole term τ_w that measures the drag at the flat wall. Similarly, a friction Reynolds number Re_τ can be defined using τ_t (rather than τ_w) by

$$Re_\tau = \frac{u_\tau d}{\nu}, \quad u_\tau = \sqrt{\frac{\tau_t}{\rho}}. \quad (4.6)$$

The quantity of Re_τ is plotted in Fig. 4.18 as a function of the usual Reynolds number Re_w . Not surprisingly, the effect of wall roughness predicted by the model is an increase in Re_τ , quantitatively stronger for two rough walls than for one rough wall. This expresses the deterioration of the energetic efficiency of the systems with increasing roughness height.

Interestingly, assessing why and how laminar-turbulent patterns break down in the presence of roughness is a subtle way to interrogate the physical mechanisms by which they are usually sustained. The dynamic sustenance of non-trivial flow motion can be investigated in two different ways: a local approach, concerned with the local regeneration of streamwise streaks, or a global approach that considers localized turbulent structures as a global entity.

We first address here the local sustenance mechanisms in the light of the self-sustained process (SSP) suggested by Waleffe (1997). This nonlinear process considers, in the absence of roughness, that decaying streamwise vorticity first advects streamwise velocity to create streamwise streaks by the lift-up effect. These streaks then undergo an inflectional instability generating three-dimensional vorticity, some of which reinforces the streamwise

vorticity. If that feedback is strong enough, it prevents the original streamwise vorticity from decaying, which sustains the streaky motion. Both the lift-up effect and the nonlinear feedback are enhanced for higher Reynolds numbers. The whole SSP loop implies a quasi-cyclic regeneration of the streamwise vorticity and streaks as long as $Re \geq Re_g$. Below Re_g , the contribution of streak instability to the vorticity is too weak to prevent it from eventually decaying. Physically, we expect roughness elements, independently from their location, density and height, to contribute spontaneously to the generation of vorticity (including the streamwise vorticity component) via shedding or inflectional instabilities. The introduction of parametric roughness allows the nonlinear feedback stage to be by-passed since streamwise vorticity can be regenerated by the contribution of the roughness elements rather than from the streak instability (Bottin et al., 1998). In other words each roughness element acts as a vortex generator. The onset Re_g can hence be lowered in the presence of roughness because the local SSP is by-passed by the introduction of new vorticity sources. It is natural to expect that higher roughness h , or equivalently larger density α , allows for further reduction of Re_g . This reduction of Re_g with h is indeed observed here in Figs. 4.4 and 4.10, though the dependence of Re_g on h differs in both cases and is more marked with one rough wall only. This picture suggests to distinguish, independently of h and α , between self-sustained and forced turbulence, both occurring for Re_w respectively above and below $Re_g(h = 0)$. Forced turbulence is defined by the property that it would decay rapidly if the roughness would suddenly be turned off. In practice the distinction between the two types of dynamics is not crucial. Fig. 4.19 shows two realizations of turbulence in the presence of high roughness on two walls, visualized by the iso-contours of streamwise velocity at mid-gap. Fig. 4.19(b) corresponds to forced turbulence since $Re_w=700 < Re_g(h = 0)$, whereas Fig. 4.19(a) has $Re_w=1300 \approx Re_g(h = 0)$ and corresponds to self-sustained turbulence. Both examples display an array of elongated streamwise streaks with similar velocity levels and comparable wavelengths (the spanwise wavelength is known to scale in inner units that shrink slightly with increasing Re_w). The occurrence of streak breakdown events (noticeable in these instantaneous flow states by the loss of neat spanwise periodicity and by smaller-scale fluctuations) is however visually much more pronounced for the self-sustained case than for the forced case.

The global approach to sustained shear flow turbulence addresses the stability of localized turbulent patches seen as fully coherent structures rather than as juxtapositions of independent and local SSP processes. This point of view is better suited to the investigation of the self-organization of turbulence into laminar-turbulent patterns. The argument of Duguet and Schlatter (2013) justifies the obliqueness of the laminar-turbulent interfaces provided there is i) streamwise localization and ii) absence of large-scale wall-normal transport. The absence of strong large-scale wall-normal transport is expected for low- Re wall turbulence. Though it is established for smooth walls and small h/d , this hypothesis was invalidated in the case of one rough wall for high roughness elements $h/d > 15\%$ and $Re_w \leq 1000$. The main consequence in the latter case is the lack of obliqueness of the interfaces for

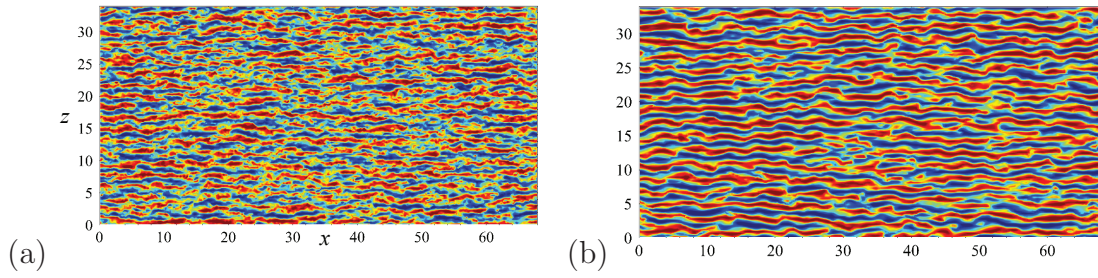


Fig. 4.19 Contours of u'_x at mid-gap with two rough walls and rectangular-shaped roughness elements: (a) $h/d = 0.125$ and $Re_w = 1300$; (b) $h/d = 0.25$ and $Re_w = 700$. Contours range from -0.25 (blue) to 0.25 (red).

streamwise localized turbulent spots. The underlying physical mechanism is expected to be observable in experiments with one rough wall only: high roughness elements strongly break the top-down anti-symmetry of the flow, resulting in different streamwise flow rates at the two sides. By continuity, this sustains strong wall-normal currents at large scales which breaks the interface obliqueness. The property of streamwise localization of turbulent patches remains, in turn, the most crucial but the least understood properties or low- Re turbulent flows. Barkley (2016) justifies it, for the companion problem of smooth pipe flow, by a recovery property of the mean velocity profile. The mean profile distortion due to some localized turbulent fluctuations prevents the sustenance of new fluctuations immediately downstream of itself, implying streamwise localization of turbulence—at least at low Re . The transition from patterned to patternless turbulence occurring at Re_t is attributed in this picture to an excitability-bistability transition blurred by the stochastic nature of the fluctuations.

5

Investigations of rotation effect on laminar-turbulent pattern

5.1 Large-scale structure alternation

5.1.1 Coriolis effects on the transitional regime

In order to demonstrate the switch of dominant large-scale structure in the flow, three-dimensional visualizations of turbulent vortexes are shown in Fig. 5.1. The second invariant of the deformation tensor, defined as

$$II' = \frac{\partial u'_i}{\partial x_j} \cdot \frac{\partial u'_j}{\partial x_i}, \quad (5.1)$$

is used for the identification of the vortex region that exhibits either a circular or spiral motion (but not a simple shear motion). Also shown in the figures are contours of the streamwise velocity fluctuation in y - z planes at several locations. Note that each figure shows different typical flow states: Fig. 5.1 (a) is obtained at very low Ro_τ and reveals a spatially intermittent turbulence with two localized turbulent bands (stripe pattern); Fig. 5.1 (b) shows dominating roll cell as the only characteristic structure, observed at high Ro_τ ; and Fig. 5.1 (c) shows a transitional state with the coexistence of turbulent bands and large-scale longitudinal vortexes (roll cells). To describe the structures further, we also present the x - z contours of the instantaneous streamwise velocity fluctuation in the buffer layers on the pressure side and on the suction side in Fig. 5.2. Here, let us categorize flow states into the following three, based on large-scale structures:

- SP state, where the stripe pattern occurs without any roll cell,
- Tr state, which is a transition state between the SP and RC states,
- RC state, where the roll cells are dominant in the whole area.

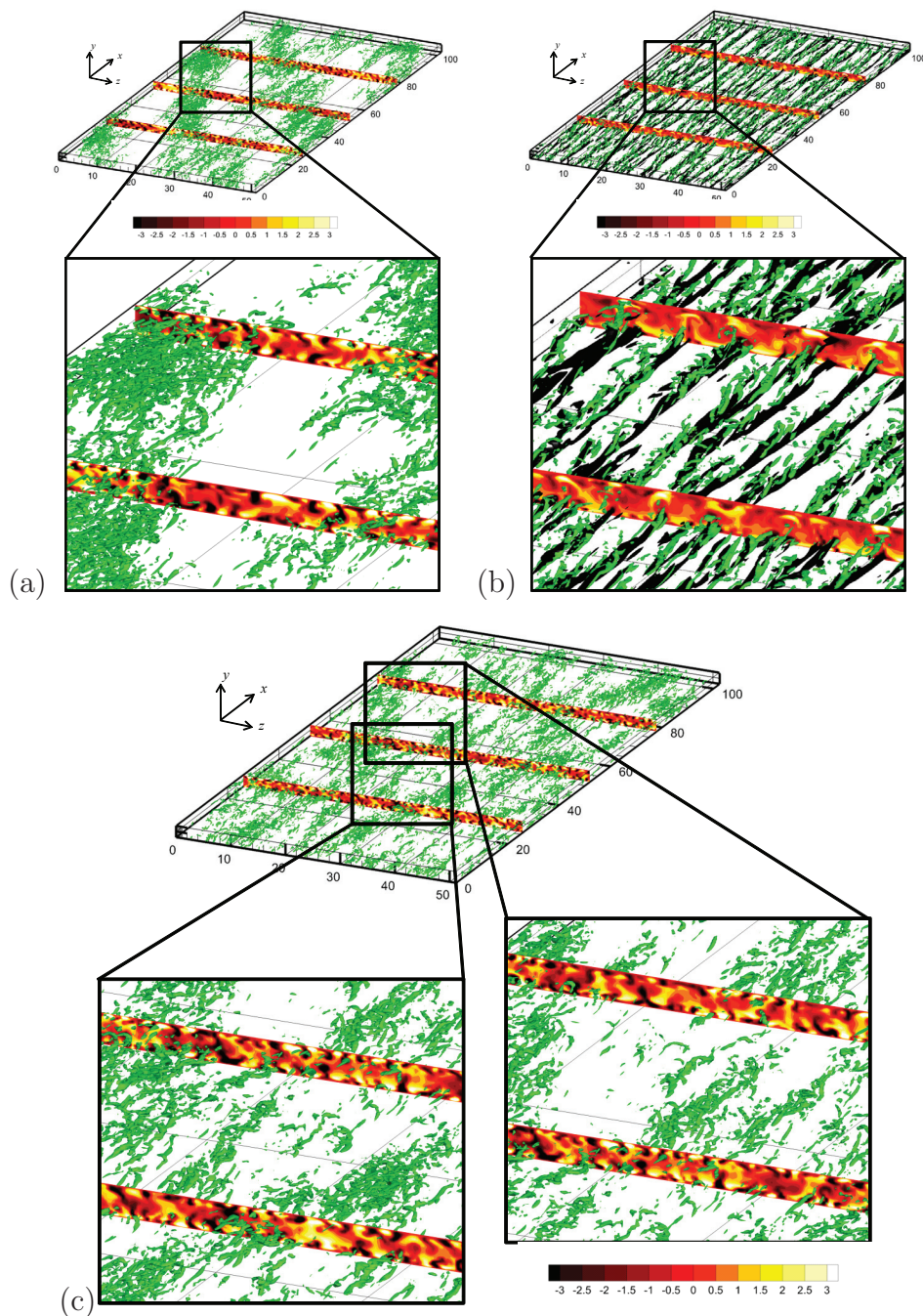


Fig. 5.1 Visualization of instantaneous flow field at $Re_\tau = 80$ and $Ro_\tau =$ (a) 0.01, where the stripe pattern occurs clearly, (b) 1.5, where the longitudinal roll cells are evenly distributed, and (c) 0.05, where the flow includes both the stripe pattern and roll cells. Green iso-surfaces indicate regions of $II^+ = u'_{i,j}u'_{j,i} < -0.025$ and are equivalent to the vortical position. Contours in arbitrary y - z planes show u'^+ . Black iso-surfaces indicate low-speed regions ($u'^+ < -3.0$). The mean flow moves from bottom-left to top-right.

As observed in Fig. 5.1(a), the structure of stripe pattern is clearly found in the range of $0 \leq Ro_\tau \leq 0.02$, on both the pressure and suction sides. Its characteristic features are the spatial alternation of the quasi-laminar region and the turbulent band (in which fine-scale

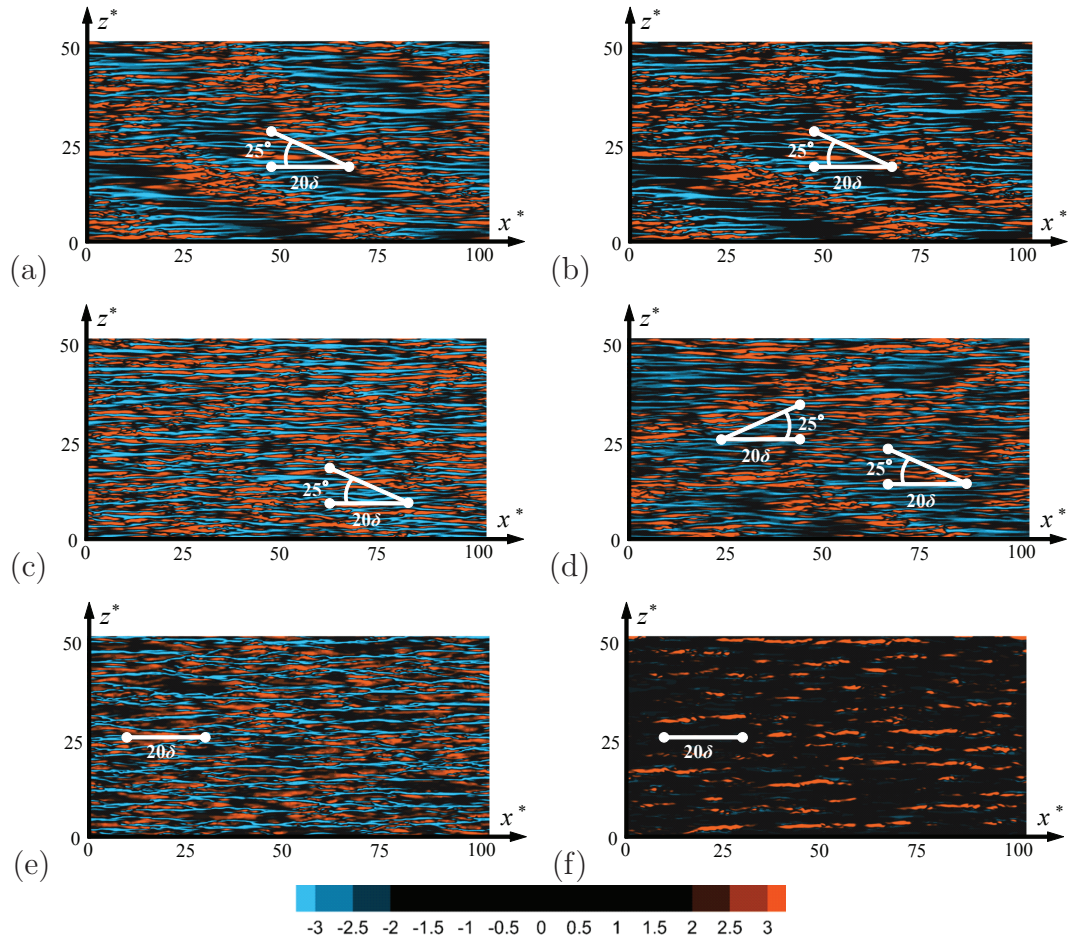


Fig. 5.2 Contours of instantaneous u'^+ in the x - z plane at (a, c, and e) $y^* = -0.86$ (the pressure side) and at (b, d, and f) $y^* = 0.86$ (the suction side) for different rotation numbers, showing different flow states: (a and b) stripe pattern at $Ro_\tau = 0.01$, (c and d) transition states from stripe pattern to roll cell at $Ro_\tau = 0.05$, and (e and f) roll cell at $Ro_\tau = 1.5$. The friction Reynolds number is fixed at $Re_\tau = 80$. The mean flow moves from left to right. The whole area of the computational domain is visualized: $102.4\delta \times 51.2\delta$ in x and z .

eddies are clustered) and the inclined pattern against both the streamwise and spanwise directions with a certain angle. The densely gathering eddies may give rise to locally large frictional drag in the turbulent region and then the high and low-speed streaks are induced in the upstream and downstream regions of the turbulent region, respectively: cf. (Tsukahara et al., 2006 and 2010a). As seen in Figs. 5.2(a) and (b), positive and negative u' are observed intermittently and unevenly distributed. One may find large-scale motions in the form of oblique patterns inclining with respect to x at 25° – 30° . Other regions apart from the turbulent bands are close to the laminar state accompanied by relatively small velocity fluctuations, and the turbulent eddies are not observed so much (Fig. 5.1 (a)). A difference of flow states between the two side is almost absent in the state of stripe pattern.

In addition, we found somewhat enhanced stripe pattern features at $Ro_\tau = 0.01$.

As shown in Figs. 5.2 (c) and (d), we found a structure involving the coexistence of stripe pattern and roll cells in an intermediate region between (a, b) and (e, f) of the figures. We can observe a turbulent-laminar banded pattern, similar to the state of stripe pattern, although the organization pattern may be vague compared to that visualized in Figs. 5.2 (a) and (b). In Fig. 5.2 (c), the stripe pattern on the pressure side is somewhat fuzzier than that on the suction side in Fig. 5.2 (d), where one may recognize the appearance of inclined bands of assembled high-speed streaks (positive u') with a streamwise interval of $\Delta x \approx (50\delta)$ and a spanwise interval of $\Delta z \approx (20\delta)$, similar to the observed stripe pattern in the literature (Tsukahara et al., 2010a). A comparison between Figs. 5.2 (a) and (c) reveals a difference in the typical length of low-speed streaky structures, which extends from finite to infinite in x as the state changes from SP to Tr. The infinitely-long streamwise streaks caused by the roll cells simultaneously exist with a stripe patterns in the Tr state, especially, on the pressure side. Indeed, the distribution of visualized eddies in Fig. 5.1 (c) implies longitudinally-clustering structures as well as the spatially large-scale intermittency of turbulence. The elongated cluster of eddies in the streamwise direction is attributed to the longitudinal vortexes of roll cells, and it appears mainly on the pressure side. We consider that this coexistent state occurs in the process of disappearance of stripe pattern and the development of roll cells on the pressure side. In the structure of stripe pattern, the wall-normal turbulent intensity $\overline{v'v'}$ is not strong because stripe pattern is accompanied by the spanwise secondary flow along the turbulent bands, but does not have a large wall-normal component (Tsukahara et al., 2006). In contrast, roll cells have an intense wall-normal component, since roll cells involve large-scale vortical motions. The turbulent intensity of each direction should be significantly affected by the Coriolis effect and thereby the large-scale structures are altered.

Figure 5.1 (b) allows us to confirm the dominance of roll cells, showing elongated streaky structures along the streamwise direction. We can identify neither the occurrence nor the effect of stripe pattern in the roll cells state. The low- and high-speed streaks coexist on the pressure side (see Fig. 5.2 (e)), whereas only high-speed streaks seem to dominate on the suction side at high Ro_τ (Fig. 5.2 (f)). In the literature, the dependence on the rotation number of the presence or absence of roll cells was reported (Johnston et al., 1972; Iida et al., 2010) and the instability of roll cells (Kristoffersen et al., 1993; Tafti et al., 1991) has been investigated well. In this study, the dependence of roll cells is found to basically agree with the existing results. The structure of roll cells on the pressure side is unstable so that its vortical motion would affect the flow on the suction side, where the roll cells are essentially not triggered. Therefore, the influence of the elongated streamwise streaks due to roll cells is observed not only on the pressure side but also on the suction side. From the results of Fig. 5.1 (b), the fine-scale eddies are found on the pressure side, especially around the low-speed streaks.

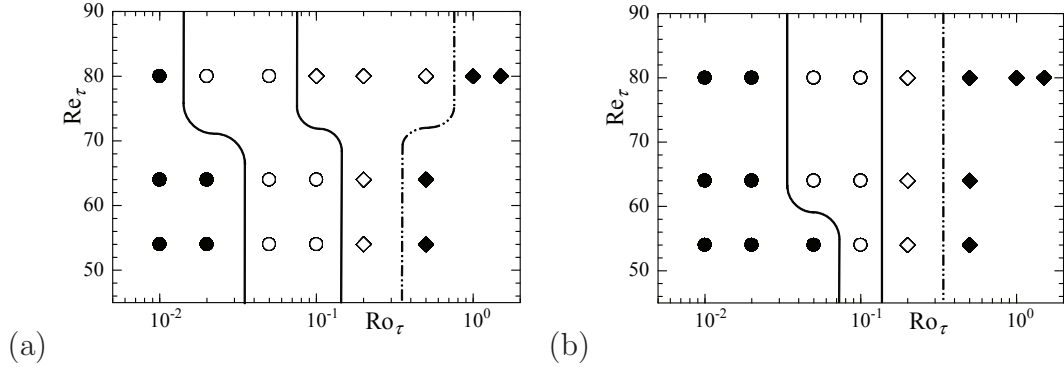


Fig. 5.3 Flow maps for each side of the channel: ●, stripe pattern (SP); ○, transitional state (TR) between SP and RC; ◇, roll cells (RC); ◆, roll cells (RC2, high- or low-speed streaks is prominent). (a) pressure side, (b) suction side.

On the basis of the flow visualizations, we have summarized various turbulent states in flow maps for each side, as given in Fig. 5.3. As just described above, the SP state occurs at only very low Ro_τ and, as consistent with previous reports, roll cells become dominant with the increase of Ro_τ . We determined transition states, labeled as Tr, from a static- to a rotating-system, where both stripe pattern and roll cells can stably coexist. Although the Reynolds-number dependency is still not elucidated clearly from the flow map, the SP state seems to widely occur for the lower Reynolds numbers. Further investigation is needed to discuss the variations of the transitional Reynolds number regime that might be changed depending on the rotation number. The effect of strong spanwise rotation at substantially-higher Reynolds numbers than those used in earlier studies was recently investigated by Brethouwer et al. (2011) through DNS at Ro_m up to 2.4. A key finding of their DNS at high Ro_m and high Re_m was that a strong cyclic instability similar to the Tollmien-Schlichting wave would occur on the suction side and made the flow unstable and it broke down into turbulence. This parameter regime for which the instability can occur on the suction side could not be found in the presently tested parameter range.

5.1.2 Friction factor

When $\Omega \neq 0$, we confirmed the coexistence of stabilized and destabilized regions in the rotating channel. Hereafter, those regions are discriminated according to the S criterion: i.e., the bottom side of the channel exhibits $S < 0$, and is referred to as the pressure side, while the top side ($S > 0$) is referred to as the suction side. In this study, we decided to define simply the border of the two sides as the maximum- \bar{u} height at which $d\bar{u}/dy = 0$. Figure 5.4 shows the mean velocity profiles for different rotation numbers at the friction Reynolds number fixed at 80. The profiles for low Ro_τ seem to be symmetric with respect to the channel center ($y = 0$), which is similar to the case of the static channel.

As Ro_τ increases, the wall-normal height of the velocity peak shifts toward the suction

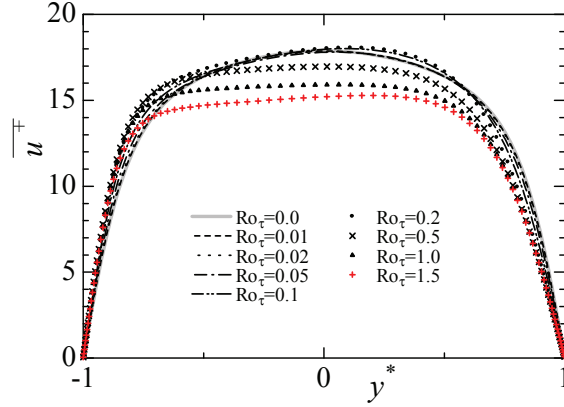


Fig. 5.4 Mean streamwise velocity profile at $Re_\tau = 80$.

side. With increasing Ro_τ , the near-wall velocities in the pressure and suction sides, respectively increase and decrease monotonically, whereas the core-region velocity reveals relatively complex behavior as a function of the rotation number. In the core region ($-0.5 < y^* < 0.5$), the magnitude of \bar{u}^+ for $Ro_\tau \leq 0.2$ is slightly larger than that of $Ro_\tau = 0$, but for $Ro_\tau > 0.2$ it decreases with increasing Ro_τ . This critical Ro_τ of 0.2 (i.e., a turning point of the rotation-number dependency) corresponds to the beginning of roll cells' dominance due to high Ro_τ , irrespective of the pressure and suction sides. It should be noted that this alternation of the most dominant structure occurs when the suction-side flow state is close to the relaminarization.

For more detailed discussion, the normalized friction velocities of $u_{\tau p}/u_\tau$ and $u_{\tau s}/u_\tau$ with respect to each wall of the channel are shown in Fig. 5.5(a) as a function of the bulk rotation number Ro_m , which is normalized by the bulk mean velocity $u_m = 0.5 \int_{-1}^1 \bar{u} dy^*$ instead of u_τ . Here, the two rotation numbers are given as

$$Ro_m = \frac{u_\tau}{u_m} Ro_\tau. \quad (5.2)$$

Also shown in Fig. 5.5(a) for a comparative verification are the experimental result by Nakabayashi et al. (1996) and the DNS result by Iida et al. (2010).

As in the figure, Ro_m (corresponding to a resultant parameter in our DNS) is applied instead of Ro_τ (a control parameter), since the friction velocity u_τ at each side of the channel is generally difficult to measure precisely in experiments. The difference between $u_{\tau p}$ and $u_{\tau s}$ can be detected even at a very low rotation number and is roughly proportional to Ro_m . The increasing rate of the difference gradually slows down in $Ro_m > 0.01$ and there is no significant change for $Ro_m > 0.03$, which is in good agreement with earlier numerical and experimental results at other Reynolds numbers (Iida et al., 2010; Nakabayashi et al., 1996). This plateau appears at both walls. The weak Reynolds-number dependence of the plateau in the high Ro_m regime is also verified by the present DNS: the ratio of $u_{\tau p}/u_{\tau s}$ is larger at the larger Reynolds number. Our DNS study focusing on a wide range of Ro_m has

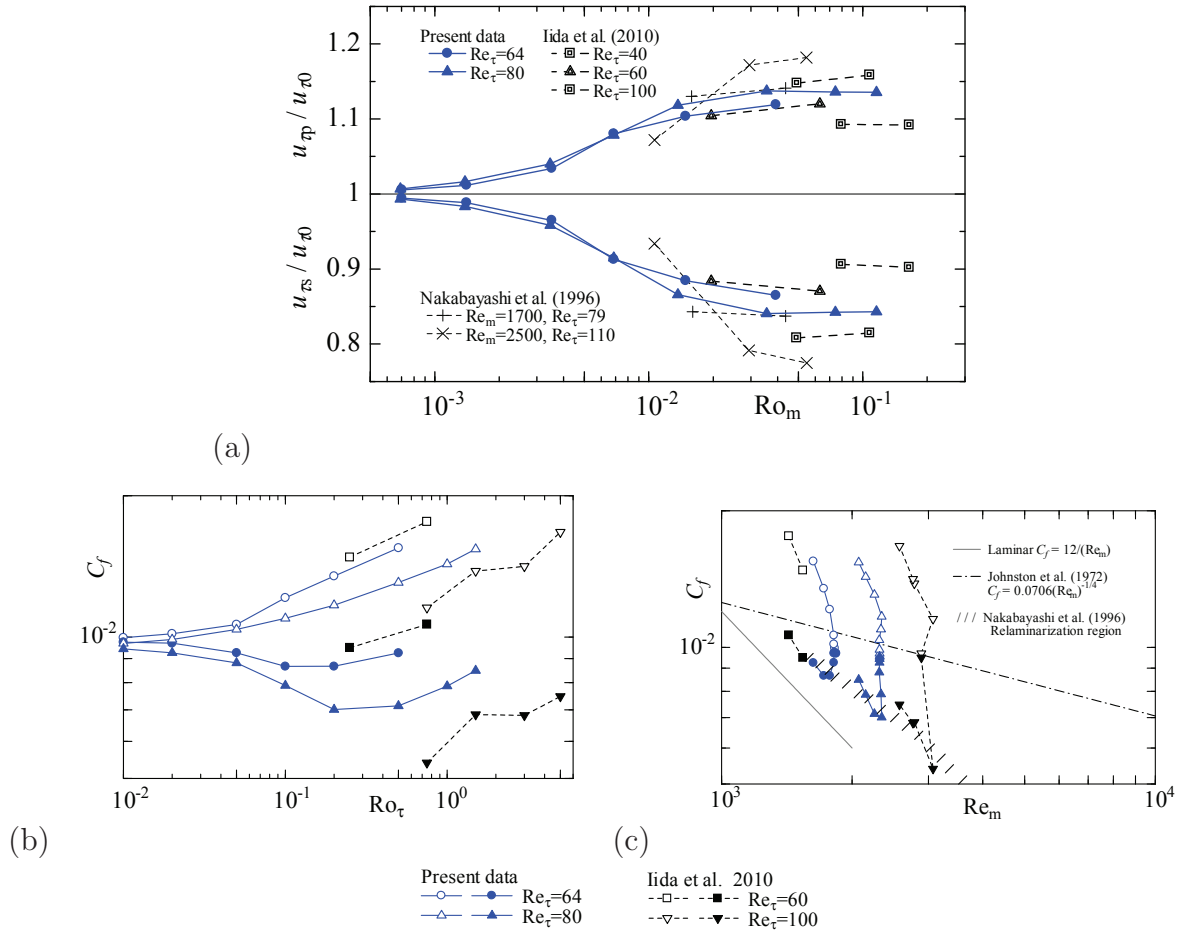


Fig. 5.5 (a) Local friction velocity at each wall ($u_{\tau p}$, pressure side; $u_{\tau s}$, suction side) as a function of Ro_m . Local skin-friction coefficient at each wall *versus* Ro_τ (b) and Re_m (c). Open and filled symbols represent the pressure-side and suction-side values, respectively. For comparison, DNS data (Iida et al., 2010) and the relaminarization region explored experimentally (Nakabayashi et al., 1996) are also shown. The dashed-dotted line in (b) is an empirical correlation function for the non-rotating turbulent channel flow (Johnston et al., 1972).

uncovered significant rotation-number dependence and less Reynolds-number dependence in the low Ro_m regime.

Figures 5.5 (b) and (c) displays the variation of the skin friction coefficient at each wall: $C_f = u_{\tau p}^2/2u_m^2$ or $u_{\tau s}^2/2u_m^2$. The horizontal axis represents either Ro_τ or Re_m . Note that $Re_m = 2u_m\delta/\nu$ undergoes a change because of the present calculation that was performed under the fixed Re_τ (constant pressure gradient) condition.

As seen in Fig. 5.5 (b), monotonic increases of C_f with Ro_τ clearly appear on the pressure side, while this is not the case for the suction side. There exists a local minimum of C_f at $Ro_\tau = 0.2$, that also results in the maximum Re_m for a given Re_τ . This means that the net drag reduction can be achieved by the spanwise system rotation at relatively low

Ro_τ , although the reduction rate is very small. This net drag reduction may be caused by the suppression of turbulence on the suction side, approaching the maximum when relaminarization occurs on this side. It can be confirmed from Fig. 5.5(b) that some points in the C_f - Re_m plot are settled in the relaminarization region, which was proposed by Nakabayashi et al. (1996) for $Ro_\tau \geq 0.2$. The state of the turbulent structure on the pressure side is dominated by roll cells for $Ro_\tau \geq 0.2$, and the turbulent activity is almost attenuated on the suction side. As Ro_τ is increased from 0.2, the C_f values of both the pressure and suction sides are seen to increase. This is because the wall-normal momentum transfer is enhanced by vortical motions of roll cells and intensifies the near-wall velocity gradient ($d\bar{u}/dy$) in both sides. As a result, the drag augmentation on both walls induces a decrease of Re_m . The above variations of the parameter dependences may be closely related to the alternation of the dominant turbulent structure in the turbulent flow field of each side.

5.2 Augmentation of spanwise secondary flow of the pattern

5.2.1 Stripe pattern in weak rotation

The occurrence of turbulent stripe is found in the pPf with spanwise system rotation, as given in Fig. 5.6, but it is limited only at Ro_τ lower than the previously investigated Ro_τ range by existing studies on the pPf with spanwise system rotation (Kristoffersen et al., 1993; Iida et al., 2010).

We confirmed that, under the condition of no/weak system rotation, turbulent stripe did not decay for a long time, at least, the averaging time of $\Delta T^+ = 25600$ (corresponding to 55 wash-out times of the bulk flow). The rotation number range, in which stripe pattern is the dominant structure on both the pressure and suction sides, is $Ro_\tau \leq 0.02$ for $Re_\tau = 64$. A typical snapshot of the flow field accompanied by stripe pattern under the system rotation is shown in Fig. 5.6, where one can see a single oblique band of localized turbulence at $Re_\tau = 0.02$. The structure of stripe pattern consists of the quasi-laminar region and the turbulent region, and these regions stably co-exist in alternate shifts. In the turbulent region, the vortexes densely occur between high- and low-speed streaks, and the local centerline velocity is lower than that in the quasi-laminar region. The quasi-laminar region exhibits fewer streaks of velocity fluctuation, and this region reveals a relatively large velocity at the channel center, like the laminar flow. As a result, the quasi-laminar region impinges on the turbulent region with a relatively low speed of propagation. Then, the streamwise velocity decreases rapidly at the interface of the two regions (turbulent and quasi-laminar regions). In the area downstream of the turbulent region, the streamwise velocity is accelerated gently until the next downstream turbulent region occurs or until

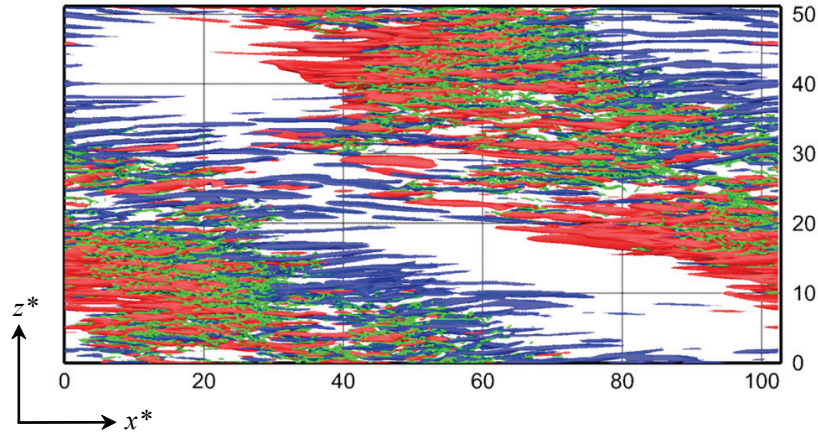


Fig. 5.6 Three-dimensional visualization of an instantaneous flow field at $Re_\tau = 64$ and $Ro_\tau = 0.02$, viewed from the wall-normal direction. Red isosurface, $u'^+ > 3$; blue, $u'^+ < -3$; green, $II'^+ = u'_{i,j}u'_{j,i} < -0.01$ (which is equivalent to the vortical position). The mean flow moves from left to right.

it reaches the relevant laminar velocity. In consequence, local high- and low-speed regions occur, respectively upstream and downstream of the turbulent band. Other explanations for the large-scale flow structure formation are also given by other researchers (Duguet et al., 2013; Fukudome and Ida, 2012, Seki and Matsubara, 2012). Fukudome and Iida (2012) investigated how the secondary flow was persistently sustained from the viewpoint of the vorticity equation. According to their consideration, the flow redirection from streamwise to spanwise would generate $\partial w/\partial x$, and the secondary flow inside the turbulent region must be maintained in the strong interaction between streamwise and wall-normal vortexes through the flow redirection. Seki and Matsubara (2012) showed the large-scale structure forming about a turbulent patch and stripe pattern in the plane channel flow. They inferred that, as a result of an upstream laminar flow hitting the decelerating turbulent patch with high skin friction, a high-pressure region was produced at the laminar-turbulent interface and the high pressure made the upstream laminar flow slow down. Because of the continuity of the flow, this decelerating flow should turn to the spanwise direction, resulting in a spanwise secondary flow around the downstream interface of the turbulent patch. Our explanation of the mechanism of stripe pattern is similar to theirs (Seki and Matsubara, 2012). Recently, Duguet et al. (2013) suggested a mechanism to explain the obliqueness of stripe pattern in the plane Couette flow. They indicated that a forming stripe pattern should be seen as a growing turbulent spot made of streaks of finite streamwise extent. The local orientation of y -dependent advection velocity would determine the direction in which the turbulent patch elongates and creates new streaks.

Figures 5.7 show each component of the velocity fluctuations at two different rotation numbers. It is clearly observed in (a) in the figures that streamwise streaky structures are

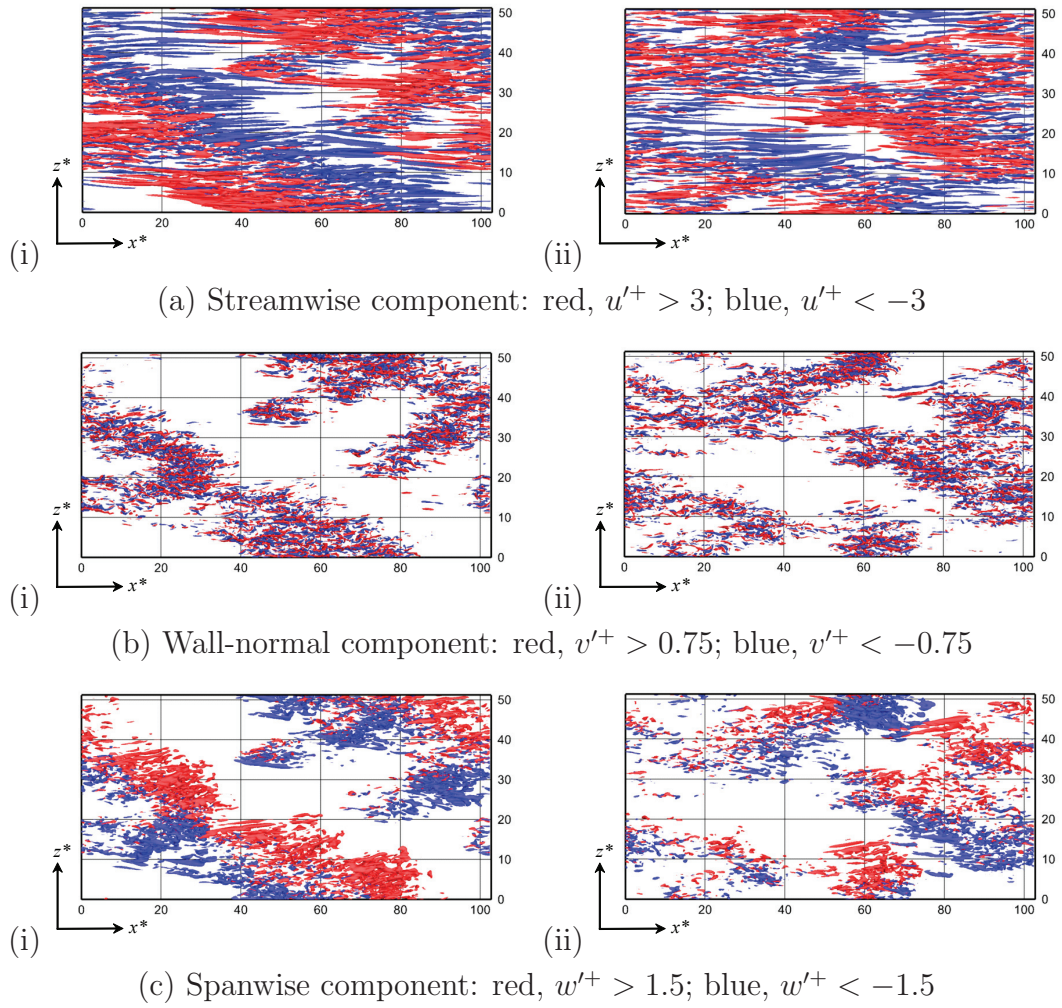


Fig. 5.7 Three-dimensional visualization of an instantaneous flow field at $Ro_\tau =$ (i) 0.015 and (ii) 0.03, viewed from the wall-normal direction: (a) u' , (b) v' , and (c) w' . The mean flow moves from left to right.

not evenly distributed and seem to form bands or clusters. According to the distributions of the wall-normal velocity fluctuation (v'^+), one can clearly observe spatially-localized turbulence. The intermittent stripe pattern can be determined in Fig. 5.7(b-i), and stripe pattern contains two-way inclination with respect to the streamwise direction. In the figure, one of the oblique bands is relatively thick and elongated in the same direction as that observed in Fig. 5.6, i.e., the direction with about -26° against the x axis. In addition, two finite bands elongated in a different direction to $+26^\circ$ are observed in Fig. 5.7(b-i). It may be interesting to note that the rather short interval between these finite bands is equivalent to the stripe pattern neutral wavelengths in the static system, while the intervals of the thicker bands are twice the size of the neutral wavelengths. This implies that the flow field at $Ro_\tau = 0.015$ (given in Fig. 5.7 (i)) is a transitional state, in which stripe pattern occurs with a mixture of the neutral wavelength and a widened wavelength due to the system rotation. This widening of the stripe pattern wavelength will be discussed

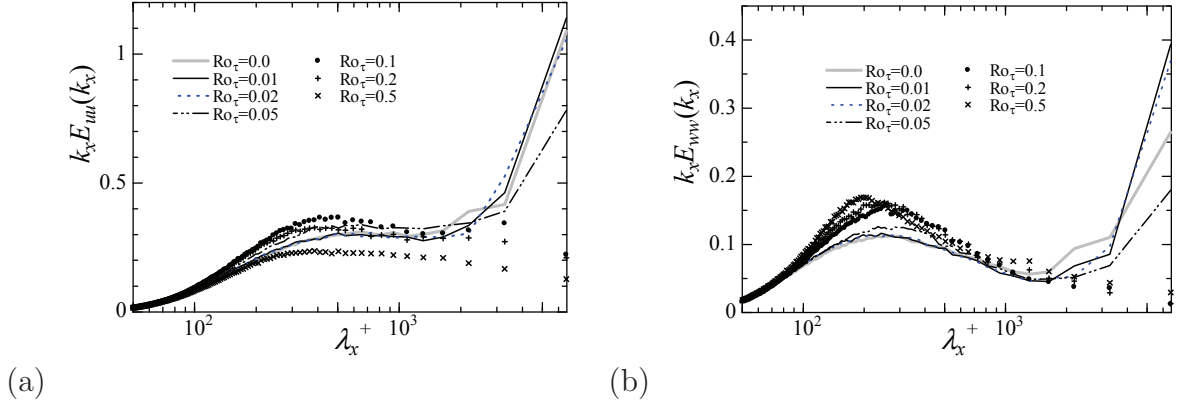


Fig. 5.8 Pre-multiplied energy spectra for (a) u' and (b) w' , as a function of streamwise wavelength λ_x ($= 2\pi/k_x$) at $y^+ = 63$ ($y \approx \delta$).

further with energy spectra later.

As for the spanwise velocity fluctuation, somewhat coherent structures are clearly seen to emerge around the turbulent regions, as shown in Fig. 5.7(c-i). In common with the streamwise component u' , either a positive or negative fluctuation of w' dominantly appears in the upstream area of the turbulent region, while w' with the opposite sign dominates the downstream area. This phenomenon is the spanwise secondary flow of interest.

As seen in Fig. 5.7 (ii) ($Re_\tau = 0.03$), the regular pattern of stripe pattern becomes unstable with increasing Ro_τ . The streamwise streaky structure is much elongated longitudinally. This transformation is attributed to the onset of roll cells in a moderate rotation. The turbulent region is scattered about the horizontal direction, then the streaks around the turbulent region gather and grow in clusters. Around a fragment of stripe pattern, the spanwise secondary flow still exists along the turbulent region.

In order to estimate the effect of the rotation on the structure of stripe pattern quantitatively, the streamwise and spanwise pre-multiplied energy spectra are shown in Figs. 5.8 (a) and (b). Their spectra at the channel center are presented in the form of $k_i E_{uu}(k_i)$ versus $\log \lambda_i^+$, where k_i is the wave number, on the basis of the formula:

$$\int_0^\infty k_x E_{uu}(k_x) d \log k_x = \int_0^\infty k_z E_{uu}(k_z) d \log k_z = \overline{u'u'}. \quad (5.3)$$

In this plot, a peak wavelength is named as ‘Most Energetic Wavelength’ (MEW) and represents the size of the most dominant structure. In distributions of $k_x E_{uu}$, $k_x E_{ww}$, and $k_z E_{ww}$, MEW appear at $\lambda_x^+ = 6500$ and $\lambda_z^+ = 3300$, which correspond to the streamwise and spanwise sizes of stripe pattern. Under the system rotation ($Ro_\tau = 0.01, 0.02$), those MEW exhibit higher peaks than those in the static system ($Ro_\tau = 0$). This augmentation of MEW represents the increase in the contained energy of stripe pattern. Another peak in short wavelengths, which is relevant to inherent fine-scale structures of wall turbulence, is almost unchanged for $Ro_\tau \leq 0.05$. It is well known that the spanwise spacing of the near-wall streaky structure is $\lambda_z^+ = 100$ and that of the large-scale structure of turbulence

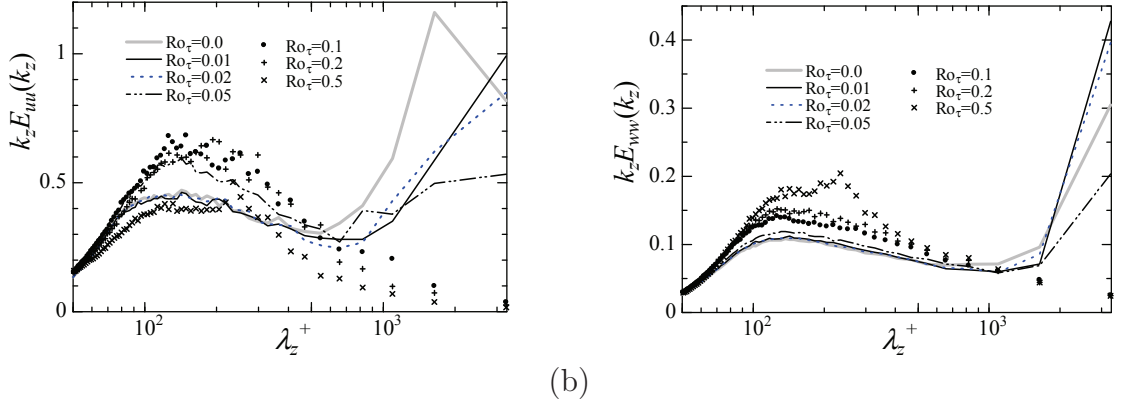


Fig. 5.9 Pre-multiplied energy spectra of (a) u' and (b) w' , as a function of spanwise wavelength λ_z ($= 2\pi/k_z$) at $y^+ = 63$ ($y \approx \delta$).

is $\lambda_z^* = (\lambda_z/\delta) \approx 1.3\text{--}1.6$ (Abe et al., 2004). These inner and outer structures in wall turbulence would be measured well by the viscous length scale ν/u_τ and the outer scale δ , respectively. For low Reynolds numbers, however, the difference in size between the near-wall structure and the large-scale structure should be small. Therefore, it is difficult to determine whether the wavelength ($\lambda_z^+ = 150$) of the MEW in the short wavelength regime is caused by the near-wall streaks or the large-scale structure. The other MEW of interest can be found in the long wavelength regime. As for $k_z E_{uu}$, MEW of $\lambda_z^+ = 1600$ at $Ro_\tau = 0.0$ moves to the longer wavelength of $\lambda_z^+ = 3300$ in the rotating system. This shift of MEW may prove that the spatial quasi-laminar region becomes wider in the spanwise direction. (It should be noted that the inclination angle of stripe pattern with respect to the streamwise direction does not change from $\pm 26^\circ$, as given in Figs. 5.6 and 5.7 (i), whereas MEW becomes a longer wavelength.) According to these results, at the very low Ro_τ , stripe pattern contains more energy compared to the static case ($Ro_\tau = 0$), whereas the quasi-laminar region becomes wider. The augmentation of spanwise turbulent energy is also directly related to that of the spanwise secondary flow.

The above-mentioned widening of the stripe pattern wavelength may be interpreted as due to competition among different modes. Rolland and Manneville (2011) explained the orientation of stripe pattern in the plane Couette flow by decomposing several modes $\mathbf{m} = (m_x, m_z) = (k_x L_x/2\pi, k_z L_z/2\pi)$. To quote their discussion, the thicker and thinner bands do not have the same wavelength: the averaged wavelengths are results of competition between $(1, \pm 1)$ and $(2, \pm 2)$. The present results show that the low wave-number mode of $(1, \pm 1)$ becomes dominant as $Ro_\tau = 0 \rightarrow 0.02$, and then the size of stripe pattern is expanded by very low rotation. However, it should be noted that the exact wavelength and angle of stripe pattern under a negligibly small effect of the periodic boundary cannot be determined by the present DNS. Although the spatial size of structures (stripe pattern and roll cells) relies more-or-less on the computational domain, the alternation of the stripe pattern dominant mode (in the competition between $(1, \pm 1)$ and $(2, \pm 2)$ by the rotation)

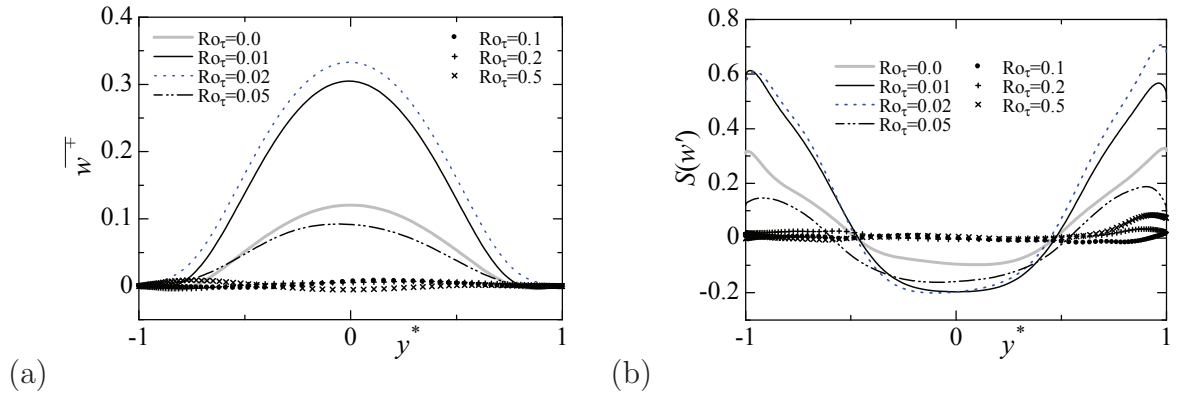


Fig. 5.10 (a) Mean spanwise velocity profiles and (b) skewness factor of w' for various rotation numbers.

is a result of interest.

For Ro_τ higher than 0.05, we observe no footprint of stripe pattern in the visualized flow and also no spike in long wavelengths of the pre-multiplied energy spectra, as shown in Figs. 5.8 (a) and (b). Instead of stripe pattern, other spikes relating to roll cells are displayed in $\lambda_z^+ = 128-256$ (corresponding to $2-4\delta$) at $Ro_\tau = 0.5$: see Figs. 5.8 (b). Iida et al. (2010) also indicated the disappearance of stripe pattern when a moderate system rotation was imposed. The disappearance of stripe pattern can be detected also from the spanwise-velocity statistics, to be given later.

5.2.2 Spanwise secondary flow

In this section, we present several statistics related to the spanwise velocity component, which characterizes stripe pattern, and discuss the augmentation/diminution of stripe pattern.

Figure 5.10 (a) shows the mean spanwise velocity profile, $\overline{w^+}$. It is known that this averaged value should be zero in the turbulent or the laminar channel flow. $\overline{w^+}$ is about zero in high- Ro_τ , because of the dominance of roll cells without stripe pattern. However, in the flow accompanied by stripe pattern (for $Ro_\tau \leq 0.05$), $\overline{w^+}$ has significant magnitude, because of the asymmetricity of the spanwise secondary flow along each inclined turbulent band of stripe pattern. The spanwise secondary flow is induced by the impingement of the quasi-laminar and turbulent regions. The impingement causes a flow redirection from the streamwise to the spanwise direction, and then stripe pattern has spanwise velocity fluctuation of strong magnitude and asymmetricity. Hence, the asymmetric feature of the spanwise velocity component would dissolve when stripe pattern disappeared. As seen in Fig 5.10 (a), $Ro_\tau = 0$ reveals a non-zero value of $\overline{w^+}$ throughout the channel because of the occurrence of stripe pattern. It is interesting to note that, at $Ro_\tau = 0.01$ and 0.02, $\overline{w^+}$ significantly increases compared to the non-rotating case. Under the spanwise system

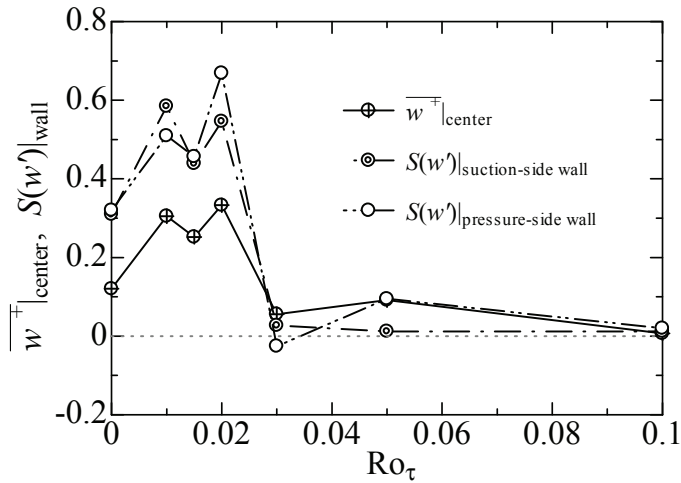


Fig. 5.11 Variation of statistical values corresponding to the magnitude of spanwise secondary flow as a function of the rotation number.

rotation, the Coriolis instability would not directly affect the spanwise velocity component.

Figure 5.10 (b) shows the skewness factor $S(w') \equiv \overline{w'^3}/w'_{rms}{}^3$, where w'_{rms} represents the root-mean-square (RMS) value of w' .

The skewness factor of w' is a measure of the asymmetric distribution of w' . Similar to \overline{w} , $S(w')$ should be zero in the channel flow, according to the reflection symmetry of the solutions of the fundamental equations. It should be noted that the selection of either a positive or negative value of $S(w')$ would depend on the inclination direction of stripe pattern. If the inclination is inverse against our obtained flow field, $S(w')$ would show opposite signs. In Fig. 5.10 (b), $S(w')$ deviates from the normal distribution ($S(w') = 0$) and it has significant magnitudes near the wall and at the channel center in the case accompanied by stripe pattern. This indicates intermittently-intensified fluctuations along with the asymmetry. It is interesting to note that, for $Ro_{\tau} \leq 0.02$, the non-zero $S(w')$ is significantly enhanced compared to that at $Ro_{\tau} = 0$.

The maximum of $\overline{w^+}$ and $S(w')$ appear at the channel center and in the vicinity of the wall, respectively. Figure 5.11 shows the Ro_{τ} -dependency of these maxima of $\overline{w^+}$ and $S(w')$. As for $S(w')|_{max}$, two values are determined on the pressure and suction sides. It is obvious that these values are increased by the system rotation and achieve a peak around $Ro_{\tau} = 0.01$ – 0.02 . Although there is non-monotonicity at $Ro_{\tau} = 0.015$, this is probably a trivial issue. To obtain a more precise curve, it would be necessary to perform a simulation with longer period of time averaging and a much larger computational domain. However, at least, it can be concluded that a very low system rotation enhances the characteristic flow of stripe pattern. Although both $\overline{w^+}|_{rms}$ and $S(w')|_{rms}$ decrease significantly at $Ro_{\tau} = 0.03$ – 0.05 , the footprint of stripe pattern still remains. As Ro_{τ} is larger than 0.1, both $\overline{w^+}$ and $S(w')$ become zero and stripe pattern disappears.

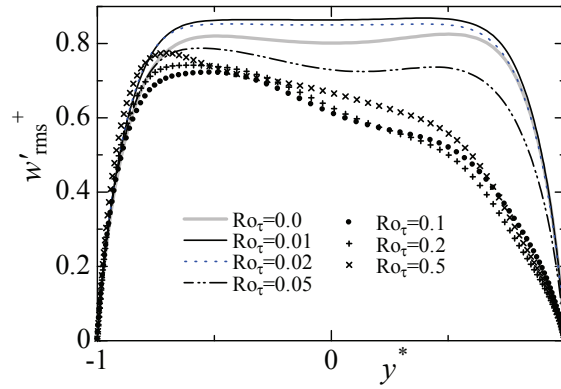
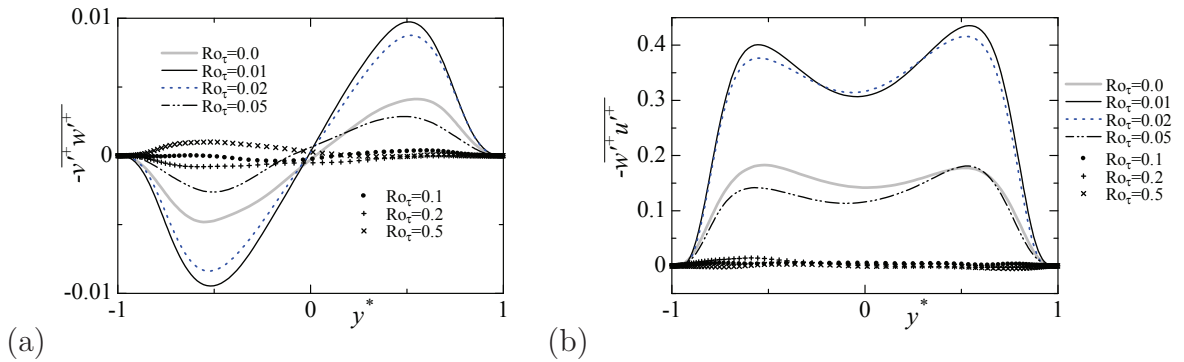


Fig. 5.12 Root-mean-square of the spanwise velocity fluctuation.

Fig. 5.13 Wall-normal profiles of the Reynolds shear stress of (a) $-\overline{v'^+w'^+}$ and (b) $-\overline{w'^+u'^+}$.

The discussion only of the spanwise mean velocity would not necessarily give adequate support to the augmentation of the spanwise secondary flow, because the spatial average neglects the variation in the streamwise position. However, the augmentation of the spanwise secondary flow is determined by RMS of the spanwise velocity fluctuation. The spanwise turbulence intensity (RMS of the spanwise velocity fluctuation) is shown in Fig. 5.12.

The very low rotation numbers, at which the secondary flow is enhanced, are observed to induce an increase in w'_{rms} throughout the channel. On the other hand, w'_{rms} monotonically decreases, especially on the suction side with increasing Ro_τ (for $\text{Ro}_\tau \geq 0.03$).

The Reynolds shear stresses of $-\overline{v'^+w'^+}$ and $-\overline{w'^+u'^+}$ for different Ro_τ levels are given in Figs. 5.13 (a) and (b). Generally, in unidirectional flows such as the present flow configuration, those mean components should be zero in turbulence and laminar flow. With the occurrence of stripe pattern, they become non-negligible values. Only at $\text{Ro}_\tau = 0.01$ and 0.02 , are those magnitudes higher than that at $\text{Ro}_\tau = 0$. Under the spanwise system rotation, the Coriolis instability would not affect directly the spanwise velocity component, but would give rise to the longitudinal vortices (of roll cells) on the pressure side. The enhancement of the shear stresses including w' occurs in the whole channel (irrespective of the pressure and suction side). This implies the augmentation of the stripe pattern structure,

which is practically uniform in the wall-normal direction from the viewpoint flow state.

Finally, we discuss the high rotation number regime. As Ro_τ increases, the peak values of several statistics relating to \bar{w} and w' decrease: see Figs. 5.10, 5.12, and 5.13. This reduction is caused by the development of roll cells and the diminution of stripe pattern. The structure of roll cells consists of large-scale longitudinal vortices and causes variation of the wall-normal velocity component. In contrast, stripe pattern does not contain an intensive wall-normal velocity component. The wall-normal turbulence intensity increases in contrast to the spanwise component, with the development of roll cells and the stripe pattern disappearance occurring in the background.

5.3 Summary

The alternations of large-scale structures in the rotating channel flow with emphasis on the turbulent stripe and roll cells are investigated to illuminate robustness of laminar-turbulent pattern to rotation.

The stripe pattern is a localized equilibrium turbulence that can be observed in the transitional Reynolds-number regime. The roll cell is the array of longitudinal vortexes caused by the Coriolis instability, and exerts several significant variations in the momentum transfer. The transitional channel flow subject to relatively weak spanwise system rotation involves these two large-scale structures with the turbulent background. Alternations of large-scale structures occur as a function of the friction rotation number: (i) the occurrence of turbulent stripe is limited only to very low Ro_τ (≤ 0.02), (ii) the intermediate region between (i) and (iii) shows the coexistence of turbulent stripe and roll cells, and (iii) only roll cells is dominant at $Ro_\tau \geq 0.2$. The Reynolds number dependency with respect to these threshold Ro_τ values is not particularly noticeable.

Because of the relaminarization and disappearance of stripe pattern, the contribution of turbulence to the wall shear stress on the suction side becomes minimum at $Ro_\tau = 0.02$, which is not a high enough value to activate roll cells. As a result, a net drag reduction can be achieved in this condition, although it is very small. Once the pressure-side flow is dominated by roll cells, the net drag is increased (i.e., the flow rate decreases) with increasing Ro_τ , similar to the results for high Reynolds numbers. The asymmetric character of turbulent stripe is enhanced at very low Ro_τ ($= 0.01$) by the Coriolis effect, although its mechanism is still unclear. The disappearance of turbulent stripe and the development of roll cells are caused by the intense wall-normal component of the velocity fluctuation, which is related to the direct Coriolis effect.

In addition, the effects of spanwise system rotation on the structure of the turbulent stripe pattern is evaluated. The stripe pattern occurs only in flows with weak or no spanwise system rotation in both the pressure and suction sides, as discussed above. The very low rotation (Ro_τ as low as 0.01–0.02) enhances the structure of stripe pattern. In the very

low Ro_τ , the wavelength corresponding to stripe pattern contains more energy than in the static system, whereas the quasi-laminar region is wider. A spanwise secondary flow occurs along each turbulent band of stripe pattern. In addition, the spanwise velocity component relevant to the secondary flow is enhanced by weak rotation with the occurrence of stripe pattern on both the pressure and suction sides. When Ro_τ is further increased to the level of the roll cells occurrence, \bar{w} and the Reynolds shear stresses including w' decrease as a result of the disappearance of stripe pattern.

The flow map reported herein offers many opportunities and benefits to study the effect of rotation on transition and turbulence in shear flows, allowing us to find the parameter range where a specific flow state occurs. The occurrence of stripe pattern and its augmentation by system rotation are important phenomena from the viewpoint of mass and scalar transport in the spanwise direction, because the spanwise velocity component has a distinguished value. The present study successfully demonstrated that the system rotation, even with very low Ro_τ , gives rise to non-zero mean spanwise velocity. This may be favorable for engineering applications that require the efficient mass/scalar transfer even at transitional Reynolds-number flows.

6

Discussion

We comprehensively discuss the universality of laminar-turbulent patterning to the annular geometry of Poiseuille flows and the robustness of the patterning to roughness and rotation by scrutinizing the sustaining process of the patterning in this section.

As discussed in previous sections of the investigation, a large-scale intermittent structure (laminar-turbulent pattern) consisting of laminar and turbulent regions spatially occurs in alternate shifts at transitional Reynolds number. Well known specific size of the turbulent structure is introduced by Jimenez and Moin (1991) and scaled by the inner unit (u_τ/ν). The mean streak spacing zu_τ/ν of streaks and the streamwise length xu_τ/ν of vortices near a wall is approximately 100 and 250–350, respectively. The internal structure of the laminar-turbulent pattern is also scaled by the specific size of turbulent structures that are streaks and vortices corresponding to a small-scale structure. In contrast, streamwise and spanwise (azimuthal) lengths of laminar-turbulent pattern are characterized by very large-scale rather than small-scale structures. The laminar-turbulent pattern is mostly classified into a streamwise localized structure such as puff in pipe flow and the stripe pattern in planar channel flows. Whereas the puff is a spatially one-dimensional structure, the stripe pattern is a two-dimensional structure accompanied with spanwise secondary flow with an oblique interface. These large-scale structures are scaled by the outer unit and the streamwise length of the puff is about 20 pipe diameter (Eckhard et al., 2007). In the planar channel flows, the streamwise and spanwise lengths of stripe pattern are approximately 30 and 15 channel width, respectively (Duguet et al., 2010 and Tsukahara et al., 2010b). Therefore, we were able to divide instantaneous velocity into large-scale flow ($U_i = \mathcal{L}u_i$) and small-scale flow ($\tilde{u}_i = \mathcal{H}u_i$) because the specific size of small and large-scale structures is obviously different. For scale separation, \mathcal{L} and \mathcal{H} as low- and high-pass filters, respectively, are considered as described in previous sections. The clear scale separation between large and small scales is a key assumption when analyzing the sustaining mechanism of the laminar-turbulent pattern which we will describe below.

Firstly, we re-introduce the streamwise velocity distribution along the streamwise direction in the case of the laminar-turbulent pattern. As seen in Fig. 6.1, streamwise velocity in

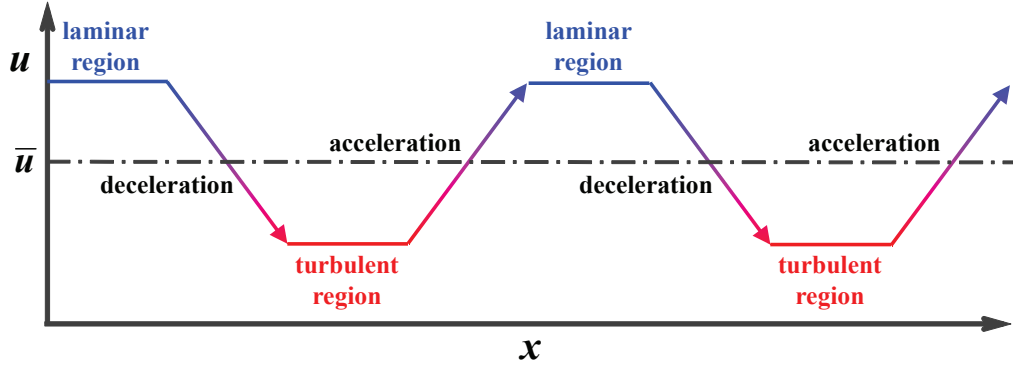


Fig. 6.1 Streamwise velocity in the streamwise direction of the laminar-turbulent pattern.

the laminar region is higher compared to that in the turbulent region because a small-scale structure densely occurs in the turbulent region. Therefore, a velocity difference along the laminar-turbulent interface occurs and the laminar region impinges on the turbulent region. Then, the streamwise velocity decreases rapidly at the interface. In addition, the streamwise velocity increases towards the laminar region along the interface in the downstream area of the turbulent region.

The continuity equation for a large-scale flow in Cartesian and cylindrical coordinates is as follows.

$$\frac{\partial U_x}{\partial x} + \frac{\partial U_y}{\partial y} + \frac{\partial U_z}{\partial z} = 0 \quad (6.1)$$

$$\frac{\partial U_x}{\partial x} + \frac{1}{r} \frac{\partial r U_r}{\partial r} + \frac{1}{r} \frac{\partial U_\theta}{\partial \theta} = 0 \quad (6.2)$$

$\partial U_x / \partial x$ caused by the mismatch of streamwise flow rates at the interface should balance with $\partial U_y / \partial y + \partial U_z / \partial z$ or $1/r(\partial r U_r / \partial r + \partial U_\theta / \partial \theta)$. When we consider laminar-turbulent patterning with obliqueness, because the pattern is almost spatially homogeneous in the wall-normal direction, the continuity equation for a large scale flow is integrated in the wall-normal direction and we obtain the following equation.

$$\int_0^d \frac{\partial U_x}{\partial x} dy + \int_0^d \frac{\partial U_y}{\partial y} dy + \int_0^d \frac{\partial U_z}{\partial z} dy = 0 \quad (6.3)$$

$$\int_{r_i}^{r_o} \frac{\partial U_x}{\partial x} dr + \int_{r_i}^{r_o} \frac{1}{r} \frac{\partial r U_r}{\partial r} dr + \int_{r_i}^{r_o} \frac{1}{r} \frac{\partial U_\theta}{\partial \theta} dr = 0 \quad (6.4)$$

Here, wall-normal-integration makes the term $\int_0^d \partial U_y / \partial y dy$ and $\int_{r_i}^{r_o} 1/r(\partial r U_r / \partial r) dr$ vanish because of the zero relative flux across the two walls and the following equations are obtained.

$$\int_0^d \frac{\partial U_x}{\partial x} dy + \int_0^d \frac{\partial U_z}{\partial z} dy = 0 \quad (6.5)$$

$$\int_{r_i}^{r_o} \frac{\partial U_x}{\partial x} dr + \int_{r_i}^{r_o} \frac{1}{r} \frac{\partial U_\theta}{\partial \theta} dr = 0 \quad (6.6)$$

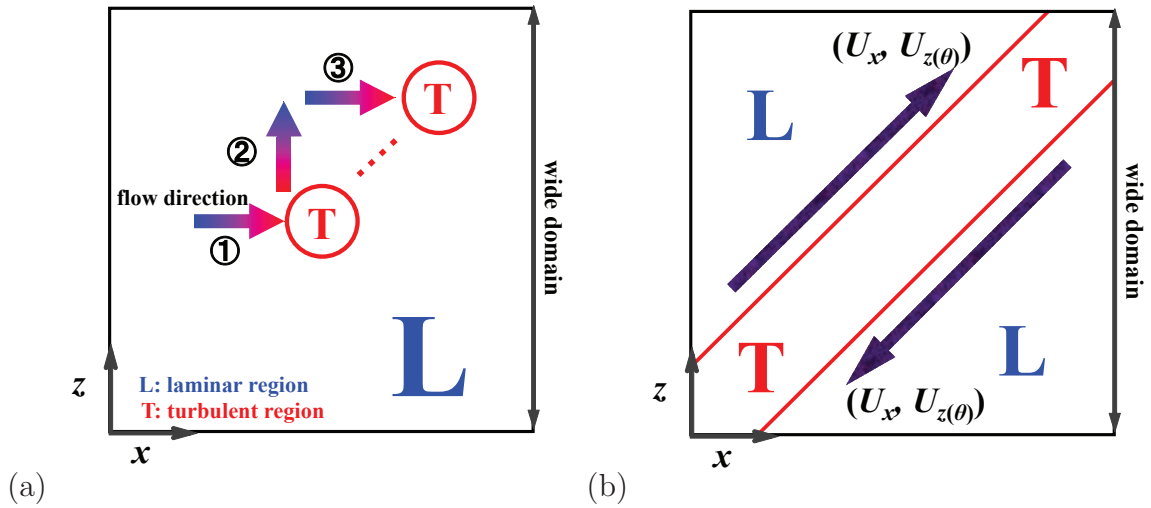


Fig. 6.2 Conceptual diagram of oblique formation of the pattern.

If the spanwise length of the domain is sufficiently long (Fig. 6.2(a)), the laminar flow impinges upon the turbulent region ① and the spanwise redirection of the flow occurs at the interface ② to satisfy the wall-normal integrated conservation law (Eq. 6.6). Then, the redirected flow is advected in the streamwise direction by the laminar flow again and impinges upon the turbulent region ③. These sequences continuously occur and finally a laminar-turbulent pattern with obliqueness associated with large-scale flow $(U_x, U_{z(\theta)})$ is sustained as shown in Fig. 6.2(b).

As for the aPf for high η , the azimuthal spacing (L_z) where the large-scale flow can proceed is large. Therefore scale separation of small- and large-scale flow is workable. A non-zero peak of the probability of an azimuthal large scale flow is observed as shown in Figs. 3.24 and 3.25. Therefore, helical turbulence emerges by the same sustaining mechanism of laminar-turbulent patterning with obliqueness in the pPf as discussed above. However, in the aPf for small η , spanwise length is insufficient to maintain a spanwise large-scale flow (Fig. 6.3(a)) and applying the scale separation between small- and large-scale flows is difficult because the scale difference of small- and large-scale flow decreases. In practice, if a spanwise large-scale flow is obtained by using a low-pass filter selecting all spanwise wavelengths smaller than $2d$ that corresponds the mean streak spacing as a small-scale flow, the probability of a spanwise large-scale flow is mostly zero, as shown in Fig. 3.24 and 3.25. This proves that there is no spanwise large-scale flow and the scale of spanwise flow is smaller than $2d$. Therefore, the flow could be redirected both into wall-normal and spanwise directions (Fig. 6.3② of (a) and (b)) because the scale order of the spanwise flow becomes similar to that of the wall-normal flow ($L_z \approx d$). Because of the redirection process, a large-scale flow with spanwise secondary flow cannot be formed and a straight puff as a one-dimensional structure or as a streamwise localized structure is constructed and sustained. As described above, because of the attenuation of the azimuthal large-scale flow, helical turbulence changes straight puff with decreasing η through the helical

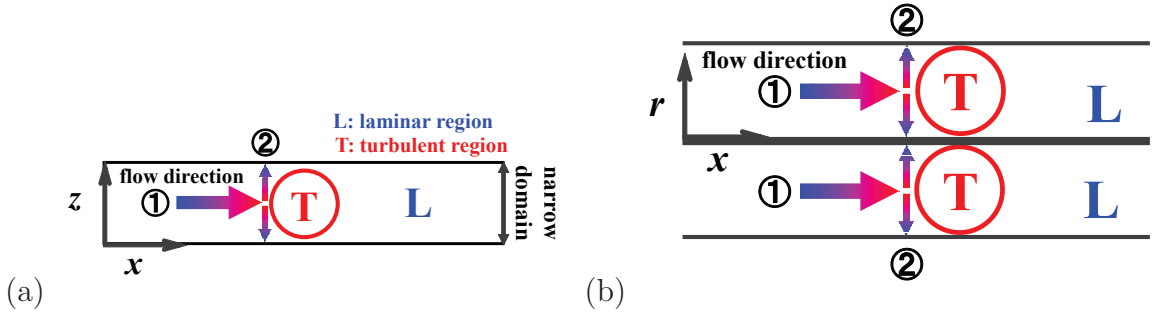


Fig. 6.3 Formation of secondary flow of the laminar-turbulent pattern without obliqueness in the aPf.

puff. Although a spanwise large-scale flow is not enough to maintain the obliqueness of the pattern, a spanwise large-scale flow cannot be ignored in contrast to that in a straight puff. Therefore, the equilibrium helical puff is not a stable state and is rarely observed because it should have two different features of stable patterns, such as helical turbulence and a straight puff.

So far, radius ratio dependency of laminar-turbulent patterning of the aPf has been examined. However, the formation of the pattern also depends on the Reynolds number. For high η , helical turbulence is localized in the streamwise direction and a helical puff is formed around Re_g in the narrow Reynolds number range. This alternation is caused by the scale transition and the SSP of the small scale structures. As described above, mean spanwise spacing of streaks is scaled by the inner unit and approximately $zu_\tau/\nu = 100$. When the specific scale is converted from inner (zu_τ/ν) to the outer scale ($2z/d = (zu_\tau/\nu)/Re_\tau$), the mean spanwise spacing of streaks scaled by the outer unit increases with decreasing Re_τ . Therefore, the maximum spanwise spacing (L_z) of annular geometry by the viewpoint of a small-scale flow narrows with a decrease in Re_τ and the boundary between small- and large-scale flows becomes unclear compared to moderate Re_τ in the transition regime. These allow the change of laminar-turbulent patterning with the same process depending on η ; helical turbulence cannot be maintained and changes the helical puff. However, the Reynolds number range for the occurrence of a helical puff becomes narrower around Re_g with increasing Re_τ . Moreover, for intermediate η , a complex transition process with decreasing Re_τ is observed and the transitional structure is varied, including helical turbulence, the helical puff, and the straight puff following the Re_τ dependency process. The other approach to explain the laminar-turbulent patterning with Re_τ is the SSP suggested by Waleffe (1997) that describes the sustenance mechanism of streaks and streamwise vorticity. As seen in Fig. 6.4, the streamwise vorticity advects streamwise velocity to create streaks. These streaks then undergo an inflectional instability and generate three-dimensional vorticity by the nonlinear self-interaction. When the Reynolds number is high enough, the feedback process of nonlinear interaction is enhanced and this prevents the original streamwise vorticity from decaying, which sustains the streaky motion. At

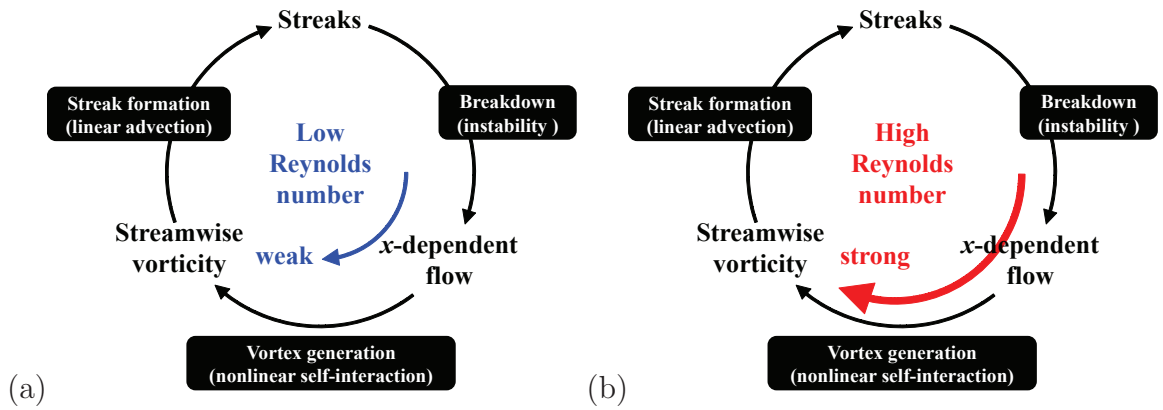


Fig. 6.4 Self-sustaining-process for (a) low and (b) high Reynolds number.

high Reynolds number, the contribution of streak instability to the vorticity is too weak to prevent it from eventually decaying at low Reynolds number around Re_g . Therefore, a small-scale structure around Re_g cannot be activated and preserve a certain amount of the turbulent region whereas turbulence can be enhanced at a high Reynolds number. Then, even for high η , the helical puff is sustained with a sequence of expansion and diminution, and the helical puff cannot be developed into helical turbulence at low Re_τ . This sequence is also observed in the case of the straight puff with fixed streamwise length in the cPf and the aPf with low η . As discussed above, the shape of the laminar-turbulent pattern changes, depending both on Re_τ and η by the combination of large and small-scale flow motions and the space scale of the flow.

As discussed above, the present results have confirmed that the aPf, parametrised by both its radius ratio η and Re_τ , is a relevant candidate to track the transition from puffs to oblique stripes. The main physical mechanism responsible for this transition is the relaxation of the azimuthal confinement (measured in units of the gap d) as η increases, allowing for more freedom in the orientation of the large-scale flow occurring at the laminar-turbulent interfaces, should they exist. Beyond a critical azimuthal extent, a neater selection of the orientation occurs ruled by the mass conservation at the interfaces. As η increases from 0 to 1, the following turbulent regimes are encountered :

- spatio-temporal intermittency as in cPf for $0 < \eta \lesssim 0.2$
- mixed distribution of straight and helical puffs for $0.2 \lesssim \eta \lesssim 0.4$
- regular patterns of oblique stripes, so-called helical turbulence in the aPf for $\eta \gtrsim 0.5$
- disordered patterns of oblique stripes for $0.5 \ll \eta \lesssim 1$.

The last item has not been verified here but is expected to match all observations in extended planar shear flows (with weak additional effects due to the wall curvature). The parameter space may also contain new regimes so far unexplored. A statistical analysis has been carried out by focusing entirely on the local structure and orientation of the large-scale

flow. When the two regimes of interest are characterised by a symmetry breaking (as is the case here where each oblique stripe violates the $\overline{U_\theta} = 0$ symmetry), other order parameters can be considered (see e.g. Cortet et al., 2010). In the spirit of pattern formation, the statistics of some well-chosen spectral coefficients characteristic of the structures under study can be helpful.

While an experimental verification of such flow regimes is called for, it is instructive to discuss whether other shear flow geometries lend themselves easily to bifurcations between intermittently turbulent regimes. The transition from puffs to stripes corresponds essentially, as previously shown, to a transition from one-dimensional to two-dimensional intermittency, via the occurrence of quasi-one-dimensional stripe patterns. Other homotopies can be suggested by similarly tuning the confinement in the direction transverse to the mean flow. Imposing confinement by sidewalls in an otherwise Cartesian geometry is a possible option. A rectangular duct flow driven by a pressure gradient, with a cross-section of dimensions $L_y \times L_z$, can be parametrised both by a Reynolds number and an aspect ratio $A = L_z/L_y$ ($A \geq 1$ by convention). $A=1$ corresponds to a square duct whereas $A \rightarrow \infty$ is equivalent to plane Poiseuille flow. The laminar profile is known to be linearly stable for all values of Re of interest here. This parametric problem has been considered numerically in Takeishi et al. (2015). Again straight puffs have been identified for $A \leq 3$ whereas spots with somewhat oblique interfaces have been visualized for $A \geq 4$. The authors yet report a peculiarity of the confinement by solid side-walls: permanent local relaminarisation at the side walls affecting the localisation of the turbulent structure. This is consistent with the recent experimental observations of spots in a duct flow with aspect ratio $A = 7.5$ (Lemoult et al., 2014). While this system has the advantage of dealing with flat walls only, the local relaminarisation at the sidewalls is interpreted as an additional complication obscuring the transition from puffs to oblique stripes.

Other examples closer to the present case of the aPf share a common geometry but differ in the way energy is injected into the flow. The Taylor-Couette system, where the two coaxial cylinders rotate with different frequencies Ω_i and Ω_o in the absence of axial pressure gradient, is such an example. It is known that for $\eta \rightarrow 1$, the case of exact counter-rotation $\mu = \Omega_o/\Omega_i = -1$ corresponds to plane Couette flow, which has a linearly stable base flow. It has been experimentally verified for η slightly below 1 that low- Re regimes with $\mu \approx -1$ feature two-dimensional intermittent arrangements of oblique stripes with both positive and negative angles (Prigent, 2002; Borrero, 2010; Avila et al., 2013). Reducing η with fixed μ , however leads to changes in the stability of the base flow. New regimes such as those featuring interpenetrating spirals (Andereck, 1986) enter the bifurcation diagram and make the continuation from stripes to puffs unlikely. It is an open question whether other paths in an enlarged parameter space could lead to such a transition.

Finally, an interesting candidate for the continuation from stripes to puffs is the sliding Couette flow (sCf), where the outer cylinder is fixed and the inner one moves axially with a constant velocity (see e.g. Deguchi and Nagata, 2011). This flow is thought to be equivalent

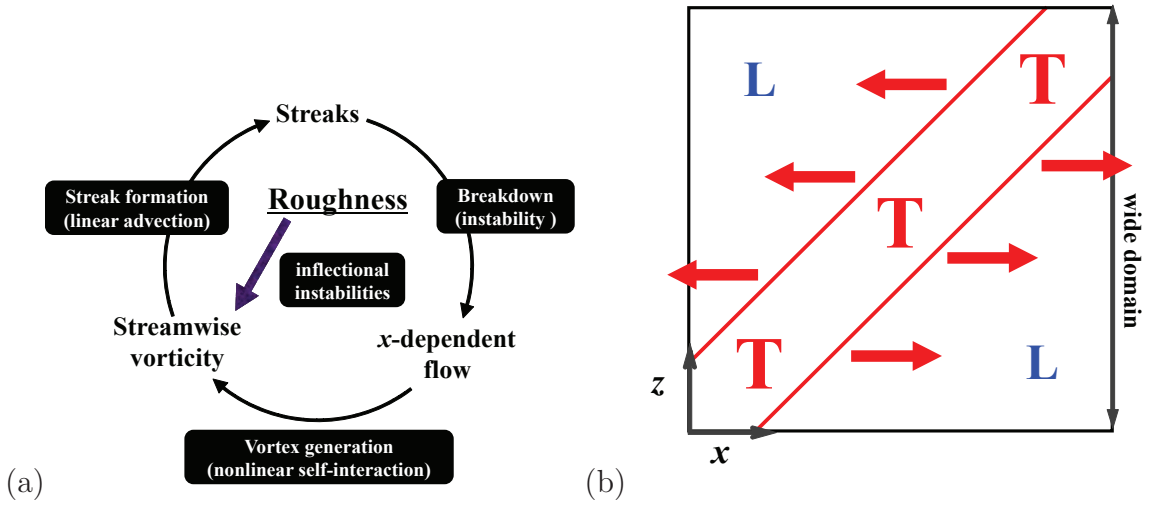


Fig. 6.5 (a) Self-sustaining-process influenced by roughness and (b) expansion of turbulent region of stripe pattern, effected by roughness.

to the pCf in the $\eta \rightarrow 1$ limit and again to pipe flow in the vanishing η limit. It has been verified numerically (Kunii et al., 2016) that this system bridges puffs to spots in a way apparently similar to the present system. Whether and how the homotopies in the sCf and the aPf really differ remains an open question. However, the aPf shows the important advantage of being easier to achieve experimentally as it does not include any motion of the solid walls, only a pressure gradient imposed on a fixed geometry.

Wall roughness affects the SSP of the small-scale flow whereas it does not directly affect the large-scale flow of the laminar-turbulent pattern. As seen in Fig. 6.5(a), wall roughness promotes the process of generating streamwise vorticities induced by the transverse vortices that are formed by the inflectional instability, acting as a vortex generator (Fig. 6.5(a)). Therefore, the turbulent region of the laminar-turbulent pattern expands and the flow becomes fully-turbulent with increasing roughness height. In the smooth case, a similar transition process from the laminar-turbulent pattern to fully-turbulence is observed with increasing Reynolds number. Nonlinear instability induced by high Reynolds number purely promotes the SSP without roughness. Although no laminar-turbulent pattern occurs below Re_g for smooth walls in the case of two rough walls, several modulated patterns emerge in the case of one rough wall. A dominant turbulent structure occurs in the region without roughness elements. Because the system is asymmetric, negligible ejection and sweep motion occurs in the region with and without roughness elements as shown in Fig 6.6 (a) and (b), respectively. Therefore, this yields a non-zero wall-normal components of the wall-normal averaged continuity equation in the roughness-free area as described by the following equation.

$$\int_{\eta(h)}^d \frac{\partial U_x}{\partial x} dy = - \left(\int_{\eta(h)}^d \frac{\partial U_y}{\partial y} dy + \int_{\eta(h)}^d \frac{\partial U_z}{\partial z} dy \right) \quad (6.7)$$

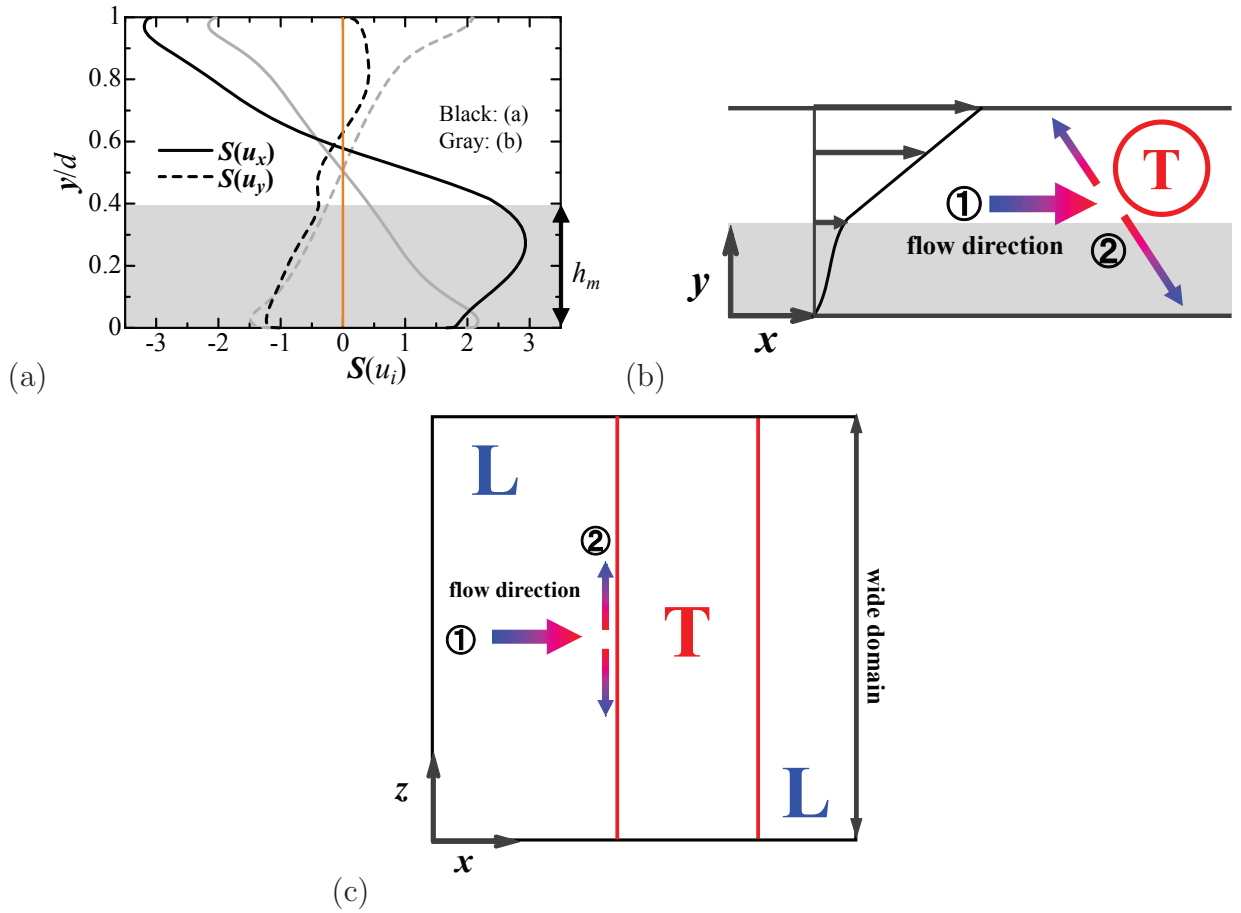


Fig. 6.6 (a)Skewness factor in the pCf with one rough wall $(Re_w, h/d) = (900, 0.2)$. (b)Schematic diagram of secondary flow along turbulent region of laminar-turbulent pattern without obliqueness in the pCf with roughness.

Then, $\int_{\eta(h)}^d \partial U_x / \partial x dy$ should be balanced with $\int_{\eta(h)}^d \partial U_y / \partial y dy + \int_{\eta(h)}^d \partial U_z / \partial z dy$ and the laminar-turbulent pattern without obliqueness is formed as shown in Fig 6.6 (c). The one-wall roughness affects the enhancement of $\partial U_y / \partial y$ in the roughness free-area and mass balance becomes $\int_{\eta(h)}^d \partial U_y / \partial y dy \approx \int_{\eta(h)}^d \partial U_z / \partial z dy$.

A spanwise system rotation also affects the mass balance of a large-scale flow. On the suction side, the flow is stabilized and relaminarizes with increasing rotation number. This leads to the disappearance of velocity fluctuations irrespective of small- and large-scale flow. On the pressure side, the rotation induces flow instability and forms a longitudinal vortex array called a roll cell (Fig 6.7). The roll cell is in the spanwise direction with regularity. The roll cell is almost homogeneous in the streamwise direction and causes $\partial U_x / \partial x = 0$. In contrast, intensive upward- and downward-motion occurs against the wall-normal direction (Fig 6.7(a)). In addition, a large-scale flow is balanced as $\partial U_y / \partial y + \partial U_z / \partial z = 0$ with the scale of half channel width because the roll cell is a large-scale pair vortex in alternate shifts (Fig 6.7(b, c)). Therefore, $\partial U_y / \partial y$ cannot be avoided and large-scale wall-normal motion affects not only the pressure side but also the suction side where the flow relaminarizes

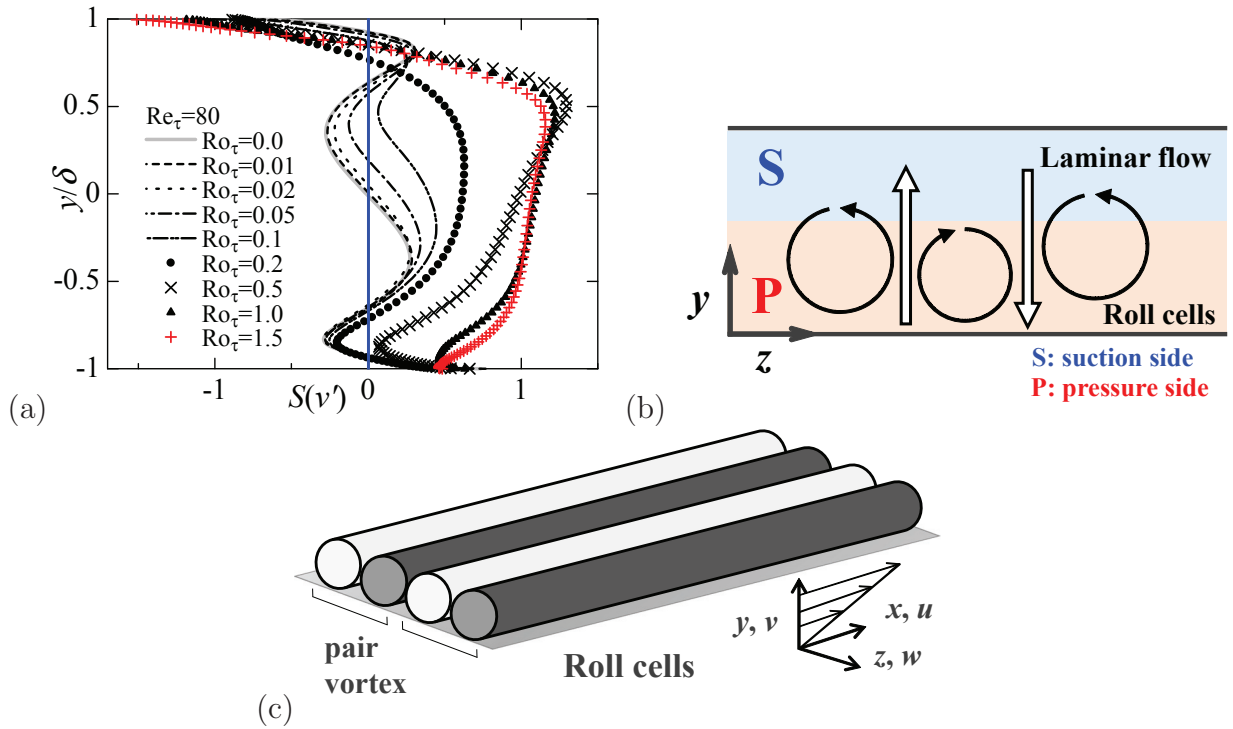


Fig. 6.7 (a) Skewness factor in the rotating pPf. (b, c) Schematic diagram of roll cells.

and laminar-turbulent pattern is collapsed. In the pCf with spanwise system rotation, the whole flow independent of the wall-normal position is stabilized or destabilized depending on the rotation direction. Tsukahara et al (2010a) describe the whole transition process in the pCf with spanwise system rotation. For stabilized rotation, the stripe pattern emerges in the wider and higher Reynolds number range compared to the Reynolds number range of the stripe pattern for the static case. In addition, the flow relaminarizes in the moderate Reynolds number range where the stripe pattern occurs in the static case. For destabilized rotation, various roll cells are observed and any intermittent structures does not occur. In a recent study, Brethouwer et al. (2011) consider the pPf with spanwise system rotation at very high Reynolds number ($Re_m = 10000$) and rotation number. They reveal the stripe pattern only occurs near the wall on the stabilized side and fully-turbulence without a roll cell is on the destabilized side. Therefore, the turbulent structures in the stabilized and destabilized regions are perfectly separated and there is no interaction at very high Reynolds and rotation numbers. These results also prove that wall-normal large-scale flow is the nuisance of the formation of stripe pattern consisting of streamwise and spanwise large-scale flow.

Clear separation of small- and large-scale flows and mass balance of large-scale flow are a key role to maintain a kind of laminar-turbulent pattern. Regardless of the pattern shape, the occurrence of the laminar-turbulent pattern causes a difference in the streamwise velocity between the laminar and turbulent region. This mismatch should balance with the

wall-normal and spanwise velocity components. If spanwise length is sufficiently large, the spanwise velocity component becomes large enough to ignore the wall-normal component and the oblique interface is constructed as a two-dimensional structure. However, when the spanwise length is not large or roughness/rotation affects the structure, wall-normal and spanwise components have relatively similar values and a laminar-turbulent pattern without an oblique interface is developed. Moreover, a strong wall-normal component makes the pattern collapse. As for small-scale motion, intensification of the SSP leads to the expansion of the turbulent region and the flow transitions to fully-turbulence.

7

Conclusion

The universality of laminar-turbulent patterning to the annular geometry of Poiseuille flows and the robustness of the patterning to roughness and rotation in plane channel flows are discussed in this thesis and we obtained the following conclusions.

The annular Poiseuille flow is firstly demonstrated to consider the universality of laminar-turbulent patterning depending on the flow system and we determine the possible connection between two different flow systems of cylindrical and plane Poiseuille flows. Most dominant laminar-turbulent pattern in the transitional regime of aPf changes from the straight puff to helical turbulence with increasing radius ratio. The straight puff and helical turbulence, obtained in the aPf, is similar to the equilibrium puff in the cPf and stripe pattern in the pPf, respectively. These transitional structures are connected by the newly obtained structure named the helical puff although the equilibrium steady helical puff is rarely observed. In addition, the dominant structure changes not only with radius ratio but also with Reynolds number. At large and small radius ratios, only the straight puff and helical turbulence dominated, respectively, in the transition regime. In contrast, there is competition among the straight puff, helical puff, and helical turbulence for intermediate radius ratios. These results prove that laminar-turbulent patterns emerges irrespective of the flow system of wall-bounded shear flows and laminar-turbulent patterns in different systems are smoothly connected by changing the shape with/without a spanwise secondary flow and by streamwise localization of the pattern. These new analyses suggest that all canonical flow systems, such as the Taylor-Couette flow, the plane Couette flow, and their combinations (e.g. the Couette-Poiseuille flow) should bridge each other.

The robustness of the laminar-turbulent pattern focusing on the stripe pattern is shown by considering the roughness and rotation effects.

The effects of roughness on the stripe pattern are investigated by adopting the roughness model. The stripe pattern is sustained until $h/d = 0.075$ and 0.05 in the pCf with one/two rough walls, respectively, at fixed $Re_w = 1300$ that is the lowest Re_w sustaining stripe

pattern in pCf without roughness. By adding roughness, especially at a high roughness height, lower critical Reynolds numbers sustaining turbulence are obtained compared to the smooth wall case. However, a stripe pattern is not obtained below $Re_g \approx 1300$ in the pCf with two rough walls. In contrast, stripe pattern emerges below Re_g in the pCf with one rough wall. These results indicate the stripe pattern is robust and can be sustained even with roughness. In addition, several characteristic structures are observed in pCf with one rough wall. At an extremely high roughness height of one rough wall, the occurrence of forced turbulence with coherent streaks and a strange laminar-turbulent pattern are found. That is to say, a laminar-turbulent pattern is obtained not only in the ideal case but also in actual situations when removing the roughness and obtaining a perfectly smooth wall is difficult. In addition, if artificially roughness is created, forced turbulence can be obtained.

As for more complicated cases, the pPf with spanwise system rotations is analyzed. The flow system is known to consist of unstable and stable side with respect to the wall-normal direction. Differing from the results of roughness, the parameter range of the occurrence of the stripe pattern is very narrow and the stripe pattern only can be sustained at very low rotation numbers ($Ro_\tau \leq 0.02$). Roll cells with strong vertical transport occur in the unstable side and roll cells influence not only the unstable side but also the stable side. Therefore, the stripe pattern with spanwise secondary flow is collapsed by the dominance of the roll cells that induce strong vertical transport. However, the pPf with very weak rotation enhances the spanwise secondary flow of the stripe pattern.

Finally, we summarize the conclusion. The mechanism of laminar-turbulent patterning is characterized by two different scales that are small- and large-scale flows, and it can be applied all wall-bounded shear flows in subcritical transition as universal phenomena of the turbulent transition. The small-scale flow as general turbulent motion described by a SSP is in the turbulent region of the pattern. High Reynolds number and roughness height (or density) promote the nonlinear process of generating vortices. The promotion expands the turbulent region of the pattern and transition from the pattern to fully-turbulence. The large-scale flow is sustained by the mass balance according to the large-scale flow conservation law. A laminar-turbulent pattern with/without an oblique interface is organized by the mass balance of streamwise and spanwise components. The shape of the large-scale flow is changed by the non-negligible wall-normal velocity component caused by the insufficient spanwise length or other large-scale motion by roll cells/one-wall roughness.

These mechanisms prove that the laminar-turbulent pattern is a universal phenomenon changing the form of patterning with/without obliqueness depending on the wall-normal and spanwise large-scale flow caused by the flow geometry. The pattern is not robust when intensive wall-normal velocity exists and the SSP is promoted by additional effects, such as rotation and wall roughness. The pattern would be obtained in several situations by varying the shape of the pattern when the large-scale flow can be sustained.

Our study, with considering all the various factors, focusing on laminar-turbulent pattern

in wall-bounded shear flows categorized by subcritical transition find the large- and small-scale flow is important to sustain the pattern. In addition, the property of the pattern is determined by the pattern shape and the patterning is characterized by the interaction of large- and small-scale flow. When large-scale flow is sufficiently enough, the pattern is infinite oblique pattern, whereas the angle of obliqueness decreases and streamwise localization emerges when large-scale flow cannot maintain. The infinite oblique pattern is equilibrium state and maintain the same regime. However, there is not equilibrium state in the case of streamwise localized structure with weak obliqueness or without obliqueness, and splitting/merging event of the pattern appear. Although the pattern property is determined by the large-scale flow, the large-scale flow cannot maintain when small-scale flow does not exist. Therefore, small-scale flow effects the patterning in an indirect manner. In addition small-scale flow directly effects the amount of turbulence or laminar regime in the flow. Attenuating small-scale flow as self-sustaining process of turbulent coherent structures induces decaying large-scale flow and finally the pattern is collapsed. In contrast, small-scale flow is enhanced, the pattern expands spatially and finally transition to fully-developed turbulence.

Appendix A

This thesis is constructed by the following articles.

1. Ishida, T., Tsukahara, T., and Kawaguchi Y., 2014, “Large-scale structure alternation in rotating plane Poiseuille flow at transitional Reynolds number”, *Applied Thermal Engineering*, **72**, 70–81.
2. Ishida, T., Tsukahara, T., and Kawaguchi Y., 2015, “Effects of spanwise system rotation on turbulent stripe in plane Poiseuille flow”, *Journal of Turbulence*, **16**, 273–289.
3. Ishida, T., Duguet, Y., and Tsukahara T., 2016, “Transitional structures in annular Poiseuille flow depending on radius ratio”, *Journal of Fluid Mechanics*, **794**, R2 (11 pages).
4. Ishida, T., and Tsukahara T., 2016, “Friction factor of annular Poiseuille flow in a transitional regime”, *Advances in Mechanical Engineering*, **9**, 1 (10 pages).
5. Ishida, T., Brethouwer, G., Duguet, Y., and Tsukahara T., “Laminar-turbulent patterns with rough walls”, *under review*.

Acknowledgements

This dissertation was achieved during my study for my doctoral course at Tokyo University of Science.

My first acknowledgement is directed to my supervisor Professor Yasuo Kawaguchi and advisor Junior Associate Professor Takahiro Tsukahara, Department of Mechanical Engineering, Tokyo University of Science. They made enormous contributions and gave great support.

I would like to thank Doctor Yohann Duguet, LIMSI-CNRS, and Doctor Geert Brethouwer, KTH, for their invaluable advice and hosting in France and Sweden, respectively, during my research visits. Advice and comments given by the France-Japan workshop with Professor Genta Kawahara, Professor Susumu Goto, Assistant Professor Masaki Shimizu, School of Engineering and Science, Osaka University, and Professor Paul Manneville, Hydrodynamics Laboratory, École Polytechnique have been of great help in the study.

I also thank the members of four universities' joint workshop for their insightful advices, namely Professor Koji Fukagata, Department of Mechanical Engineering, Keio University, Associate Professor Kaoru Iwamoto, Department of Mechanical Systems Engineering, Tokyo University of Agriculture and Technology, Associate Professor Yosuke Hasegawa, Institute of Industrial Science, The University of Tokyo, and Assistant Professor Mamori Hiroya, Department of Mechanical Engineering, Tokyo University of Science. I am particularly grateful for the assistance given by colleagues in the group of Professor Yasuo Kawaguchi and Junior Associate Professor Takahiro Tsukahara at the Tokyo University of Science.

This thesis has been reviewed by the committee in Tokyo University of Science with Professor Yasuo Kawaguchi, Department of Mechanical Engineering, Professor Makoto Yamamoto, Department of Mechanical Engineering, Professor Hiroshi Okada, Department of Mechanical Engineering, Professor Yasuo Nihei, Department of Civil Engineering, Associate Professor Akiyuki Takahashi, Department of Mechanical Engineering. I greatly thank them valuable comments.

I have greatly benefited from a Grant-in-Aid from JSPS (Japan Society for the Promotion of Science) Fellowship #26-7477 . I also thank SX-9 at the Cyberscience Center of Tohoku University and on SX-ACE at the Cybermedia Center of Osaka University for obtaining simulation results.

Last but not least, I owe my deepest gratitude to my family, Shinichi Ishida, Etsuko Ishida, and Kanako Ishida for their continuous encouragement and support.

Bibliography

- Abe, H., Kawamura, H., and Matsuo, Y., 2001, “Direct numerical simulation of a fully developed turbulent channel flow with respect to the Reynolds number dependence”, *J. Fluids Eng.*, **123**, 382–393.
- Ashrafian, A., Andersson, H. I., and Manhart, M., 2004, “DNS of turbulent flow in a rod-roughened channel”, *Int. J. Heat Fluid Flow*, **25**, 373–383.
- Avila, K., Moxey, D., de Lozar, A., Avila, M., Barkley, D., and Hof, B., 2011, “The onset of turbulence in pipe flow”, *Science*, **333**, 192–196.
- Aydin, E. M., and Leutheusser, H. J., 1991, “Plane Couette flow between smooth and rough wall”, *Exp. Fluids*, **11**, 302.
- Barkley, D., 2011, “Computational study of turbulent laminar patterns in Couette flow”, *Phys. Rev. E*, **84**, 016309.
- Barkley, D., 2016, “A theoretical perspective on the route to turbulence in a pipe”, *J. Fluid Mech.*, **803**, 192–196.
- Borrero-Echeverry, D., Schatz, M. F., and Tagg, R., 2010, “Transient turbulence in Taylor-Couette flow”, *Phys. Rev. E*, **81**, 025301.
- Bottin, S., Dauchot, O., Daviaud, F., and Manneville, P., 1998, “Experimental evidence of streamwise vortices as finite amplitude solutions in transitional plane Couette flow”, *Phys. Fluids*, **10**, 2597–2607.
- Bradshaw, P., 1969, “The analogy between streamline curvature and buoyancy in turbulent shear flow”, *J. Fluid Mech.*, **36**, 177–191.
- Brethouwer, G., Duguet, Y., and Schlatter, P., 2012, “Turbulent-laminar coexistence in wall flows with Coriolis, buoyancy or Lorentz forces”, *J. Fluid Mech.*, **704**, 137–172.
- Busse, A. and Sandham, N. D., 2012, “Parametric forcing approach to rough-wall turbulent channel flow”, *J. Fluid Mech.*, **712**, 169–202.
- Cambon, C., Mansour, N. N., and Godeferd, S. F., 1997, “Energy transfer in rotating turbulence”, *J. Fluid Mech.*, **337**, 303–337.
- Chung, S. Y., Rhee, G. H., and Sung, H. J., 2002 “Direct numerical simulation of turbulent concentric annular pipe flow: Part 1: Flow field”, *Int. J. Heat Fluid Flow*, **23**, 426–440.

- Chung, S. Y. and Sung, H. J., 2003, “Direct numerical simulation of turbulent concentric annular pipe flow: Part 2: Heat transfer”, *Int. J. Heat Fluid Flow*, **24**, 399–411.
- Coles, D., 1965 “Transition in circular Couette flow”, *J. Fluid Mech.*, **21**, 385–425.
- Cortet, P. P., Chiffaudel, A., Daviaud, F., and Dubrulle, B. 2010, “Experimental evidence of a phase transition in a closed turbulent flow”, *Phys. Rev. Lett.*, **105**, 2145101.
- Cotrell, D. L. and Pearlstein, A. J., 2006, “Linear stability of spiral and annular Poiseuille flow for small radius ratio”, *J. Fluid Mech.*, **547**, 1–20.
- Couliou, M. and Monchaux, R., 2015, “Large-scale flows in transitional plane Couette flow: A key ingredient of the spot growth mechanism”, *Phys. Fluids*, **27**, 3, 034101.
- Croop E. J. and Rothfus R. R., 1962, “Skin friction patterns for transitional flow in annuli”, *AIChE Journal*, **8**, 26–30.
- Deguchi, K. and Nagata, M., 2011, “A numerical study of the stratified and unstratified Ekman layer”, *J. Fluid Mech.*, **678**, 156–178.
- Deusebio, E., Brethouwer, G., Schlatter, P., and Lindborg, E., 2014, “A numerical study of the stratified and unstratified Ekman layer.”, *J. Fluid Mech.*, **755**, 672–704.
- Deusebio, E., Caulfield, C. P., and Taylor, J. R., 2015, “The intermittency boundary in stratified plane Couette flow.”, *J. Fluid Mech.*, **781**, 298–329.
- Duguet, Y., Schlatter, P., and Henningson, D. S., 2009, “Localized edge states in plane Couette flow”, *Phys. Fluids*, **21**, 111701.
- Duguet, Y., Schlatter, P., and Henningson, D. S., 2010, “Formation of turbulent patterns near the onset of transition in plane Couette flow”, *J. Fluid Mech.*, **650**, 119–129.
- Duguet, Y. and Schlatter, P., 2013, “Oblique laminar-turbulent interfaces in plane shear flows”, *Phys. Rev. Lett.*, **110**, 034502.
- Eckhardt, B., Schneider, T. M., Hof, B. and Westerweel, J., 2007, “Turbulent transition in pipe flow”, *Ann. Rev. Fluid Mech.*, **39**, 447–468.
- Finnigan, J. J., Shaw, R. H., and Patton, E. G., 2009, “Turbulence structure above a vegetation canopy”, *J. Fluid Mech.*, **637**, 387–424.
- Floryan, J. M., 2007, “Three-dimensional instabilities of laminar flow in a rough channel and the concept of hydraulically smooth wall”, *Eur. J. Phys. B*, **26**, 3, 305–329.
- Fukudome, K. and Iida, O., 2012, “Large-scale flow structure in turbulent Poiseuille flows at low-Reynolds numbers”, *J. Fluid Sci. and Tech*, **7**, 181–195.
- Hanks, R. W. and Bonner, W. F., 1971, “Transitional flow phenomena in concentric annuli”, *Ind. Eng. Chem. Fundamen.*, **10**, 105–113.
- Hanks, R. W. and Peterson, J. M., 1982, “Complex transitional flows in concentric annuli”, *AIChE Journal*, **28**, 800–806.

- Hashimoto, S., Hasobe, A., Tsukahara, T., Kawaguchi, Y., and Kawamura, H., 2009, “Experimental study on turbulent stripe structure in transitional channel flow”, *Proc. the 6th Int. Symp. Turbulence, Heat and Mass Transfer*, pp. 193-196.
- Heaton, C. J., 2008, “Linear instability of annular Poiseuille flow”, *J. Fluid Mech.*, **610**, 391–406.
- Iida, O., Fukudome, K., Iwata, T., and Nagano, Y., 2010, “Low Reynolds number effects on rotating turbulent poiseuille flow”, *Phys. Fluids*, **22**, 085106.
- Jimenez, J. and Moin, P., 1991, “The minimal flow unit in near-wall turbulence”, *J. Fluid Mech.*, **225**, 213–240.
- Jimenez, J., 2004, “Turbulent flows over rough walls”, *Ann. Rev. Fluid Mech.*, **36**, 173–196.
- Johnston, J. P., Halleen, R. M., and Lezius, D. K., 1972, “Effects of spanwise rotation on the structure of two-dimensional fully developed turbulent channel flow”, *J. Fluid Mech.*, **438**, 533–557.
- Kerswell, R., 2011, “Transition Scenarios: Normality vs Non-Normality”, *Lecture note.*, Lecture 7.
- Khapko, T., Schlatter, P., Duguet, Y. and Henningson, D. S., 2016, “Turbulence collapse in a suction boundary layer flow”, *J. Fluid Mech.*, **795**, 356–379.
- Kristoffersen, R. and Andersson, H. I., 1993, “Direct simulations of low-Reynolds-number turbulent flow in a rotating channel”, *J. Fluid Mech.*, **256**, 163–197.
- Kunii, K., Ishida, T., and Tsukahara, T., 2016, “Helical turbulence and puff in transitional sliding Couette flow”, *Proc. ICTAM, Montréal, Canada*.
- Lamballais, E., Lesieur, M., and Métais, O., 1996, “Effects of spanwise rotation on the vorticity stretching in transitional and turbulent channel flow”, *Int. J. Heat and Fluid Flow*, **17**, 324–332.
- Lemoult, G., Gumowski, K., Aider, J. L., and Wesfreid, J. E. 2014, “Turbulent spots in channel flow: An experimental study”, *Eur. Phys. J. E*, **37**, 1–11.
- Lemout, G., Shi, L., Avila, K., Jalikop, S., Avila, M., and Hof, B., 2016, “Directed percolation phase transition to sustained turbulence in Couette flow”, *Nature Physics*, **12**, 254–258.
- Lezius, D. K. and Johnston, J. P., 1976, “Roll-cell instabilities in rotating laminar and turbulent channel flows”, *J. Fluid Mech.*, **77**, 153–175.
- Liu, N. S. and Lu, X. Y., 2004, “Large eddy simulation of turbulent concentric annular channel flows”, *Int. J. Numer. Methods Fluids*, **45**, 1317-1338.

- Lundbladh, A. and Johansson, A.V., 1991, “Direct simulation of turbulent spots in plane Couette flow”, *J. Fluid Mech.*, **229**, 499-516.
- Mahrt, L., 2014, “Stably stratified atmospheric boundary layer flows”, *Annu. Rev. Fluid Mech.*, **46**, 23-25.
- Manneville, P., 2011, “On the decay of turbulence in plane Couette flow”, *Fluid Dyn. Res.*, **43**, 065501.
- Manneville, P., 2015, “On the transition to turbulence of wall-bounded flows in general, and plane Couette flow in particular”, *Eur. J. Phys. B*, **49**, 345–362.
- Manneville, P., 2016, “Transition to turbulence in wall-bounded flows: Where do we stand?”, *Mech. Eng. Rev.*, **3**, 15-00684.
- Matsson, O. J. E., and Alfredsson, P. H., 1994, “The effect of spanwise system rotation on Dean vortices”, *J. Fluid Mech.*, **274**, 243–265.
- Matsubara, M., Alfredsson, P. H., 1996, “Experimental study of heat and momentum transfer in rotating channel flow”, *Phys. Fluids*, **8**, 2964.
- Moin, P. and Kim, J., 1982, “Numerical investigation of turbulent channel flow”, *Phys. Fluids*, **11**, 2065–2073.
- Morinishi, Y., Nakabayashi, K. and Ren, S. Q., 2001, “Dynamics of anisotropy on decaying homogeneous turbulence subjected to system rotation”, *Phys. Fluids*, **1**, 2912–2922.
- Mott, J. E. and Joseph, D. D., 1968, “Stability of Parallel Flow between Concentric Cylinders”, *J. Fluid Mech.*, **118**, 341–377.
- Moxey, D. and Barkley, D., 2010, “Distinct large-scale turbulent-laminar states in transitional pipe flow”, *PNAS*, **107**, 8091–8096.
- Nakabayashi, K. and Kitoh, O., 1996, “Low Reynolds number fully developed two-dimensional turbulent channel flow with system rotation”, *J. Fluid Mech.*, **315**, 1–29.
- Nikuradse, J., 1993, “Laws of flows in rough pipes”, *VDI Forschungsheft*.
- Patel, V. C., and Head, M. R., 1969, “Some observations on skin friction and velocity profiles in fully developed pipe and channel flows”, *J. Fluid Mech.*, **38**, 181–201.
- Pfenniger, W., 1961, “Transition in the inlet length of tubes at high Reynolds numbers”, in *Boundary Layer and Flow Control* (ed. G. V. Lachman), 970–980.
- Philip, J. and Manneville, P., 2010, “From temporal to spatiotemporal dynamics in transitional plane Couette flow”, *Phys. Rev. E*, **83**, 036308.
- Pomeau, Y., 1986, “Front motion, metastability and subcritical bifurcations in hydrodynamics”, *Physica D*, **23**, 3–11.
- Pope, S., 2000, *Turbulent flows*, Cambridge Univ. Press.

Prigent, A., 2001, “La spirale turbulente: motif de grande longueur d’onde dans les écoulements cisailés turbulents”, *PhD Thesis, Université Paris XI*.

Prigent, A. and Dauchot, O., 2002, “Transition to versus from turbulence in subcritical Couette flows”, *Phys. Rev. Lett.*, **89**, 014501.

Reynolds, O., 1883, “An experimental investigation of the circumstances which determine whether the motion of water shall be direct or sinuous, and of the law of resistance in parallel channels”, *Philos. Trans. Roy. Soc. Lond.*, **174**, 935–982.

Rodriguez-Corredor, F. E., Bizhani, M., Ashrafuzzaman, M., and Kuru, E., 2014, “An experimental investigation of turbulent water flow in concentric annulus using particle image velocimetry technique”, *J. Fluids Eng.*, **136**, 051203.

Romanov, V. A., 1973, “Stability of plane-parallel Couette flow”, *Functional Anal. Appl.*, **7**, 137–146.

Rolland, J. and Manneville, P., 2011, “Pattern fluctuations in transitional plane Couette flow”, *J. Statistical Phys.*, **142**, 577–591.

Rothfus R. R., Monrad C. C., and Senecal V. E., 1950, “Velocity distribution and fluid friction in smooth concentric annuli”, *Industr. Engng. Cheml*, **42**, 2511–2520.

Samanta, D., De Lozar, A., and Hof, B., 2011, “Experimental investigation of laminar turbulent intermittency in pipe flow”, *J. Fluid Mech.*, **681**, 193–204.

Sano, M. and Tamai, K., 2015, “A universal transition to turbulence in channel flow”, *Nature Physics.*, **12**, 249–253.

Satake, S. and Kawamura, H., 1995, “Large eddy simulation of turbulent flow in concentric annuli with a thin inner rod”, *Turbulent Shear Flows 9, Springer Berlin Heidelberg*, 259-281.

Seki, D. and Matsubara, M., 2012, “A universal transition to turbulence in channel flow”, *Phys. Fluids*, **24**, 124102.

Schlichtung, H., 1968, *Boundary-layer theory*, *MC-Graw Hill New York*.

Schmid, P. J. and Henningson, D. S., 2001, “Stability and transition in shear flows”, *Springer*.

Shi, L., Avila, M., and Hof, B., 2013, “Scale invariance at the onset of turbulence in Couette flow”, *Phys. Rev. Lett.*, **110**, 204502.

Shimizu, M., Manneville, P., Duguet, Y., and Kawahara, G., 2014, “The universality class of the transition to turbulence”, *Fluid Dyn. Res.*, **46**, 061403.

Su, H. B., Shaw, R. H., Paw, K. T., Moeng, C. H., and Sullivan, P. P., 1998, “Turbulent statistics of neutrally stratified flow within and above a sparse forest from large-eddy simulation and field observations”, *Boundary Layer Meteorol.*, **88**, 363–397.

Tafti, D. K. and Vanka, S. P., 1991, “A numerical study of the effects of spanwise rotation on turbulent channel flow”, *Phys. Fluids A* **3**, 642–656.

Takeishi, K., Kawahara, G., Wakabayashi, H., Uhlmann, M., and Pinelli, A., 2015, “Localized turbulence structures in transitional rectangular-duct flow”, *J. Fluid Mech.*, **782**, 368-379.

Tsukahara, T., Seki, Y., Kawamura, H., and Tochio, D., 2005, “DNS of turbulent channel flow at very low Reynolds numbers”, *Proc. 4th Int. Symp. on Turbulence and Shear Flow Phenomena, Williamsburg, USA*, pp. 935–940.

Tsukahara, T., Iwamoto, K., Kawamura, H., and Takeda, T., 2006, “DNS of heat transfer in a transitional channel flow accompanied by a turbulent puff-like structure”, *Turbulence, Heat and Mass Transfer 5, 339 K. Hanjalić et al., eds.*, pp. 193–196

Tsukahara, T., Kawaguchi, Y., Kawamura, H., Tillmark, N., and Alfredsson, P. H., 2010a, “Turbulence, instabilities and passive scalars in rotating channel flow”, *Seventh IUTAM Symposium on Laminar-Turbulent Transition*, **18**, 421–426.

Tsukahara, T., Tillmark, N., and Alfredsson, P. H., 2010b, “Flow regimes in a plane Couette flow with system rotation”, *J. Fluid Mech.*, **648**, 5-33.

Tuckerman, L. S., Kreilos, T., Schrobsdorff, H., Schneider, T. M., and Gibson, J. F., 2014, “Turbulent-laminar patterns in plane Poiseuille flow”, *Phys. Fluids*, **26**, 114103.

Waleffe, F., 1997, “On a self-sustaining process in shear flows”, *Phys. Fluids*, **9**, 883–900.

Walker, J. E., Whan, G. A., and Rothfus, R. R., 1957, “Fluid friction in noncircular ducts”, *AIChE Journal*, **3**, 484–489.

Wynanski, I. J., and Champagne, F. H., 1973, “On transition in a pipe. Part1. The origin of puffs and slugs and the flow in a turbulent slug”, *J. Fluid Mech.*, **59**, 281–335.

Wynanski, I. J., Sokolov, M., and Freidman, D., 1975, “On transition in a pipe. Part2. The equilibrium puff”, *J. Fluid Mech.*, **69**, 283–304.

Xiong, X., Tao, J., Chen, S., and Brandt, L., 2015 “Turbulent bands in plane-Poiseuille flow at moderate Reynolds numbers”, *Phys. Fluids*, **27**, 041702.